

**A Fracture Mechanical Study of
Precipitation Hardenable
Aluminium-Based Metal Matrix Composites**

☒ This is granted
permission to
reproduce and sell,
on a not-for-profit
basis

☒ Yes only
☐ No in the
US, Canada
Mexico

Cover design: Rob Deurenberg
Microstructure of an AA6061 alloy reinforced with Al_2O_3 particles with on top the finite element mesh used for calculation of the fracture toughness.

A Fracture Mechanical Study of Precipitation Hardenable Aluminium-Based Metal Matrix Composites

Een breukmechanisch onderzoek naar op aluminium gebaseerde
precipitatie hardende metaal matrix composieten

PROEFSCHRIFT

ter verkrijging van de graad van doctor
aan de Technische Universiteit Delft,
op gezag van de Rector Magnificus Prof. ir. K.F. Wakker,
voorzitter van het College voor Promoties,
in het openbaar te verdedigen op vrijdag 22 september 2000 te 13.30 uur

door

Katinka Mariska MUSSERT

materiaalkundig ingenieur
geboren te Rotterdam

Dit proefschrift is goedgekeurd door de promotoren:

Prof.dr.ir. A. Bakker

Prof.dr.ir. S. van der Zwaag

Samenstelling promotiecommissie

Rector Magnificus,

Prof. dr. ir. A. Bakker,

Prof. dr. ir. S. van der Zwaag,

Prof. dr. ir. E. van der Giessen,

Prof. ir. L. Katgerman,

Prof. dr. H. W. Zandbergen,

Prof. dr. -ing. W. Brocks,

Prof. dr. ir. L. Froyen,

voorzitter

Technische Universiteit Delft, promotor

Technische Universiteit Delft, promotor

Technische Universiteit Delft

Technische Universiteit Delft

Technische Universiteit Delft

GKSS Research Centre Geesthacht, Duitsland

Katholieke Universiteit Leuven, België

Dr. ir. Michael Janssen heeft als begeleider in belangrijke mate aan het totstandkomen van dit proefschrift bijgedragen.

Published and distributed by:

Delft University Press

P.O. Box 98

2600 MG Delft

The Netherlands

Telephone: +31 15 2783254

Telefax: +31 15 2781661

E-mail: DUP@Library.TUDelft.NL

ISBN 90-407-2090-8

NTIS is authorized to reproduce and sell this
report. Permission for further reproduction
must be obtained from the copyright owner.

Copyright © 2000 by Ir. K.M. Mussert

All rights reserved. No part of the material protected by this copyright notice may be reproduced or utilised in any form or by any means, electronic or mechanical, including photocopying, recording or by any information storage and retrieval system, without written permission from the publisher: Delft University Press.

Printed in the Netherlands

CONTENTS

| | |
|---|-----------|
| CONTENTS | v |
| NOMENCLATURE | ix |
| 1 METAL MATRIX COMPOSITES | 1 |
| 1.1 Introduction | 1 |
| 1.2 Aluminium-Based MMCs | 2 |
| 1.3 Failure Mechanisms in Particle Reinforced MMCs | 3 |
| 1.4 Effect of Microstructural Variables on Fracture Toughness | 4 |
| 1.5 Finite Element Modelling of Fracture in MMCs | 7 |
| 1.6 Scope of this Thesis | 8 |
| PART A: INVESTIGATION OF MATERIAL BEHAVIOUR | |
| 2 PRECIPITATION KINETICS IN AA6061 AND AN AA6061 BASED MMC | 11 |
| 2.1 Introduction | 11 |
| 2.1.1 Thermal Analysis of Phase Transformations | 11 |
| 2.1.2 Kinetic Analysis of Phase Transformations | 12 |
| 2.2 Experimental Procedure | 14 |
| 2.3 Results and Discussion | 15 |
| 2.3.1 Differential Scanning Calorimetry | 15 |
| 2.3.2 Kinetic Parameters | 19 |
| 2.4 Conclusions | 23 |
| 3 NANOINDENTATION STUDY INTO THE MECHANICAL BEHAVIOUR OF MMC MATRIX MATERIAL | 25 |
| 3.1 Introduction | 25 |
| 3.2 Materials Used | 26 |
| 3.3 Nanoindentation Procedure | 27 |
| 3.4 Results and Discussion | 29 |
| 3.5 Conclusions | 34 |

| | | |
|---|---|-----------|
| 4 | FRACTURE MECHANICAL EXPERIMENTS | 35 |
| 4.1 | Introduction | 35 |
| 4.2 | Materials | 35 |
| | 4.2.1 Commercial Materials | 35 |
| | 4.2.2 Experimental Material | 37 |
| 4.3 | Tensile Experiments | 39 |
| 4.4 | Fracture Mechanical Parameters | 40 |
| | 4.4.1 Stress Intensity Factor K | 40 |
| | 4.4.2 J-Integral Concept | 41 |
| 4.5 | Fracture Toughness Experiments | 42 |
| | 4.5.1 Fatigue Precracking | 43 |
| | 4.5.2 Fracture Toughness Test Methods Used | 44 |
| 4.6 | Tensile Test Results | 49 |
| 4.7 | Fracture Toughness Test Results and Discussion | 50 |
| | 4.7.1 AA6061 Aluminium Alloy | 50 |
| | 4.7.2 Commercial MMC | 54 |
| | 4.7.3 Experimental MMC | 57 |
| 4.8 | Conclusions | 63 |
| PART B: MODELLING MECHANICAL BEHAVIOUR | | |
| 5 | MODELLING PARTICLE FRACTURE USING WEIBULL STATISTICS | 67 |
| 5.1 | Introduction | 67 |
| 5.2 | Cell Model | 67 |
| 5.3 | Weibull Model | 68 |
| 5.4 | Finite Element Calculations | 69 |
| 5.5 | Parameter Dependence | 70 |
| | 5.5.1 Reference Configuration | 71 |
| | 5.5.2 Loading History | 71 |
| | 5.5.3 Weibull Modulus | 72 |
| | 5.5.4 Stresses in the Particle | 72 |
| | 5.5.5 Matrix Hardening | 75 |
| | 5.5.6 Characteristic Stress and Yield Stress | 75 |
| | 5.5.7 Particle Size | 78 |
| 5.6 | Conclusions | 78 |
| 6 | MODELLING DAMAGE IN MMCS USING GURSON'S MODEL | 81 |
| 6.1 | Introduction | 81 |
| 6.2 | Continuum Model for Voided Material | 82 |
| 6.3 | Void Growth and Coalescence in MMCs | 83 |
| 6.4 | Calculation of Fracture Toughness on DSCT-Specimens | 87 |
| 6.5 | Effect of Heat Treatment on Fracture Toughness | 89 |
| 6.6 | Extrapolation of Concept | 92 |
| 6.7 | Conclusions | 93 |
| 6.8 | Concluding Remarks | 94 |

Contents

| | |
|-------------------------|------------|
| REFERENCES | 95 |
| SUMMARY | 105 |
| SAMENVATTING | 111 |
| ACKNOWLEDGEMENTS | 117 |
| THE AUTHOR | 119 |

NOMENCLATURE

Greek Symbols

| | |
|--------------------------------|--|
| α | function of ratio of compression strength and tensile strength |
| β | state variable fully determining the state of transformation |
| δ | crack opening displacement |
| ε | elongation |
| ε_e | effective strain |
| ε_{eq} | equivalent strain |
| ϕ | heating rate |
| Φ | flow potential |
| Γ | integration path |
| η | (plastic) work factor |
| λ_v | distance between microcracks in front of the crack tip |
| ν | Poisson's ratio |
| ρ | stress proportionality factor |
| σ | applied stress, stress in ceramic particle |
| σ_0 | constant with dimensions of stress ('characteristic stress') |
| $\sigma_1, \sigma_2, \sigma_3$ | principal stress in x-, y-, z-direction |
| σ_c | compression strength |
| σ_{DP} | Drucker-Prager stress |
| σ_{kk} | hydrostatic stress |
| σ_M | average Von Mises stress in the matrix |
| σ_r | stress in radial direction |
| σ_t | tensile strength |
| $\sigma_{u.s}$ | ultimate tensile strength |
| σ_{VM} | macroscopic Von Mises stress |
| σ_{yi} | yield strength |
| σ_{zz} | stress in axial direction |

Roman Symbols

| | |
|--------------------|--|
| a | crack length |
| a_i | current crack length |
| A | length of reduced section for tensile specimen |
| $A_{pl(i)}$ | increment of plastic area under a load versus load-line displacement record |
| A | total area under a DSC peak or projected area of elastic contact |
| b | size of the uncracked ligament ahead of the crack |
| B | thickness of disk-shaped compact tension specimen |
| B_N | net thickness |
| C | compliance |
| C_1, C_2 | fit coefficients |
| C_{ll} | compliance calculated at load-line displacement |
| d | particle diameter |
| ds | increment of contour path |
| D | diameter of tensile specimen |
| E | elastic modulus |
| E' | plane strain elastic modulus |
| E_r | reduced elastic modulus |
| E | activation energy |
| f | particle volume fraction |
| $f(a/W)$ | stress intensity geometry factor for crack length a and specimen width W |
| $f(\underline{x})$ | some function of the position \underline{x} in a particle |
| $f(y)$ | function depending on the reaction mechanism of the phase transformation |
| f | void volume fraction |
| f^* | function of the void volume fraction f |
| f_0 | initial void volume fraction |
| f_c | critical void volume fraction at void coalescence |
| f_f | void volume fraction at failure |
| f_N | volume fraction of void forming particles |
| f_u^* | ultimate void volume fraction ($=1/q_1$) |
| G | elastic energy per unit crack surface area |
| GL | gauge length of tensile specimen |
| h_c | depth of contact |
| h_f | final depth of contact impression after unloading |
| h_{max} | indenter displacement at peak load |
| H | hardness |
| H | enthalpy |
| J | J-integral |
| J_c | critical J-value at the onset of crack extension |
| J_{el} | elastic component of J |
| J_{Ic} | mode I critical J-value at the onset of crack extension |
| J_{pl} | plastic component of J |
| J_Q | conditional calculated critical J-integral |
| k_0 | pre-exponential factor |
| $k(T)$ | rate constant |
| K | stress intensity factor |
| K_I | mode I stress intensity factor |

| | |
|-----------------|--|
| K_{Ic} | mode I critical stress intensity factor |
| K_J | stress intensity factor calculated using J-integral |
| K_{IcQ} | conditional calculated critical stress intensity factor |
| L_c | initial unit cell length |
| m | Weibull modulus |
| n | hardening exponent |
| n | numerical exponent |
| P | applied load |
| P_{max} | maximum load during a fatigue cycle or an indentation |
| P_{C_i} | load to calculate conditional critical stress intensity factor |
| q_1, q_2 | empirical fitting parameters in modified Gurson model |
| r | radius of fillet of tensile specimen |
| r_0 | radius of spherical particle |
| r_p | plastic rotation factor |
| r_p | plastic zone size |
| R | ratio of minimum to maximum stress |
| R_c | initial unit cell radius |
| R | gas constant |
| S | survival probability |
| S | initial unloading stiffness |
| T | absolute temperature |
| T_i | temperature corresponding to the point of inflection on a y-T curve |
| T_{yf} | temperature for a fixed stage of transformation |
| \underline{T} | outward traction vector on the contour around a crack |
| \underline{u} | displacement vector |
| U_f | potential energy |
| V | ceramic particle volume, volume of a deformed cell |
| V_c | constant with dimensions of volume or volume of undeformed cell |
| V_e | volume due to elastic dilatation |
| V_l | load-line displacement |
| $V_{l,el}$ | elastic part of clip gauge displacement at load-line |
| $V_{l,pl}$ | plastic part of clip gauge displacement at load-line |
| V_x | crack mouth opening displacement |
| $V_{x,pl}$ | plastic component of the crack mouth opening displacement |
| W | width of disk-shaped compact tension specimen |
| W_{strain} | strain energy per unit volume due to loading |
| x | rectangular co-ordinate in the crack direction |
| y | fraction of a phase transformation completed at a given time |
| y_i | fraction transformed |
| y_f | fixed stage of transformation |
| y | rectangular co-ordinate normal to the crack direction |
| z | distance between clip gauge knife edge measuring point and the load-line in the specimen |

Abbreviations

| | |
|------|--|
| ASTM | American Society for Testing and Materials |
| CGR | crack growth region |
| CMOD | crack mouth opening displacement |
| CTE | coefficient of thermal expansion |
| DSC | differential scanning calorimetry |
| DSCT | disk-shaped compact tension |
| EDS | energy dispersive spectrum |
| EPFM | elastic-plastic fracture mechanics |
| EPMA | electron probe microanalysis |
| FEM | finite element method |
| LEFM | linear elastic fracture mechanics |
| MMC | metal matrix composite |
| RTD | resistance temperature detector |
| SEM | scanning electron microscope |
| SiC | silicon carbide |
| TEM | transmission electron microscope |
| WQ | water quench |
| XRF | X-ray fluorescence |

1

METAL MATRIX COMPOSITES

1.1 Introduction

Aluminium alloys are widely used in transportation and aerospace applications, due to their low density in combination with an adequate stiffness, strength and ductility. Aluminium also possesses other properties of considerable technological importance, *e.g.* a high corrosion resistance and high electrical and thermal conductivity. A major additional advantage of aluminium alloys is the fact that their properties can be adjusted through thermomechanical treatments. Although most metallic elements will alloy with aluminium, comparatively few have sufficient solid solubility to serve as major alloying additions. Of the commonly used elements, only zinc, magnesium, copper and silicon have significant solubilities. However, several other elements with solubilities below 1 at.% confer important improvements to alloy properties. By suitable alloying and heat treatment, it is possible to increase the yield strength of high-purity aluminium by as much as 40 times [1]. The microstructure of an aluminium alloy consists of either precipitate structures or dispersoid structures. Precipitates are fine particles of phases that were in solution in aluminium at an elevated temperature and precipitated from solid solution at a lower temperature, whereas dispersoids are fine particles, in general larger than precipitates, that precipitate from solid solution, either during cooling after casting or during preheating [2].

Besides the advantages, aluminium alloys have some intrinsic disadvantages like a rather low stiffness of 69 GPa, a moderate wear resistance and a poor high temperature performance. Aiming at even better materials, it is desirable to improve the properties of current aluminium alloys. An important development of the last few decades in this direction is the development of aluminium-based metal matrix composites (MMCs) which consist of ceramic particles embedded in an aluminium matrix, see figure 1.1. With these composites, it is possible to achieve a higher elastic modulus, a high wear resistance and a high strength at elevated temperatures. Such composites cause a number of problems in machining, joining and recycling. However, their major drawback is the low ductility and low fracture toughness. It is the aim of the research described in this thesis, to understand the factors responsible for this low toughness and based on this knowledge to design routes for less brittle MMCs.

1.2 Aluminium-Based MMCs

A composite material can be described as a mixture of component materials designed to meet a specific engineering role by exploiting the desirable properties of the components and minimising their less desirable properties [3]. This concept results in the production of stiffer and stronger materials like MMCs which consist of particles or fibres embedded in a metallic matrix [4]. A composite then is designed to display a combination of the best characteristics of each of the component materials.

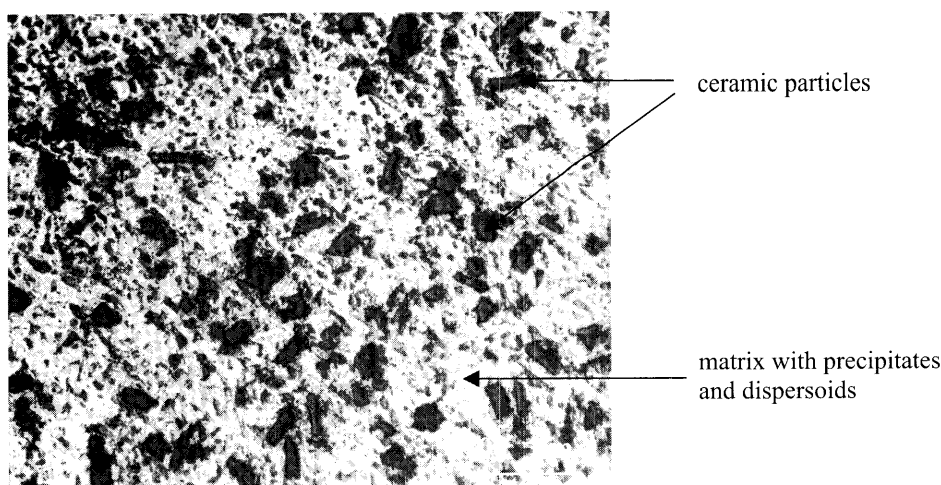


Figure 1.1
Microstructure of an AA6061 alloy reinforced with 20 vol.% Al_2O_3 particles

The most widely applied metals as matrix material for MMCs are aluminium and its alloys, since their ductility, formability and low density can be combined with the stiffness and load-bearing capacity of the reinforcement used. Mostly, the reinforcement is a ceramic which can be continuous in the form of fibres, or discontinuous in the form of whiskers (short fibres) or particles, see figure 1.2.

Depending on whether the reinforcement is continuous or discontinuous, the metallic matrix serves quite different roles.

In case of continuous fibres, the matrix serves to hold the fibres together, to fixate them in the desired stress direction and to transfer the applied load to the fibres. The mechanical properties of the MMC are dependent upon the efficiency of the matrix in transferring the load to the reinforcing fibres and are therefore related to the bonding between the fibres and the matrix. Providing the fibre/matrix bond is good, many of the MMC properties are related to those of the reinforcement whilst the matrix properties are of secondary importance. In addition, the matrix serves to protect the fibres from mechanical damage and the matrix provides environmental protection against oxidation for example. When these requirements are met, reinforcing metals with continuous fibres can result in a substantial increase in stiffness and strength.

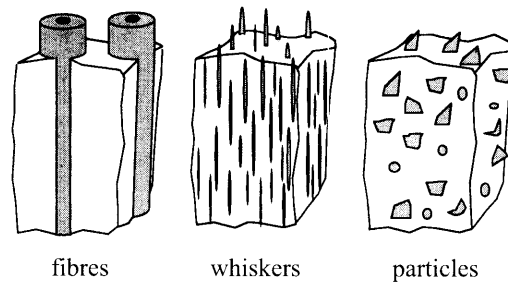


Figure 1.2

Schematic picture of three types of MMCs, classified according to the type of reinforcement [5]

For discontinuous reinforcements (whiskers or particles), both matrix and reinforcement bear substantial proportions of the load. Unlike continuously reinforced systems, the matrix strength, which is affected by precipitation and dislocation strengthening, plays an important role. Plastic deformation in the matrix of an MMC is never completely homogeneous, since reinforcements interrupt flow which gives rise to higher dislocation densities as compared to unreinforced alloys. While dislocation strengthening by the reinforcing particles is small [5], it is important for precipitation hardened matrices to consider the effect reinforcements may have upon the site and size distribution of the fine precipitates. For example, an increased dislocation density, caused by a thermal misfit strain around the reinforcement, may accelerate the nucleation of precipitates [4].

1.3 Failure Mechanisms in Particle Reinforced MMCs

Although the failure mechanisms in both an MMC and a monolithic matrix alloy are microscopically the same, the presence of brittle ceramic particles in a ductile aluminium matrix has effects on the actual failure mechanism. Consider an AA6061 particle reinforced composite containing 20 vol.% Al_2O_3 particles. It can show brittle fracture at a macroscopic scale, but microscopically seen, the MMC fails by void nucleation followed by void growth and coalescence, as does an AA6061 alloy without reinforcing particles.

So, when investigating failure in MMCs, it is useful to separate the total event of fracture in several steps, being void initiation, growth and coalescence. Definition of these steps is possible, because fracture surfaces of MMCs show characteristic features for a matrix ductile rupture mechanism [6].

Since the onset of void nucleation is the parameter controlling ductility in MMCs, this subject has been extensively researched. Mostly [7], it is assumed that fracture in discontinuously reinforced MMCs follows the same sequence as in structural alloys, namely nucleation at second phase particles followed by failure in the matrix by void coalescence. You *et al.* [8], stated that the initial step of void nucleation also occurs in the matrix, but as a consequence of the increased levels of stress and plastic constraint, caused by the addition of the reinforcing particles. These assumptions are experimentally validated by Roebuck [9]. Another possible

mechanism for void initiation is, that voids initiate near the reinforcing particle as a result of fracture of the reinforcing particle itself or debonding of the particle/matrix interface. When cracked particles act as void nucleation sites and initiate microcracks, these microcracks can be linked to each other which causes macroscopic fracture. If this mechanism is responsible for failure, the crack path followed, is the one that contains the highest area density of broken particles, whereby a relatively large percentage of broken particles should be seen at the fracture surfaces. If particle/matrix debonding precedes matrix failure, few or no broken particles should be seen at the fracture surfaces. Independent of void nucleation, a third failure mechanism [10] can be found when microcracks (in particles as well as in the matrix) in front of the main crack, are linked to this crack by void growth. These microcracks can arise as a result of high local stresses caused by inhomogeneous deformation. This inhomogeneity is due to the fact that hard and brittle ceramic particles within the plastic zone of a growing crack reduce the amount of plastic deformation of the material.

1.4 Effect of Microstructural Variables on Fracture Toughness

In the case of discontinuously reinforced MMCs, fracture toughness and fatigue behaviour can be quite sensitive to microstructural details. This sensitivity covers the reinforcement size, shape and distribution, the volume fraction of reinforcing particles, the interfacial bond strength and the matrix ageing condition in case of heat treatable alloys.

Reinforcement Size, Shape and Distribution

The primary concern regarding the dependence of fracture on the size of the reinforcement is that the failure stress of a ceramic is reduced with its size. A larger ceramic reinforcement fails sooner, thereby transferring the void nucleation mode from interfacial debonding to particle fracture. In populations with a large scatter in particle sizes, it is the largest particles which tend to fracture [11]. Consequently, in MMCs containing large particles, particle fracture is commonplace, whereas for small particles, cracking is rare.

Considering the fracture toughness of MMCs, there is no consensus whether this property increases or decreases with particle size. On the one hand, Mortensen [12] states that the total fracture energy increases with increasing particle diameter, resulting in an increased fracture toughness, on the other, Doel *et al.* [13] and Marchal *et al.* [14] conclude that the fracture toughness decreases and the portion of cracked particles increases above a certain particle diameter.

The geometry of the reinforcement has been shown to have a marked influence on the deformation behaviour of MMCs [15-17]. Song *et al.* [17] investigated particle shape effects on fracture and ductility of an AA6061 alloy reinforced with 20 vol.% Al₂O₃ particles which were either spherical or angular. The composite reinforced with spherical particles exhibited a slightly lower yield strength and work hardening rate, but a considerably higher ductility than the composite with angular particles. Examination with the scanning electron microscope (SEM) showed that during tensile deformation, the spherical composite failed through void nucleation and linking in the matrix near the particle/matrix interface, whereas the angular composite failed through particle fracture and matrix ligament rupture. Finite element calculations indicated that the distinction between the failure modes for these two composites

could be attributed to the differences in the development of internal stresses and strains within the composites due to the shape of the particles.

The formation of particle clusters during processing, *i.e.* regions with a small local interparticle distance, has deteriorating effects on the failure behaviour of MMCs. Experimental results [18-21] confirm the early occurrence of reinforcement fracture. Srivatsan [19] also concluded from a fracture surface examination that fracture occurred in the particle-rich regions and proceeded quickly. However, besides particle-rich regions there were also particle-lean regions, which aided in the retardation and were used to link a growing crack. Because of the observation of unique features in clustered areas, which were not present in structural alloys, Lloyd [18] concluded that the fracture process was controlled by large triaxial stress intensification occurring in a cluster.

Reinforcement Volume Fraction

With an increasing volume fraction of reinforcing particles, the local strain in the matrix between the particles becomes higher, resulting in premature fracture of the matrix. This is caused by the fact that, when strain is the dominating factor for failure, the distance over which this strain should be accomplished, *i.e.* the interparticle spacing, becomes shorter with increasing particle volume fraction.

Fractographic investigation into the effect of reinforcement volume fractions on fracture mechanisms by Kim *et al.* [22] showed that in a composite reinforced with 10 vol.% ceramic particles, fracture occurred by the nucleation of voids at large particles, followed by growth until coalescence. On the other hand, fracture in a composite with 30 vol.% ceramic particles was rapid and unstable. The crack propagation resistance turned out to become very small for composites reinforced with more than 20 vol.% particles. Since the constraint imposed on the matrix material determines the plastic zone size, which in its turn influences the overall fracture behaviour, it is assumed that an increase in reinforcement volume fraction leads to a decrease in plastic zone size and thus in fracture toughness.

Interfacial Bond Strength

Interfaces in conventional alloys exert an important influence on the fracture behaviour. In MMCs, this influence is expected to be even greater, because of the larger total interface surface, the chemical instabilities of most interfaces and their incoherence. Stiffening and strengthening rely on load transfer across the interface and ductility is affected by relaxation of peak stresses near the interface. For MMCs, a strong bond is usually desirable, but there may be instances where inelastic processes at the interface can be beneficial. Furthermore, there is the need for control over chemical reactions between the constituents themselves, occurring during fabrication or under service conditions at high temperatures. However, a great deal of confusion surrounds the question of how best to characterise, and then optimise, the mechanical response of the interface to stresses arising from an applied load [5].

The effect of interfacial bond strength of a powder-processed MMC was investigated by King *et al.* [23] by deliberately oxidising reinforcing particles before incorporating them into an aluminium alloy matrix. It was observed that the composite with heavily oxidised particles quickly accelerated towards final fracture at high crack growth rates when compared to a composite with naturally oxidised particles with a relatively clean surface. In contrast with King *et al.*, Ribes *et al.* [24] found higher ductilities for composites with oxidised particles. The oxidised particles were found to debond at the interface whereas the clean particles

fractured. This research appears to provide evidence for an increase in mechanical properties by a degradation of the interface. This improvement is attributed to the occurrence of stress relaxation associated with debonding at the particle/matrix interface.

Since particle fracture and interfacial debonding may occur in the same MMC depending on subtle changes in microstructure, it might be concluded that the difference in strength between the interface and the particle is small. Estimates of interfacial strengths by Flom *et al.* [25] and Davidson [26] show that the strength of an interface lies in the range 1650 - 3000 MPa, whereas SiC fracture stresses are a function of particle size and are likely to fall around 3000 MPa. This confirms the coexistence of, and the alternation between, two void nucleation modes.

Matrix Ageing Condition

When failure by void nucleation is considered, both the magnitude of the stress that can be supported within the matrix and the ability of the matrix to flow under constrained conditions is of great importance. Both can be influenced by the matrix microstructure and since precipitation changes this microstructure, it can change the fracture mechanism.

It has been reported [27] that changes in the ageing condition of the matrix material can bring about transitions in the dominant void nucleation mode. For example, in the overaged condition voids nucleated preliminary by interfacial debonding, whereas in the underaged condition particle fracture was the most important void nucleation mode in case of AA7xxx alloys reinforced with SiC particles.

Furthermore, through ageing and various process routes one or more interfacial layers adjacent to the reinforcing particle can be formed. These layers either consist of a high concentration of precipitates or are depleted of precipitating elements. Liu *et al.* [28] developed a model with which they linked the effect of a heat treatment to the void nucleation mechanism. For the peak-aged condition void nucleation occurred in a ductile interface layer at a small distance from the particle, fully in the matrix. Nucleation in this layer resulted in extensive plasticity and void growth. Because of this local ductility, the fracture toughness of the composite was increased when compared with conditions without a ductile interfacial layer near the particles. Upon overageing, the interfacial precipitates (concentrated at the interface between matrix and reinforcement) grow, leading to high stresses over the interface and resulting in interfacial debonding.

Another feature which might be observed in the interfacial region between particle and matrix is the formation of a layer of matrix material around the particles with a higher hardness than the matrix material itself. Das *et al.* [29] observed magnesium enrichment in the interfacial region for an MMC based on the AA6061 alloy reinforced with Al_2O_3 particles. This magnesium enrichment was attributed to the presence of a MgAl_2O_4 spinel formed during fabrication.

From the above sub-sections it is clear that a lot of questions remain how to produce MMCs with optimum properties for specific applications. Although extensive research into the various microstructural variables has already been done, a lot of results found are contradictory, probably due to an incomplete control of all relevant parameters during processing and characterisation. Another way of investigating fracture behaviour in MMCs, is by calculating this behaviour with finite element models in computer simulations. In such models all parameters are fully controlled, but one can not be sure that all relevant

mechanisms are included or true material properties may not be known in sufficient detail. The next section deals with modelling fracture in MMCs.

1.5 Finite Element Modelling of Fracture in MMCs

The principle aim of computational modelling of multiphase materials like MMCs, is deducing their overall (mechanical) behaviour from the individual material behaviour of their components and the interfaces between them. When realistic phase distributions are used, the analysis of spatial variations in the microfields in actual constructions will exceed present computational capabilities. Therefore, the majority of descriptions of inhomogeneous materials are based on one of the following approximations [30]:

- mean field approaches,
- unit cell approaches, or
- embedded cell approaches.

In mean field approaches, the microfields within each constituent are approximated by the mean total strain and stress fields in each phase. These approaches have been successful in describing the thermo-elastic response of inhomogeneous materials. In unit cell approaches, a model material with a spatially periodic phase arrangement approximates the inhomogeneous material. Unit cell methods are often used for material characterisation of inhomogeneous materials in the non-linear range, but they can also be employed to derive micromechanically based constitutive models. With embedded cell approaches, the inhomogeneous material is approximated by a model material consisting of a core containing a discrete phase arrangement (often rather similar to a unit cell) that is embedded within some outer region to which far field loads or displacements are applied. Like periodic field approaches, these approaches can resolve local stress and strain fields in the core region at high detail.

In this thesis the unit cell method is chosen to model the fracture behaviour of aluminium-based MMCs, since it is the most widely and successfully applied approach.

Using the unit cell approach, damage evolution in terms of the description of the failure probability of individual particles can be analysed. To investigate the role of particle-particle interactions and the spread of damage in MMCs, a Gurson-like approach which is based on spherically symmetric deformations around a single spherical void is applied. Gurson [31] studied microscopic voids in materials and derived a set of modified constitutive equations for elastic-plastic materials. The Gurson model describes damage by means of one single scalar variable, namely the void volume fraction. Such an approach neglects many effects related to the individual voids, such as size, shape, orientation and distribution.

Tvergaard [32] modified the Gurson model by introducing additional empirical parameters, to bring predictions of the Gurson model at low volume fractions into closer agreement with full numerical analysis for periodic arrays of voids. Gurson's as well as the modified Gurson model have been applied extensively on steel alloys [33-35] and sometimes on aluminium alloys [36, 37] and MMCs [121-123]. In this thesis, the modified Gurson model is used, whereby it is assumed that broken ceramic particles in MMCs provide voids in the surrounding ductile matrix material, resulting in the void volume fraction being dependent on the volume fraction of failed reinforcing particles.

1.6 Scope of this Thesis

In this thesis, the mechanical behaviour of various MMCs, which are all based on the AA6061 aluminium alloy and are reinforced with Al_2O_3 particles, is being investigated experimentally using a range of techniques, as well as numerically using finite element models. By performing fracture toughness experiments in combination with fractographic analyses of the fracture surfaces, more understanding about occurring failure mechanisms in MMCs is obtained. In spite of a lot of assumptions which have to be made, the experimentally obtained results are implemented in finite element models to simulate the mechanical behaviour. By doing so, it is possible to investigate the influence of various variables such as reinforcing particle size, reinforcement volume fraction and matrix ageing condition in isolation. The ultimate aim is to be able to obtain optimum mechanical properties for specific (industrial) applications.

Since both experiments and calculations were performed to achieve this aim, this thesis is arranged in two parts, namely part A, an experimental part devoted to material behaviour and part B, a theoretical part on modelling fracture mechanical behaviour. In part B also the synthesis of experiments and calculations is described.

The experimental part A consists of three chapters. In chapter 2 “Precipitation Kinetics in AA6061 and an AA6061 Based MMC”, the MMC matrix response to heat treating is compared with that of an unreinforced aluminium alloy of approximately the same composition using Differential Scanning Calorimetry. In chapter 3 “Nanoindentation Study into the Mechanical Behaviour of MMC Matrix Material”, the same approach as in the previous chapter is used: possible changes in matrix response due to the addition of reinforcing ceramic particles in various heat treatment conditions are investigated. Chapter 4 “Fracture Mechanical Experiments” describes fracture toughness experiments, on a commercial MMC and on a range of self-made experimental MMCs. Furthermore, the fracture behaviour of unreinforced matrix material has been measured too.

Part B contains two chapters using results from chapters 2 to 4 in modelling the mechanical behaviour as it was experimentally tested. In chapter 5 “Modelling Particle Fracture Using Weibull Statistics”, variables such as loading triaxiality, particle size, particle properties and matrix alloy properties are varied to investigate the parameter dependence of particle fracture. Chapter 6 “Modelling Damage in MMCs using Gurson's Model”, uses the modified Gurson model to calculate the fracture toughness of MMCs as they were used in the actual experiments, and compares the calculated fracture toughness values with the values found experimentally.

part A

Investigation of Material Behaviour

2

PRECIPITATION KINETICS IN AA6061 AND AN AA6061 BASED MMC

2.1 Introduction

The matrix of aluminium metal matrix composites (MMCs) is often of the precipitation hardenable type, responding to a solutionize-quench-age heat treatment. It has been reported that an increase in strength in an AA6061 alloy due to age hardening is positively affected by the introduction of reinforcing ceramic particles [38, 39]. As the reinforcements are thought not to affect the overall chemistry of the matrix, the effect must be due to a stimulated precipitation response of the matrix. The stimulation of the precipitation process is attributed to vacancy annihilation and a high dislocation density resulting from differential thermal expansion as well as stimulated nucleation at the particle-matrix interface.

The nature of this stimulated precipitation is not easy to predict, in particular not for AA6xxx base alloys containing both Mg and Si where even for the unreinforced base material the exact order of the various precipitation reactions is subject of debate [39-42]. Edwards *et al.* [41] proposed that the precipitation sequence in an Al-Mg-Si alloy consists of the formation of separate clusters of Mg and Si atoms, co-clusters of Mg and Si atoms, small equiaxed precipitates, β'' precipitates, β' and B' precipitates, and finally, β -Mg₂Si precipitates. Dutta and Allen [42] found the precipitation processes in an AA6061 alloy to be associated with vacancy-silicon clusters, GP-I zone, GP-II zone, β' and β -Mg₂Si formation. Papazian [39] did not find clusters or GP-zones in AA6061. So the precipitation processes in AA6061 alloys and their kinetics remain largely unknown.

Therefore, this chapter describes an investigation into the precipitation kinetics of an AA6061 alloy and the effects of Al₂O₃ reinforcements on the kinetics. Differential Scanning Calorimetry (DSC) was selected as the principal technique, because this allows rapid but accurate evaluation of the kinetics of the various reactions taking place.

2.1.1 Thermal Analysis of Phase Transformations

Thermal analysis is a well known and understood discipline for the analysis of phase transformation kinetics. DSC is one of such techniques. In the DSC technique, the difference in heat flows required to heat or cool the sample to be investigated at a constant rate and that to heat or cool a reference sample is measured as a function of temperature, see figure 2.1.

The sample to be investigated is placed in a sample cup in a sample cup holder. The other sample cup holder is either kept empty or filled with reference material of approximately the same weight as the investigated sample.

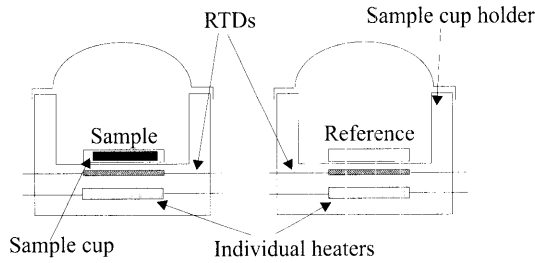


Figure 2.1
Schematic representation of the DSC method [43]

DSC equipment involves two parallel temperature measurement systems [44], whereby the sample cup and the reference cup are placed on separate holders. Each cup holder is provided with a separate heating element and RTD (resistance temperature detector for temperature measurement) with feedback to the heaters. The sample and reference cups are heated at a fixed rate. During heating, the temperature difference is constantly measured. In case of a difference, there is a reduction of heat input to one cell while adding heat to the other, so as to maintain a zero temperature difference between the sample and reference, establishing a "null balance".

Endothermic and exothermic reactions result in heat flow changes, giving information about the transformations in the examined material. Since precipitation of a phase results in a release of energy, this results in exothermic peaks, whereas melting or dissolution of a phase results in endothermic peaks due to energy absorption.

2.1.2 Kinetic Analysis of Phase Transformations

A DSC run yields the heat flow (heat release or absorption), dH/dt , due to a phase transformation as a function of temperature under a constant heating rate. The partial area divided by the total area, A , under a DSC peak is taken as equal to the fraction, y , of the transformation completed at a given time, thus:

$$y = \frac{1}{A} \int_0^t \frac{dH}{dt} dt \quad (2.1)$$

or in differential form:

$$\frac{dH}{dt} = A \frac{dy}{dt} \quad (2.2)$$

Hence, dividing the partial DSC output by the area under the peak results in a plot of dy/dt , which is a convenient function to fit to kinetic equations. Many studies [45-47] have shown

that the results of continuous heating experiments can be used to obtain a good kinetic description of the process by assuming that the rate of transformation is given by:

$$\frac{dy}{dt} = k(T)f(y) \quad (2.3)$$

where $k(T)$ is the rate constant defined as $k(T) = k_0 \exp(-E/RT)$, where k_0 , E , R and T denote the pre-exponential factor, the activation energy, the gas constant and the absolute temperature, respectively. $f(y)$ is a function depending on the reaction mechanism of the phase transformation. In heterogeneous solid-state transformations, $f(y)$ is often approximated by an n -order kinetic model [45, 48, 49]:

$$f(y) = n(1-y) \left[\ln \left(\frac{1}{1-y} \right) \right]^{[(n-1)/n]} \quad (2.4)$$

The kinetics of heterogeneous solid-state transformations under non-isothermal conditions can be described by:

$$y = 1 - \exp(-\beta^n) \quad (2.5)$$

where n is a numerical exponent and β is the state variable fully determining the state of transformation. In non-isothermal transformations, T and $k(T)$ depend on t . There are several ways to extract the kinetic parameters from equation (2.3). For a constant heating rate $\phi = dT/dt$, after rearranging equation (2.3), the following expression for the relation between the rate of transformation and the activation energy of the process is obtained:

$$\ln \left[\left(\frac{dy}{dT} \right)_{y_i, \phi_j} \right] = \ln [f(y)k_0] - \left(\frac{E}{R} \right) \frac{1}{T_j} \quad (2.6)$$

where y_i is the fraction transformed for all reactions taking place at temperature, T_j , when the heating rate is ϕ_j . A plot of $\ln[(dy/dT)_{y_i, \phi_j}]$ against $(1/T_j)$ should yield a straight line of slope $(-E/R)$, from which the value of the activation energy of the process can be calculated without recourse to any special model for the transformation kinetics.

Mittemeijer and co-workers [50, 51] used the so-called Kissinger-like method to extract kinetic parameters from data obtained in non-isothermal experiments. Using an approximation to the integral:

$$\beta = \int k(T)dt \approx \frac{T^2 R}{\phi E} k \quad (2.7)$$

the following expression was derived for a fixed stage of transformation, y_f :

$$\ln \frac{T_{y_f}^2}{\phi} = \frac{E}{RT_{y_f}} + \ln \frac{E}{Rk_0} + \ln \beta_{y_f} \quad (2.8)$$

They further showed that the temperature, T_i , where the reaction rate has a maximum (*i.e.* the temperature corresponding to the point of inflection on the y - T curve), is an appropriate substitute for T_{yf} , the temperature for a fixed stage of transformation. It has been shown [50] that for non-isothermal kinetics $\beta_{Ti} \cong 1$, so the last term in equation (2.8) could be neglected without incurring significant error. The slope of the plot of $\ln(T_i^2/\phi)$ against $(1/T_i)$ yields the activation energy.

For partially superimposed precipitation transformations, it is assumed that the heat release detected by the calorimeter may be taken as the sum of the heat flows of each transformation, thus:

$$\frac{dH}{dt} = \frac{dH_1}{dt} + \frac{dH_2}{dt} \quad (2.9)$$

Combining equations (2.2) and (2.9) and $\phi = dT/dt$, results in:

$$\frac{dH}{dt} = A_1 \frac{dy_1}{dT} + A_2 \frac{dy_2}{dT} \quad (2.10)$$

Using equation (2.5) and taking $\beta_i = (T^2/\phi)(R/E_i)k_{0i}\exp(-E_i/RT)$ we obtain:

$$\frac{dy_i}{dT} = n_i \beta_i \exp(-\beta_i^n) \left(\frac{2}{T} + \frac{E_i}{RT^2} \right) \quad (2.11)$$

Combining equations (2.10) and (2.11), the coefficients A_i , n_i , k_{0i} and E_i can be determined from the DSC trace by using the non-linear regression version of Marquart's method of minimisation of least squares error of experimental data to equation (2.10), upon reasonable estimations of the initial values.

2.2 Experimental Procedure

The AA6061 aluminium alloy used in experiments was produced by Cressona Aluminum Company, the USA. The material was extruded to a diameter of 63.5 mm and delivered in T651 condition. The investigated MMC was an AA6061 based MMC reinforced with 20 vol.% Al_2O_3 particles, produced by Duralcan USA. It was produced via the stir casting process, whereby the reinforcing powder is added and mixed into the molten matrix through melt agitation by a stirrer. After stir casting, the material was extruded into a rod with 2 inch diameter. The chemical composition of AA6061 and MMC matrix material, as listed in table 2.1, were measured using X-ray fluorescence (XRF).

Table 2.1
Chemical composition of the materials tested in weight percentage

| Material | Mg | Si | Fe | Cu | Cr | Mn | Ti | Zn | Pb | Ni |
|----------|------|------|------|------|------|-------|------|-------|-------|-------|
| AA6061 | 0.89 | 0.63 | 0.36 | 0.34 | 0.10 | 0.100 | 0.03 | 0.020 | 0.020 | 0.010 |
| MMC | 1.11 | 0.45 | 0.05 | 0.23 | 0.09 | 0.001 | 0.01 | 0.003 | 0.008 | 0.006 |

Samples for DSC analysis in the form of discs 6 mm in diameter by 0.8 mm thickness, with an approximate weight of 46 mg, were cut from the extruded rods and were solution treated at 530°C for 1 h in air, followed by quenching into water of 12°C (WQ). Then, the discs were examined immediately in a Perkin-Elmer DSC7 over a temperature interval ranging from 0 to 530°C using a set of heating rates up to 40°C/min, whereby dry nitrogen was passed through the cell to avoid oxidation. The Perkin-Elmer DSC7 Differential Scanning Calorimeter was connected to a DEC Personal Workstation via a TAC7/DX Thermal Analysis Instruments Controller. With Perkin-Elmer Series/UNIX Thermal Analysis System software, the DSC7 can be used for calorimetric measurements and characterisation and analysis of thermal properties of materials.

Efforts were made to ensure that the delay between WQ treatment and DSC analysis was as short as possible. For comparison, WQ samples, stored in a fridge for various periods were also analysed. Typically, at least three DSC samples were made for each heat treatment condition. The results obtained were found to be highly reproducible. AA6061 and composite samples aged for 10 h at 400°C with a mass close to that of the specimen were found to be very suitable as reference materials. The baselines were obtained by subtracting the output of the reference measurements from that of the specimen.

2.3 Results and Discussion

2.3.1 Differential Scanning Calorimetry

The DSC thermograms, as shown in figure 2.2, were obtained at heating rates of 5, 10, 20 and 40°C/min over the range 0-530°C. The average peak temperatures and the heat effects associated with these transformations are shown in tables 2.2 and 2.3, respectively.

For the solutionized and freshly quenched AA6061 the traces show that there are four exothermic peaks in the interval 0-530°C. For a heating rate of 10°C/min, one peak is at 83°C (A), two partially overlapping peaks close to 243°C (B) and 298°C (C), and one at 495°C (D). Furthermore, peak B is found to be a doublet of B₁ and B₂. All peaks are found to shift to lower temperatures at lower heating rates, indicating that the rate of phase formation is controlled by the reaction kinetics. In line with other studies [41, 42, 52] the precipitation events in the freshly solutionized and quenched AA6061 are assigned to take place in the following sequences: supersaturated solid solution, vacancy related clusters (exothermic peak A), GP-I and GP-II (β'') zone formation (peak B₁, B₂), β' formation (peak C) and β -Mg₂Si formation (peak D).

The calorimetric measurements on the MMC samples show a similar behaviour. The precipitation sequences and the shapes of the peaks do not change, but some aspects of the reactions are altered. The precipitation peaks are slightly advanced to lower temperatures compared with those for monolithic AA6061 at the same heating rate. The area and the height of all peaks are smaller than those of the corresponding peaks in AA6061. As shown in table 2.2, for a heating rate of 10°C/min, peak A, peak B₂ and peak C shift to lower temperature by 2.2, 1.4 and 7°C, respectively. The ratios of the volumes of peak A, peak B and peak C in the MMC to those of corresponding peaks in AA6061 are 0.27, 0.81 and 0.54, respectively.

The peak ratio for peak β'' (peak B₂) should be interpreted in the light of the difference in chemical composition between the AA6061 alloy and the AA6061 matrix of the MMC. Using the data provided by reference [53], the maximum volume fractions β'' (peak B₂) formed in the same amount as AA6061 and the matrix of the MMC can be calculated to be 1.36 and 1.27 vol.%, respectively. Taking into account that the MMC contains 20 vol.% Al₂O₃, the ratio of the β'' volume fraction in MMC to that in AA6061 should be 0.75 (*i.e.* $0.8 \times 1.27/1.36$). This is less than the observed ratio of 0.81, which means that the presence of Al₂O₃ particles promotes the formation of β'' . These observations indicate that the addition of a reinforcing phase accelerates ageing of MMC precipitation process relative to the matrix alloy, decreases the volume fractions of peaks A and C, but increases the volume fraction of peak B.

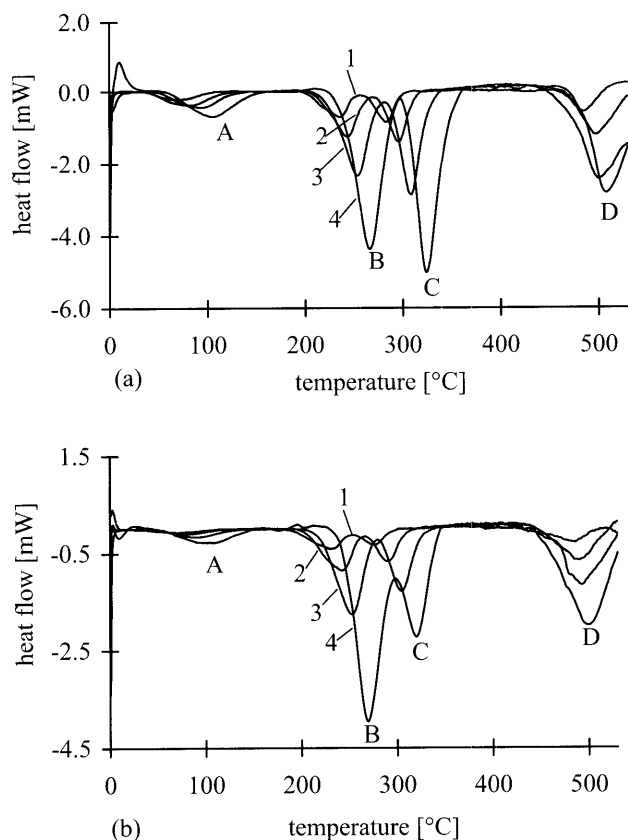


Figure 2.2

DSC thermograms for various heating rates, showing four precipitation peaks A through D: (a) as-quenched AA6061 and (b) as-quenched AA6061 with 20 vol.% Al₂O₃. (1) 5°C/min; (2) 10°C/min; (3) 20°C/min; (4) 40°C/min

2. Precipitation Kinetics in AA6061 and an AA6061-Based MMC

Table 2.2

DSC peak temperatures [°C] as a function of heating rate

| Heating rate [°C/min] | Peak A | | Peak B ₁ | | Peak B ₂ | | Peak C | |
|--------------------------|--------|-------|---------------------|-------|---------------------|-------|--------|-------|
| | AA6061 | MMC | AA6061 | MMC | AA6061 | MMC | AA6061 | MMC |
| 5 | 71.2 | 70.4 | 214.9 | 209.6 | 233.6 | 230.8 | 285.5 | 276.7 |
| 10 | 82.8 | 80.6 | 218.2 | 221.0 | 242.8 | 241.4 | 298.2 | 291.2 |
| 20 | 93.8 | 89.7 | - | - | 253.5 | 252.5 | 308.8 | 304.7 |
| 40 | 105.6 | 102.4 | - | - | 266.3 | 269.1 | 324.2 | 320.5 |

Table 2.3

Total heat effects [J/g] of the DSC peaks at different heating rates

| Heating rate [°C/min] | Peak A | | Peak B | | Peak C | |
|--------------------------|--------|------|--------|------|--------|------|
| | AA6061 | MMC | AA6061 | MMC | AA6061 | MMC |
| 5 | 2.32 | 0.73 | 4.15 | 3.13 | 3.18 | 1.14 |
| 10 | 2.11 | 0.59 | 4.01 | 3.02 | 3.22 | 1.41 |
| 20 | 1.46 | 0.52 | 4.09 | 3.06 | 3.89 | 1.35 |
| 40 | 1.39 | 0.49 | 4.14 | 2.83 | 3.81 | 1.13 |

A closer look at the thermograms of both AA6061 and MMC for heating rates of 5 and 10°C/min suggests that peak B is an unresolved doublet. As shown in figure 2.3, the peaks B in the DSC traces at low heating rates can be separated with perfect fit for individual peaks to n -order reaction kinetics (equation (2.4)). The doublet cannot be resolved at higher heating rates. Whether peaks B₁ and B₂ fully overlap or whether one of them disappears with increasing heating rate is still unknown.

AA6061 and its composite are very sensitive to the delay time between quenching and the DSC experiments. Samples were stored in a fridge at -5°C. Figure 2.4 shows the effect of the delay time on the DSC runs of AA6061. The peak A temperature shifts to higher temperatures with progressive delay in the fridge, with the onset temperature being unchanged. A delay time leads to the formation of an endothermic peak A', the longer the delay, the bigger peak A'. Peak B shifts to higher temperatures and seem to become one peak, B₂. The temperature of peak C does not change, but the height of the peak is reduced. These observations indicate that delay supports peak B₂ formation but retards the formation of peak C. Similar effects were found for the MMC.

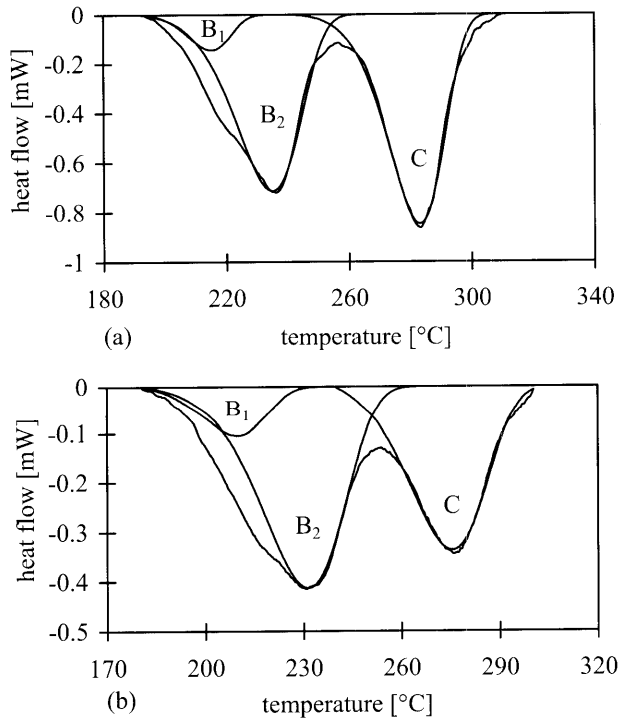


Figure 2.3

Part of the DSC traces after deconvolution showing peak B consisting of two unresolved exotherms, B₁ and B₂ (deconvoluted by equation (2.11)) for a heating rate of 5°C/min (a) AA6061 and (b) MMC

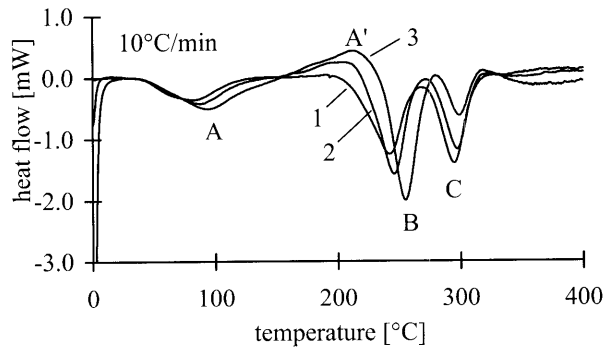


Figure 2.4

The effect of delay time in the fridge on the DSC thermograms of AA6061. (1) no delay; (2) delay for 24 h; (3) delay for 48 h

2.3.2 Kinetic Parameters

2.3.2.1 Varying Heating Rate Method (Equation (2.6))

The DSC peak designated A in figure 2.2 is assigned to the formation of vacancy-solute clusters. The fraction transformed of the phase, y , and the precipitation rate (dy/dT) , calculated from the DSC peak A using equations (2.1) and (2.2) are shown as a function of temperature in figure 2.5 for AA6061.

The y - T curves (figure 2.5(a)) have the expected sigmoidal shape and shift to higher temperatures with increasing heating rate, which implies a kinetically controlled transformation. The data extracted from figures 2.5 (a) and (b) are plotted in figure 2.6 for four values of y_i (0.2, 0.4, 0.6 and 0.8) using equation (2.6). The average slope of the four straight lines obtained from the $\ln[(dy/dT)_i \phi_i]$ versus $(1/T)$ plots yield the activation energy, E , for peak A formation.

Similar procedures and plots were used to calculate the activation energies for the transformation processes related to the other peaks. The kinetic parameters obtained for the two materials are summarised in table 2.4.

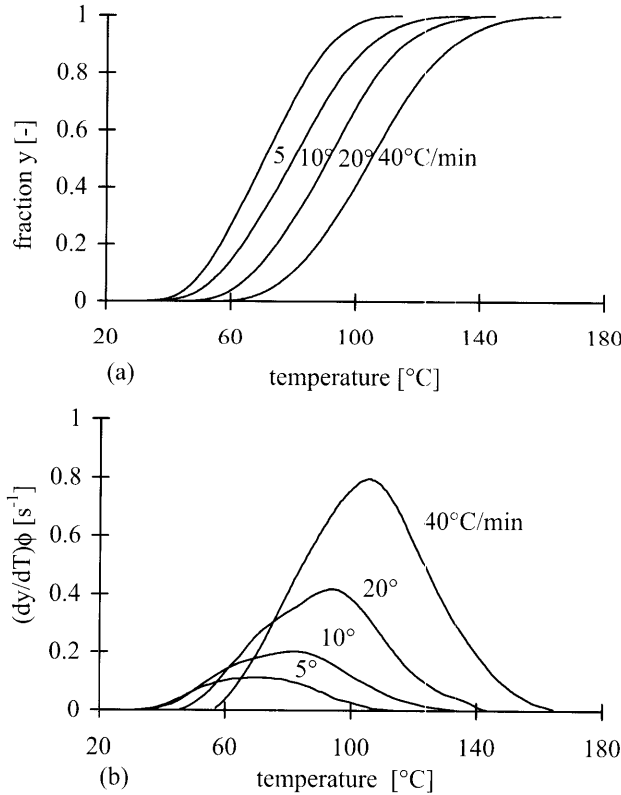


Figure 2.5

(a) The fraction y versus temperature curves and (b) $(dy/dT)\phi$ versus temperature, for peak A formation at different heating rates for AA6061

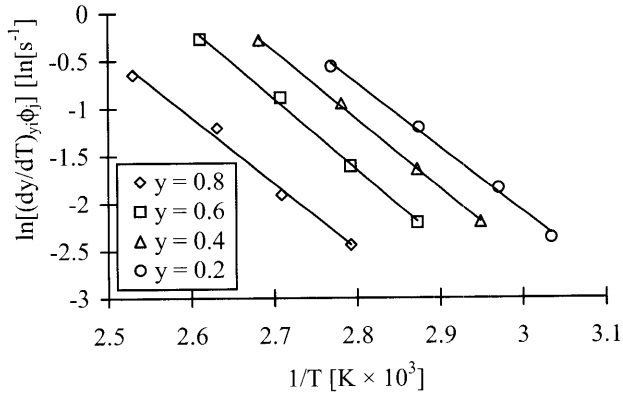


Figure 2.6
Plots of $\ln[(dy/dT)_{yi} \phi_p]$ versus the reciprocal temperature for peak A formation in AA6061 (after equation (2.6))

Table 2.4
Kinetic parameters for the transformations

| Parameter | Equation | Peak A | | Peak B ₂ | | Peak C | |
|----------------------------|----------|--------------------|--------------------|-----------------------|-----------------------|-----------------------|-----------------------|
| | | AA6061 | MMC | AA6061 | MMC | AA6061 | MMC |
| E [kJ/mol] | 2.6 | 60.5 | 65.5 | 129.8 | 114.1 | 123.9 | 122.8 |
| | 2.7 | 58.1 | 64.1 | 135.2 | 110.1 | 127.5 | 120.4 |
| k_0 [min ⁻¹] | 2.7 | 1.95×10^8 | 1.86×10^9 | 2.86×10^{13} | 7.06×10^{10} | 2.43×10^{11} | 6.63×10^{10} |

2.3.2.2 Kissinger-like Method (Equation (2.7))

It can be proved that the inflection point temperature, T_i , of the y versus T curves is the peak temperature in the DSC experiment. The average values of the peak temperatures for all peaks of the two materials are listed in table 2.2. By plotting $\ln(T_i^2/\phi)$ against $(1/T)$, as shown in figure 2.7, the effective activation energies for peaks in both materials were obtained (see table 2.4). These values agree very well with the results obtained from the varying heating rate method (equation (2.6)). Barring extrapolation errors, the pre-exponential factors, k_0 , were also calculated.

Kinetic parameters obtained by analysis of the calorimetric signal according to the n -order model given by equation (2.11) are listed in table 2.5 for heating rates of 5 and 10°C/min. The good agreement of the values between tables 2.4 and 2.5 shows that the phase transformations in AA6061 and MMC follow the n -order model, with n varying only modestly between 0.9 and 1.3.

Comparison of the results for AA6061 and MMC shows the following effects:

1. Precipitation of peak A in the composite requires a higher driving force than in the unreinforced alloy.

2. Precipitation Kinetics in AA6061 and an AA6061-Based MMC

2. The activation energy required for the precipitation of peak B₂ (GP-II) reduces from 135 to 110 kJ/mol in the composite.
3. The addition of Al₂O₃ does not change the activation energies for the formation of peaks B₁ and C (within experimental error).

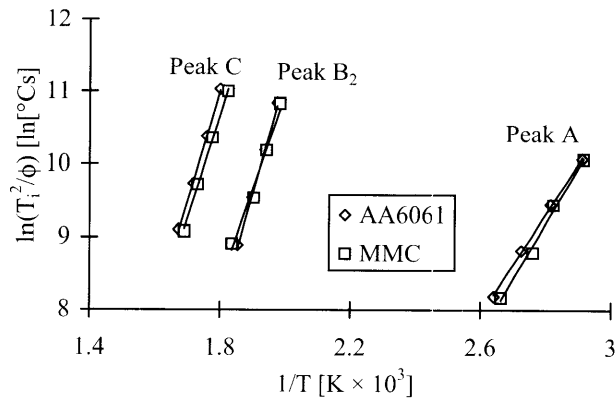


Figure 2.7
Arrhenius diagram for phase transformations in AA6061 and MMC

Table 2.5
Kinetic parameters by simulation according to equation (2.11)

| Parameter | Heating rate | Peak B ₁ | | Peak B ₂ | | Peak C | |
|----------------------------|--------------|----------------------|----------------------|----------------------|----------------------|----------------------|----------------------|
| | | AA6061 | MMC | AA6061 | MMC | AA6061 | MMC |
| \bar{E} [kJ/mol] | 5 | 92.5 | 93.6 | 127.5 | 110.9 | 127.4 | 126.6 |
| | 10 | 89.7 | 92.1 | 128.4 | 110.1 | 124.7 | 125.8 |
| k_0 [min ⁻¹] | 5 | 6.8×10^{11} | 6.9×10^{11} | 5.8×10^{14} | 6.5×10^{12} | 4.4×10^{13} | 5.0×10^{13} |
| | 10 | 7.1×10^{11} | 6.8×10^{11} | 7.6×10^{14} | 5.6×10^{12} | 3.1×10^{13} | 4.2×10^{13} |
| n | 5 | 1.235 | 1.011 | 0.975 | 0.943 | 1.224 | 0.914 |
| | 10 | 1.356 | 1.066 | 0.868 | 0.955 | 1.275 | 0.989 |

These effects will now be discussed in more detail.

The values of the activation energy for peak A formation obtained in the present study for AA6061 and MMC are 58 and 64 kJ/mol, respectively, and are in the range 41 - 66.9 kJ/mol, *i.e.* the migration energy of vacancies in Al-Cu alloys and Al-Cu-Mg alloys [48, 53]. When the alloy is quenched from the solution treatment temperature, excess vacancies are quenched in. In the presence of excess vacancies, diffusion of the solute proceeds at a rate equal to that for migration of the vacancies. Thus, peak A reflects diffusion of vacancies. It is believed that the relatively high dislocation density introduced by differential thermal expansion between the reinforcement and the matrix in the MMCs [40, 54] on quenching from the solution heat treatment temperature influences the precipitation kinetics in a complex manner. First, the dislocations and the particle-matrix interfaces give rise to vacancy annihilation, thus retarding the precipitation process and reducing the volume fraction of the precipitates formed. Second,

the high dislocation density and the particle-matrix interfaces act as nucleation sites for heterogeneous nucleation of the precipitation and offer high diffusivity paths for the solute in the composite and so promote the ageing process. Dislocations have been shown by both theoretical and experimental analysis [55] to serve as short-circuit paths for solute diffusion. In fact, at lower temperatures, dislocations can have little effect on the rate of zone formation because few atoms are near a dislocation and dislocations are stationary. With the temperature increasing the effect of dislocations would become more significant. Hence, with the vacancy concentration being lower in the MMCs than in the monolithic alloys, the height of peak A should be lower in the MMC. In a vacancy-deficient environment, the activation energy required for peak A formation would be higher than in the vacancy-rich counterpart. It is to be expected that the activation energy for peak A formation in the MMC is larger than that in the unreinforced alloy.

Comparing the kinetic parameters of peaks B₁ and B₂, the lower activation energy for peak B₁ implies that there is a lower kinetic barrier for its reaction to take place and initially it is the favoured transformation, as observed. The larger pre-exponential factor, often called the frequency factor, for peak B₂ implies that the jump rate of atoms across the interface of the β'' phase is large, so that if the kinetic barrier is surmountable, a comparatively large volume of β'' will result.

The activation energy for formation of peak B₁ is about 90 kJ/mol, which is much lower than the activation energies for migration of Si and Mg. (The activation energies for Si and Mg migration in bulk aluminium are 139 and 110 kJ/mol, respectively [56]). It can be inferred that the formation of peak B₁ is associated with vacancy-assisted diffusion of solute atoms. When the heating rate is increased, GP-I (peak B₁) formation should be at a higher temperature. However, when the temperature is high enough, the solute atoms get enough energy to surmount the higher kinetic barrier of GP-II, resulting in the formation of GP-II (peak B₂) at the expense of peak B₁.

The activation energy for peak B₂ formation in AA6061 is about 128 kJ/mol, approximately the value for migration of Si. That means that the formation of GP-II is a Si diffusion-controlled reaction. The addition of Al₂O₃ particles lowers the activation energy from 128 to 110 kJ/mol, equal to the activation energy for Mg diffusion. The reduction can be due to the extra dislocations acting as pipe-circuits for solute diffusion and/or the difference in the matrix composition. Mg is the excess alloying element in the MMC matrix.

The Al₂O₃ containing samples showed an acceleration of formation (peak C shifts to lower temperatures), but a reduction in the amount of β' phase formed. The activation energy does not change. This might be attributed to the higher Mg content in the matrix of the composite. The excess Mg (the ratio of Mg:Si in the β' phase is 1.68 [57]) in AA6061 makes the phase corresponding to peak C unstable [58]. Other factors may affect the height of peak C too, as the samples of AA6061 stored in the fridge seem to have the same effect on peak C. Whatever the mechanism, this observation shows that the relative proportions of β'' and β' will be significantly different in an Al₂O₃/AA6061 composite when compared with AA6061. The addition of Al₂O₃ particles biases the formation of the β'' , which contributes to strengthening, and hence increases the strength of the MMC.

The experimental findings in the storage time experiments can be explained by excess vacancy theory [59]. Upon quenching from 530°C, excess vacancies may cluster to form small voids, and then collapse into vacancy loops. These kind of vacancy loops (pre-clusters) would serve as nuclei for precipitates. If the alloy is placed in a temperature regime (ageing) that allows stable growth of the pre-clusters, the excess vacancies will be incorporated in pre-clusters. As pre-clusters grow to a critical (stable) nucleus size, clusters or zones form. The critical stable nucleus size depends on the ageing temperature. Dutta found in transmission electron microscope (TEM) micrographs that the initial stage of ageing in an AA6061 is similar to that in Al-Si alloys [42]. Experiments on precipitation in the Al-Si alloy show that on ageing formation of vacancy loops decorated with Si atoms precedes the actual Si precipitation, which becomes detectable only after 2 h of ageing at about 130°C [60]. It can be inferred that peak A in the DSC traces of the fresh samples of AA6061 reflects the formation of the vacancy loops. When a sample is stored in a fridge (about -5°C), vacancy loops decorated with solute atoms form and are of subcritical size. During a DSC run the pre-clusters continue to grow by vacancy-assisted solute atom clusters. The longer the delay, the larger the pre-cluster size. An increase in the pre-cluster size will result in an increase of the peak temperature [61]. If this model is tenable, peak A in the DSC traces of the delayed samples would reflect the vacancy-assisted solute atom clusters. As vacancy-assisted solute cluster formation takes place during a DSC run, the supersaturation of solute remaining in solution is diminished. When the supersaturation is further reduced as a result of rising temperature, the size at which a cluster becomes stable is increased. Because supplies of solutes and vacancies from the matrix cannot support the growth of clusters, the clusters start to dissolve leading to peak A'. So it is suggested that the precipitation sequence in the delayed AA6061 is vacancy-assisted solute atom clusters (peak A), solute cluster dissolution (peak A'), GP-II formation (β'') (*i.e.* peak B), β' formation (peak C) and β -Mg₂Si formation (peak D).

2.4 Conclusions

- Based on the DSC investigation, a precipitation sequence for AA6061, in the freshly water quenched state is proposed as : (i) vacancy related clusters; (ii) competitive formation of GP-I and GP-II (β'') zones; (iii) precipitation of the β' phase; (iv) formation of the β -Mg₂Si phase.
- The age-hardening sequence in the 20 vol.% Al₂O₃/AA6061 MMC is similar to that in the unreinforced AA6061 alloy.
- The precipitation transformations of the metastable phases in both AA6061 and the composite obey a first-order kinetic model, with $0.9 < n < 1.3$.
- The kinetic parameters for the formation of vacancy-related clusters, GP-I and GP-II (β'') zones, and β' phase precipitates calculated using the varying heating method and the Kissinger expressions are in good agreement.
- The addition of Al₂O₃ particles reduces the amount of peaks A and C formed in AA6061 and shifts the peak temperatures to lower temperatures.
- The addition of Al₂O₃ particles biases the formation of the β'' phase, which contributes to the strengthening and will increase the strength of the composite.

3

NANOINDENTATION STUDY INTO THE MECHANICAL BEHAVIOUR OF MMC MATRIX MATERIAL

3.1 Introduction

Macroscopic mechanical properties of MMCs are not only determined by the mechanical properties of the various constituents, but a considerable contribution is due to the behaviour of the particle/matrix interface. Stiffening and strengthening rely on load transfer across this interface, toughness is influenced by crack deflection and ductility is affected by relaxation of peak stresses near the interface. Some investigators have found that, as result of a heat treatment, the matrix regions adjacent to the reinforcement may exhibit a higher dislocation density when compared with matrix material further away from the interface due to mismatch of the coefficients of thermal expansion (CTE) between the matrix and the ceramic reinforcements. These CTE-dislocation effects influence the kinetics of precipitation. Matrix dislocations may act as nucleation sites for precipitates and a higher density facilitates precipitation formation. Furthermore, the dislocations may act as preferential paths for solute diffusion which can accelerate the ageing process [62-64].

Since the width of particle/matrix interfaces and the interparticle distances are of the order of micrometers, it is practically not possible to determine gradients in mechanical properties around the particles using conventional techniques. However, nanoindentation which measures the resistance to plastic deformation in very small volumes, may offer some indication of gradients in mechanical behaviour on the micrometer range. Because of this capacity, nanoindentation is often used to measure thin hard films [65]. However, Leggoe *et al.* [66] and Das *et al.* [29] used the method to study aluminium-based particle reinforced MMCs. In the latter investigation, a distinction was made between indentations in a particle, interface or matrix. Electron probe microanalysis (EPMA), indicated that magnesium enrichment occurred in the interfacial region between the particle and the matrix and the width of this phase increased with ageing time. This magnesium enrichment has been attributed to the presence of a MgAl_2O_4 spinel which formed during fabrication and which gave rise to a layer of matrix material around the particles with high hardness.

In this chapter, nanoindentation testing was used to measure the hardness and elastic moduli profiles of AA6061 reinforced with Al_2O_3 in three different heat treatment conditions. Results are compared with nanoindentation measurements on unreinforced AA6061 in the same three

heat treatment conditions, to investigate possible changes in the mechanical behaviour of the matrix material due to the presence of the ceramic reinforcement.

3.2 Materials Used

The MMC used was produced via the stir casting process by Duralcan USA and consists of an AA6061-based alloy and 20 vol.% Al_2O_3 particles. AA6061, a widely used typical extrusion alloy containing Mg and Si as the principal alloying elements, is a very suitable alloy as matrix for MMCs since its properties can be adjusted by a suitable heat treatment. An unreinforced AA6061 alloy of almost identical composition was used as the reference system. The compositions of both the MMC matrix alloy and the reference AA6061 are listed in table 3.1.

Table 3.1
Chemical composition of the materials tested in weight percentage

| Material | Mg | Si | Cu | Ni | Mn | Cr | Fe | Ti |
|----------|-------|-------|-------|-------|-------|-------|-------|-------|
| AA6061 | 0.890 | 0.628 | 0.338 | 0.011 | 0.104 | 0.104 | 0.364 | 0.030 |
| MMC | 1.107 | 0.446 | 0.229 | 0.006 | 0.001 | 0.090 | 0.045 | 0.012 |

To produce known and reproducible precipitation structures in the AA6061 material as well as the MMC matrix material, all specimens were solutionized for 2 hours at 530°C followed by water quenching. In order to generate distinctly different precipitates in the matrix material, three different heat treatments were imposed making use of the results of a recent study on the precipitation kinetics in AA6061-based MMCs [67]. In that study, DSC curves were obtained for both homogenised AA6061 MMC and the reference alloy at a fixed heating rate of 5°C/min (see figure 3.1). In this figure, the peaks at around 60°C (labelled A) are related to Si clustering, those at around 230°C (labelled B) to β'' formation, those at around 280°C (labelled C) to β' formation and those at around 480°C (labelled D) to β - Mg_2Si formation.

In the present work, the condition of a matrix containing a maximum amount of β'' precipitates was created by linear heating the samples to a temperature of 255°C (condition B), using a heating rate of 5°C/min. A matrix containing a maximum amount of β' precipitates was created by linear heating the samples to a temperature of 305°C (condition C), using a heating rate of 5°C/min. To account for small differences in precipitation kinetics in the MMC and the reference alloy, the maximum annealing temperatures were adjusted according to table 3.2. The third heat treatment condition was an as-received T6-condition for the MMC, which consisted of solutionizing followed by 8 hours holding time at 175°C and an as-received T651-condition for the AA6061 alloy, which had additional stretching of ~2% before artificially ageing.

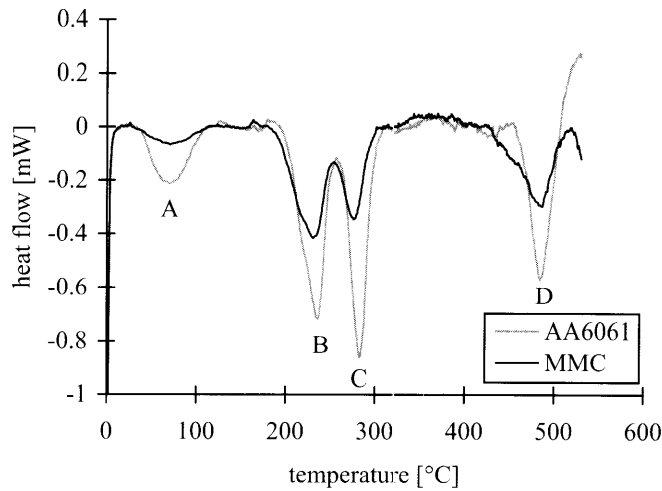


Figure 3.1
DSC traces of AA6061 and the Duralcan AA6061 with 20 vol.% Al_2O_3 particles, heating rate $5^{\circ}C/min$ [67]

Table 3.2
Water quench temperatures for the AA6061 alloy and the MMC

| Material | Temperature [$^{\circ}C$] |
|----------|-----------------------------|
| AA6061-B | 256 |
| AA6061-C | 309 |
| MMC-B | 254 |
| MMC-C | 300 |

3.3 Nanoindentation Procedure

The mechanical properties of both matrix material and MMC were investigated with a nanoindenter developed at Eindhoven University of Technology which continuously measures force and displacement as an indentation is made. The indenter in this instrument is a Berkovich diamond three-sided pyramid with a nominal angle of 65.3° and an area-to-depth function which is the same as that of a Vickers indenter. For each sample at least ten indentations were made with a maximum load of 30 mN and the indentations were separated by 20 μm . On the MMC sample in T6-condition, the maximum applied load for the indentations was 100 mN. The samples had to be polished up to 0.25 μm for the indenter to trace the surface, since any roughness affects the indentation curve. From the data obtained during unloading of the indentation, elastic displacements can be determined and from these measurements the elastic modulus, E , can be calculated. Furthermore, by removing the elastic

contribution from the total displacement, the hardness, H , can be calculated. A schematic diagram of a typical loading-unloading curve is shown in figure 3.2.

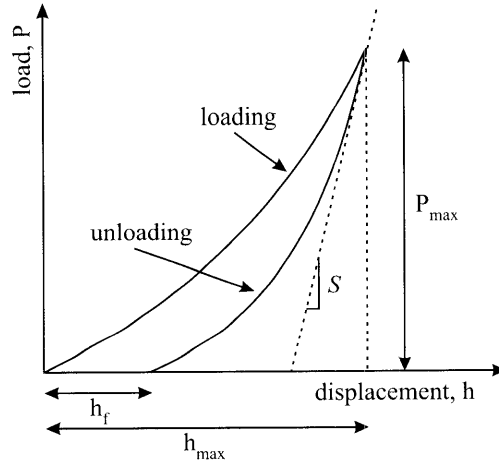


Figure 3.2

Schematic representation of a loading-unloading curve for a nanoindentation measurement; P_{max} is the load at maximum indentation, h_{max} is the indenter displacement at peak load, h_f is the final depth of the contact impression after unloading and S is the initial unloading stiffness

The displacement plotted in this figure represents the total displacement of the indenter relative to the initial position. This value is composed of both elastic and plastic displacements. An important observation concerns the shape of the hardness impression after the indenter is unloaded and the material elastically recovers [68]. In metals it turned out, that the impression formed by a conical indenter is still conical, but with a larger included tip angle. Doerner and Nix [69] observed that during the initial stages of unloading, the area of contact remains constant as the indenter is unloaded. The unloading stiffness is then related to the elastic modulus and the projected area of the elastic contact, A , through the following relationship:

$$S = \left(\frac{dP}{dh} \right)_{P=P_{max}}^{\text{unloading}} = \frac{2}{\sqrt{\pi}} E_r \sqrt{A} \quad (3.1)$$

where E_r is the reduced elastic modulus as defined in the following equation:

$$\frac{1}{E_r} = \frac{(1-\nu^2)}{E} + \frac{(1-\nu_i^2)}{E_i} \quad (3.2)$$

where E and ν are the Young's modulus and Poisson's ratio for the specimen and E_i and ν_i are the same parameters for the nanoindenter material. To determine the contact area at peak load, Oliver and Pharr [68] proposed a new method of analysis, since the behaviour of materials when indented by a Berkovich indenter can not be described using the flat punch

approximation [69]. Sneddon [70] has derived analytical solutions for punches of several geometries, including conical indenters. Like for the Berkovich indenter, the cross-sectional area of a conical indenter varies as the square of the depth of contact and its geometry is singular at the tip. Therefore, Oliver *et al.* [68] assume that the behaviour of a conical indenter gives a better description of the elastic unloading of an indentation made with a Berkovich indenter. The area of contact at peak load is then determined by the geometry of the indenter and the depth of contact, h_c . The indenter geometry can be described by an area function $F(h)$ which relates the cross-sectional area of the indenter to the distance from its tip, h . Given that the indenter itself does not deform significantly, the projected contact area at peak load can then be calculated from the relation:

$$A = F(h_c) \quad (3.3)$$

In addition to the elastic modulus, the hardness, H , defined as the applied load divided by the projected area of contact between the indenter and the sample can now be calculated:

$$H = \frac{P_{\max}}{A} \quad (3.4)$$

3.4 Results and Discussion

Typical loading-unloading indentation curves acquired for the MMC in T6 condition are shown in figure 3.3.

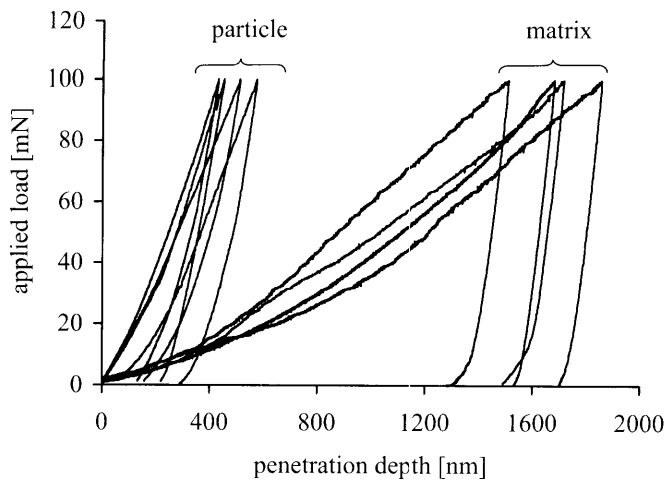


Figure 3.3

Indentation loading-unloading curves for an Al_2O_3 particle reinforced AA6061 MMC in T6 condition

In this figure, low penetration curves are attributed to indentations in particles and deep penetrations to those in the matrix. In contrast to Das *et al.* [29] this investigation did not reveal a third distinct group of indentations representing an existing 'interphase' between particle and matrix, for any of the heat treated MMCs. Little variation is observed for the particle indentations, more so for the matrix indentations. Indentation curves with deviant shapes were excluded from further interpretation. These curves were either a result of indentations in matrix material with underlying particles near the surface, indentations on particle-edges whereby the indenter slid off, or they were due to surface roughness of the sample. The latter is hard to overcome when investigating MMCs, since it turned out to be extremely difficult to level an MMC sample surface. A more detailed analysis of the shape of the indentation curves in relation to the position of neighbouring particles, showed a perfect example of a deviating curve which can be related to the indenter sliding off the ceramic particle, see figure 3.4.

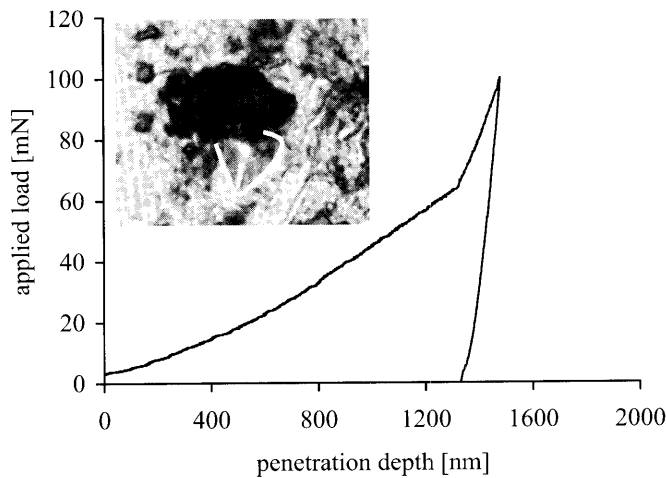


Figure 3.4

Indentation loading-unloading curve for an indent partially in the matrix and partially in a particle; the indentation is accentuated with a white line

Using dark field optical microscopy, most indentations in matrix material could be tracked down, whereas indentations in ceramic particles could not be found. After locating the position of the indentations in the matrix material with dark field, it was possible to switch to bright field and make photographs for further interpretation. Since the indentations in the MMC in T6 condition were made with a maximum load of 100 mN, the identification of the indentations was the easiest compared to the other MMCs and figure 3.5 shows such an indentation in the matrix.

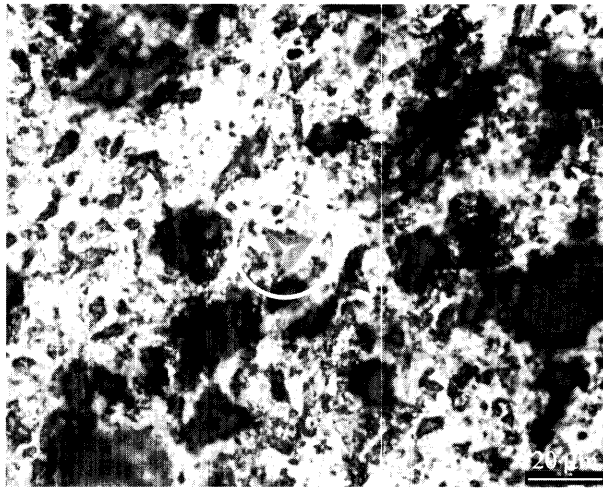


Figure 3.5

An example of an indentation in MMC matrix material in T6 condition

Since Mg enrichment of an interfacial region would lead to magnesium depletion in the matrix further away from the particles and thus reduce the age hardening effects in these regions [29], this would lead to a correlation between the measured hardness in the matrix and the distance to the nearest reinforcing particle. For the successful matrix indentations, this distance was measured using the photographs made with bright field optical microscopy, but no correlation between hardness and distance to the nearest Al_2O_3 particle was found. From figure 3.5, it can be seen that an indentation with a maximum load of 100 mN takes up approximately 10 μm . Although measurements by Das *et al.* [29] were done with a maximum load of 30 mN, it is hard to understand that they were able to measure exactly in this interfacial layer without encountering problems similar to the those found in this investigation as shown in figure 3.4.

To confirm the preferential segregation of Mg near the particle/matrix interface, linescans were made with a SEM equipped with EDS (Energy Dispersive Spectrum) facilities. Figure 3.6 shows such a linescan for the MMC material in the T6 condition. The box diagram at the top of the figure shows the translation of the chemical composition into the spatial distribution of the constituent phases; for example, the particles can be recognised by the increase of oxygen and the decrease of aluminium. Clear indications of Mg enrichment near particles were obtained. The average thickness of this Mg rich zone could not be established exactly, but was estimated to be approximately 4 μm . Such a value is in good agreement with data by Das *et al.* [29], who reported values ranging from 2 - 5 μm depending on annealing time. The limited width of the Mg rich zone explains the absence of typical 'interphase' indentations in our work, but also raises serious questions about the correctness of the 'interphase' indentations as reported by Das *et al.*. This thought is also supported by the fact that the Mg content in the MMC investigated here is even higher than that in both MMCs investigated by Das *et al.*. They investigated two MMCs, one consisting of AA6061 reinforced with 15 vol.% angular Al_2O_3 particles and the other was reinforced with 20 vol.% spherical Al_2O_3 particles.

The first MMC contained 0.752 wt.% Mg and the latter 0.704 wt.% Mg, whereas our MMC contained 1.107 wt.% Mg.

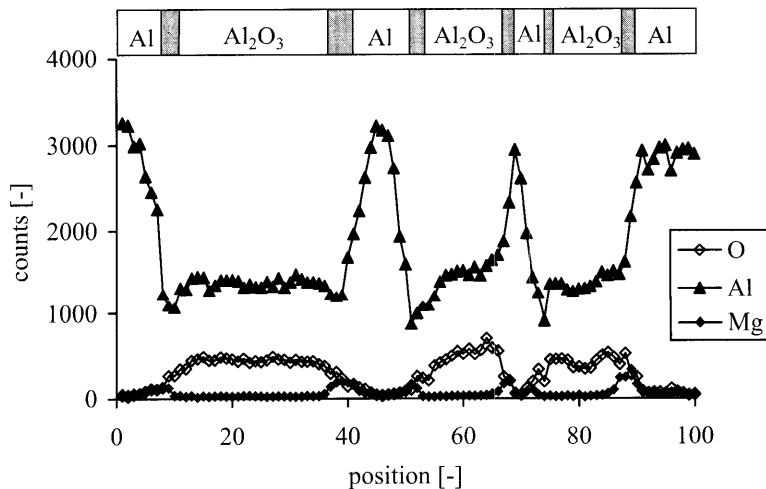


Figure 3.6
Linescan on AA6061-based MMC with 20 vol.% Al_2O_3 particles in T6 condition; Mg enrichment is represented with the grey boxes in the upper bar

Average elastic moduli and hardness values calculated for both the MMC and matrix material in all three heat treatment conditions are given in table 3.3. In the case of MMCs a distinction between matrix and particles could be made. The elastic moduli were determined from the linear fit to the initial points of the unloading part of the indentation curves and the hardness values were determined from the maximum force and plastic depth of the penetrations. In accordance with Das *et al.* [29], the calculated data in table 3.3 exhibits a relatively small scatter for indentations in the matrix, but the data for the Al_2O_3 particles show a much wider scatter. This is thought to be due to the presence of cracks and pores in the particles and the high hardness of the material itself.

The elastic moduli of the particles were lower than those reported in the literature, *i.e.* approximately 380 GPa [71, 72]. Since the elastic modulus in the nanoindentation experiments is determined by a linear fit to the initial points of the unloading curve, an underestimation might be a result of a stronger curvature in the unloading curve for indentations in the particles. However, another plausible explanation may be the fact that the particles are embedded in a soft matrix. So, when an indentation in a particle is made, the soft material underneath the particle will reduce the apparent elastic modulus value.

When analysing the hardness data and indentation curves for the MMC matrix material and the unreinforced AA6061 alloy (taking into account the experimental error), practically the same trends in hardness as a function of heat treatment are observed. For the base AA6061 material Vickers microindentation measurements were performed too and table 3.3 shows that

3. Nanoindentation Study into the Mechanical Behaviour of MMC Matrix Material

the hardness values correspond well to those found using the nanoindentation technique. It can be seen that for the matrix and particles in the MMC and the reference alloy the highest hardness values are obtained in condition B when compared with conditions C, T651 and T6.

Table 3.3

Calculated elastic moduli and hardness values for matrix and particles in AA6061 with 20 vol.% Al_2O_3 and in an AA6061 alloy as function of heat treatment

| Material | Condition | Matrix | | $H_{Vickers}$ [HV] | Particle | |
|-----------------------------------|-----------|-------------|-----------------|--------------------|--------------|--------------|
| | | E [GPa] | H [GPa] | | E [GPa] | H [GPa] |
| AA6061 | T651 | 92 ± 4 | 1.14 ± 0.05 | 100.37 ± 2.38 | | |
| | B | 89 ± 4 | 1.20 ± 0.04 | 112.21 ± 4.42 | | |
| | C | 90 ± 3 | 0.99 ± 0.05 | 84.97 ± 2.14 | | |
| AA6061 + 20 vol.% Al_2O_3 | T6 | 91 ± 6 | 0.97 ± 0.17 | | 214 ± 44 | 14 ± 4.5 |
| | B | 88 ± 2 | 1.17 ± 0.03 | | 197 ± 53 | 15 ± 3.5 |
| | C | 90 ± 10 | 1.03 ± 0.05 | | 213 ± 38 | 11 ± 0.9 |

Unlike literature reported [29, 66, 73], no indication of significantly different mechanical behaviour of matrix material near a ceramic particle was found in this investigation. Hence, the shapes of the indentation curves for the MMC matrix and unreinforced AA6061 reference material for corresponding heat treatments can be compared in detail, see figure 3.7. Average curves for AA6061 in T651 and B condition show a perfect overlap with the MMC in B condition (the MMC in T6 condition was left out here since this was indented with a load of 100 mN). Taking into account the small differences in yield strength and hardening exponent determined for these two conditions from tensile testing experiments, this good overlap is not surprisingly, *i.e.* the yield strengths for T651 and B condition are 295 MPa and 328 MPa respectively and the hardening exponents are 15.8 and 15.6 respectively (see also table 4.5).

In the C condition the loading curves for both AA6061 and the MMC vary somewhat, but the unloading curves again show a good overlap. The fact that these curves differ from the T651 and B condition can also be related to the yield strength and the hardening exponent of this heat treatment condition which are much lower, *i.e.* 200 MPa and 7.9 respectively.

The fact that hardly any differences are found in the mechanical behaviour of the MMC matrix material in comparison with the AA6061 reference alloy, makes it permissible to perform finite element calculations in which the matrix behaviour is assumed to be the same as that of the aluminium alloy without ceramic reinforcements.

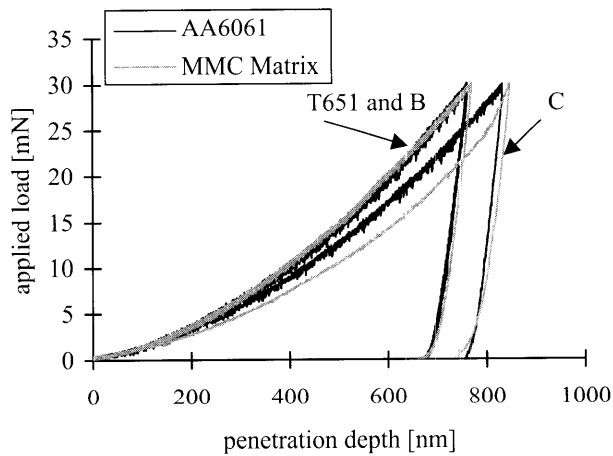


Figure 3.7

Comparison of the shapes of the indentation curves in the various heat treatment conditions; black lines represent the AA6061 alloy and grey lines the matrix of the MMC

3.5 Conclusions

- Hardness and elastic moduli of matrix and particles in aluminium-based MMCs can be determined using the nanoindentation technique, but one should be cautious about the exact values found.
- Although Mg enrichment was observed in this investigation, it was not possible to measure the hardness and the elastic modulus of this interfacial layer as a function of the various heat treatment conditions.
- When comparing results of AA6061 reference material with the behaviour of an AA6061 matrix in an MMC in three different heat treatment conditions, it turned out that there are hardly any differences in calculated elastic moduli and hardness values. So, when modelling the mechanical behaviour of MMCs using the finite element method it is permissible to assume the MMC matrix behaving similar as the same aluminium alloy without ceramic reinforcements.

4

FRACTURE MECHANICAL EXPERIMENTS

4.1 Introduction

Fracture mechanical behaviour of a precipitation hardening aluminium alloy AA6061 and AA6061-based metal matrix composites (MMCs) is being investigated using both tensile and fracture toughness experiments. In tensile experiments, material properties such as the elastic modulus, the yield strength, the ultimate tensile strain and the hardening exponent are determined. The plane strain fracture toughness (K_{Ic}) characterises the crack growth and fracture behaviour of materials and is therefore chosen to be a suitable property to determine what flaws are tolerable in an actual structure under given conditions.

Tensile tests were only performed on unreinforced AA6061 material, since it turned out to be impossible to machine the MMCs into suitable tensile specimens. The fracture toughness experiments were performed on AA6061, serving as reference material for the matrix of the MMCs, on commercial Duralcan MMC and on experimentally manufactured MMCs. The Duralcan MMC was tested in various heat treatment conditions, whereas the experimental MMCs were tested with various volume fractions of Al_2O_3 particles.

This chapter describes the investigated materials, the experimental set-up and the various testing methods used to calculate the fracture toughness. Finally, the results are discussed.

4.2 Materials

4.2.1 Commercial Materials

The AA6061 aluminium alloy was produced by Cressona Aluminum Company, the USA. The material was extruded to a diameter of 63.5 mm and delivered in T651 condition. The chemical composition was determined with X-ray fluorescence and is given in table 4.1. The mechanical properties as they were found in literature [74] are listed in table 4.3.

Table 4.1

Chemical composition of AA6061 in weight percentage

| Mg | Si | Fe | Cu | Cr | Mn | Ti | Zn | Pb | Ni | Al |
|------|------|------|------|------|------|------|------|------|------|------|
| 0.89 | 0.63 | 0.36 | 0.34 | 0.10 | 0.10 | 0.03 | 0.02 | 0.02 | 0.01 | rest |

The commercial MMC investigated (see figure 4.1) was an AA6061 based MMC reinforced with 20 vol.% Al_2O_3 particles, produced by Duralcan USA. It was produced via the stir casting process, whereby the reinforcing powder is added and mixed into the molten matrix through melt agitation by a stirrer. After stir casting, the material was extruded into a rod with 50.8 mm diameter. Chemical composition of the matrix material, measured using X-ray fluorescence and mechanical properties found in literature [75] are given in tables 4.2 and 4.3 respectively.

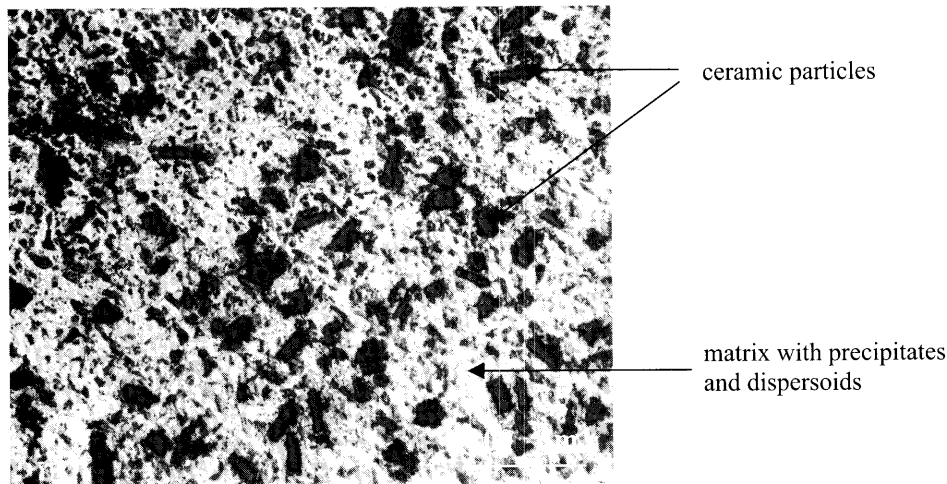


Figure 4.1

Microstructure of an AA6061 alloy reinforced with 20 vol.% Al_2O_3 particles

Table 4.2

Chemical composition of AA6061 in Duralcan MMC in weight percentage

| Mg | Si | Fe | Cu | Cr | Mn | Ti | Zn | Pb | Ni | Al |
|------|------|------|------|------|-------|------|-------|-------|-------|------|
| 1.11 | 0.45 | 0.05 | 0.23 | 0.09 | 0.001 | 0.01 | 0.003 | 0.008 | 0.006 | rest |

Table 4.3

Literature values for mechanical properties of AA6061 [74] and AA6061 with 20 vol.% Al_2O_3 particles (Duralcan MMC) [75]

| Mechanical property | AA6061 | MMC |
|--|----------|----------|
| ultimate tensile strength (σ_{uts}) | 310 MPa | 372 MPa |
| yield strength (σ_{ys}) | 276 MPa | 352 MPa |
| elongation (ϵ) | 0.12* | 0.04** |
| elastic modulus (E) | 68.9 GPa | 97.2 GPa |

* elongation at ultimate tensile strength

** elongation at fracture

4.2.2 Experimental Material

Four different series of MMC material have been produced in the laboratory by means of powder metallurgy. The volume fractions reinforcing ceramic particles for the various series were 7, 10, 14 and 22 vol.%. Production of the samples chronologically consisted of powder mixing, powder cold compaction and powder hot compaction/sintering. A full description of the optimisation of the production process resulting in fully dense material with well adhering Al_2O_3 particles is given elsewhere [76]. In this chapter, the essentials of the optimised process are presented.

The available aluminium and ceramic powders in this research were AA6061 $\leq 45 \mu m$, produced by Alpoco; The Aluminium Powder Co. Ltd., UK and $Al_2O_3 \leq 4 \mu m$ (Martoxid ®), produced by Martinswerk GmbH, Germany. As can be seen in figure 4.2, the unblended powders have irregular forms and show a large variation in size. Another important aspect is, that the morphology of the aluminium powder is very different from that of the Martoxid ® powder.

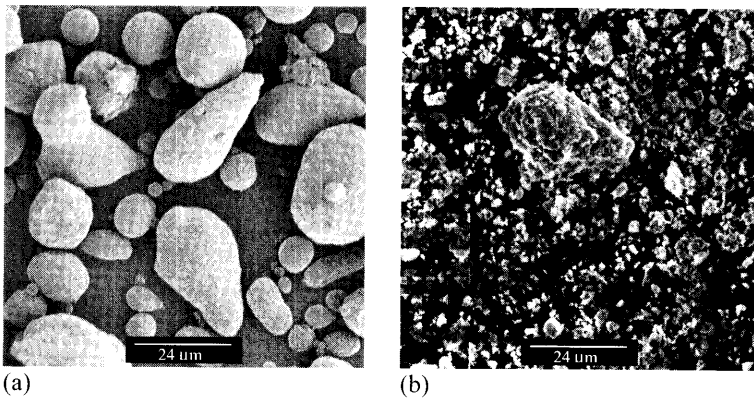


Figure 4.2

SEM-photographs of unblended (a) AA6061 $\leq 45 \mu m$ powder and (b) $Al_2O_3 \leq 4 \mu m$ Martoxid ® powder. The large lump visible in the centre of figure (b) is a conglomerate

Differences in particle sizes between AA6061 and Al_2O_3 powder might complicate the mixing step by the formation of conglomerates. If any conglomerates remain after mixing, they cannot be removed by further treatment and form defects in the material. To prevent this, the powders were blended in a Turbula 3D-mixer type T2C for at least 48 hours. This mixer is very effective, because of the multidirectional movement directions during mixing. In order to ensure breakdown of Al_2O_3 conglomerates, large solid Al_2O_3 balls were added prior to mixing.

The cold compaction step was included to create solid tablets which were easy to use in the hot compaction step. The size of the samples is determined in this step, so accurate dosage of powder was important to avoid extra manufacturing steps afterwards. For all samples, the pressure was increased slowly till 2040 bar and held constant for 30 seconds.

During the final compaction step, the actual bonding between the ceramic and aluminium takes place. To minimise the number of microstructural defects in the sample, hot compacting was performed under vacuum with a hot vacuum press, model Hot Press 50-60120 and this step consisted of drying, sintering and finally compacting. The process parameters used are summarised in table 4.4.

Table 4.4
Overview of the parameters used during hot compaction of the experimental MMCs

| Drying step | |
|-------------------|-----------------|
| time | 30 minutes |
| pressure | 0.5 bar |
| temperature | 450 °C |
| Sintering step | |
| time | 120 minutes |
| pressure | 204 bar |
| temperature | 615 °C |
| Cooling down step | |
| rate | natural cooling |
| pressure | 204 bar |

Figures 4.3 (a) and (b) show SEM photographs for 10 and 22 vol.% Al_2O_3 reinforced MMC. An inverse MMC structure was observed, whereby aluminium grains seemed to be embedded in an MMC network. However, since the network phase was fully wetted with aluminium, a good bonding was expected. It is clear from these figures, that the ratio of the particle sizes of the aluminium and the Al_2O_3 used does not result in a traditional discontinuously reinforced MMC. For such a structure, aluminium and Al_2O_3 powder with approximately the same average grain sizes would be needed, but this was not available at the time.

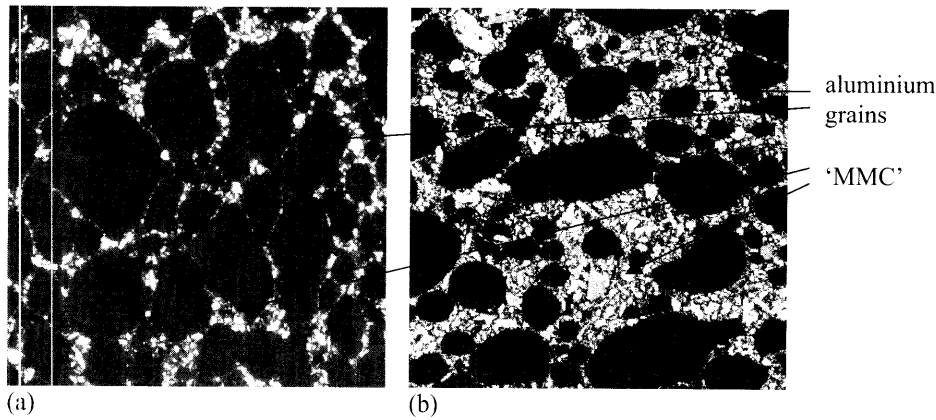


Figure 4.3

SEM photographs for (a) 10 vol.% and (b) 22 vol.% Al_2O_3 reinforced experimental MMC

4.3 Tensile Experiments

The MMCs turned out to be very hard to machine and too small in size to perform accurate tensile tests on it, so it was not possible to make tensile specimens from this material. To investigate the influence of the various heat treatments as described in chapter 2 on mechanical properties, tensile tests were performed on AA6061. The tested conditions were: the as-received T651 condition, a self-made T6 condition and conditions B and C. The T6 heat treatment consisted of 2 hours solutionizing at 530°C followed by water quenching and ageing for 8 hours at 175°C. Conditions B and C were prepared according to DSC measurements as described in chapter 2, figure 2.2. The specimens were heated with a heating rate of 5°C/min and water quenched at 256°C and 309°C respectively.

Since K_{Ic} tests were performed on specimens whereby loading was perpendicular to the extrusion direction, tensile specimens were taken from the extruded AA6061 bar in the same direction. Therefore, the specimen geometry used was a proportionally reduced round tension test specimen as described in ASTM E8M [77] and shown in figure 4.4.

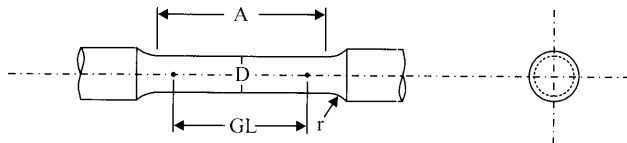


Figure 4.4

Specimen geometry used for tensile testing; $A = 36$ mm, $D = 6$ mm, $GL = 25$ mm and $r = 6$ mm

The specimens were provided with threaded ends to connect them to extension pieces, which could be fixed in the wedge grips of the tensile testing machine. For all tests, an Instron 4505 testing machine with a 100 kN loadcell was used, whereby the data was recorded by a computer using 'Series IX Automated Materials Testing System 5.04' software. To measure the displacement, an Instron clip gauge of $25 \text{ mm} \pm 5 \text{ mm}$, was used.

4.4 Fracture Mechanical Parameters

4.4.1 Stress Intensity Factor K

In fracture mechanics, the stress intensity factor K describes the magnitude of the elastic crack tip stress field. Provided that this stress field stays predominantly elastic, K characterises the crack growth and fracture behaviour of materials. This characterising ability makes the stress intensity factor an extremely important fracture mechanics parameter. The crack flank displacements caused by the load can be in opening mode (mode I), sliding mode (mode II) or tearing mode (mode III) or a combination of these modes, see figure 4.5.

Under conditions of limited crack tip plasticity, the parameter governing mode I fracture can be stated as a critical stress intensity, either K_{Ic} (plane stress) or K_{Ic} (plane strain) [78]. K_{Ic} can be considered a material property characterising the crack growth resistance, and is called the plane strain fracture toughness. By testing specimens of the same material with different geometries and with critical combinations of crack size and shape and fracture stress, the same value of K_{Ic} should be found.

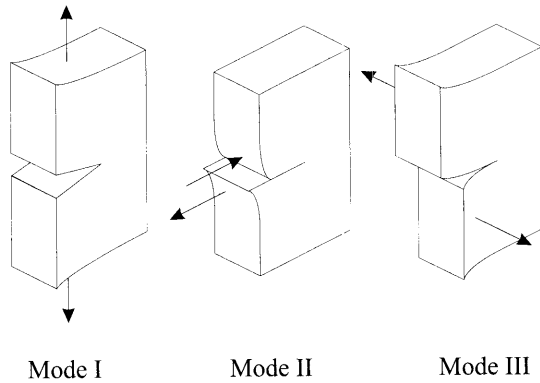


Figure 4.5
Three modes of loading [79]

The general form of the stress intensity factor is given by [78]:

$$K = \sigma \sqrt{\pi a} \cdot f\left(\frac{a}{W}\right) \quad (4.1)$$

where σ is the applied stress, a is the crack length and $f(a/W)$ is a geometry factor depending on the geometries of specimen and crack.

4.4.2 J-Integral Concept

If a material is too ductile to permit description of its behaviour by linear elastic fracture mechanics (LEFM), because the crack tip plastic zone is too large, other methods have to be used. One of the approaches (in the category of elastic-plastic fracture mechanics (EPFM)) used nowadays is a parameter called the J-integral introduced by Rice [80]. He showed that this line-integral can be used as a parameter for two-dimensional crack problems in the presence of plastic deformation. This line-integral with a value equal to the decrease in potential energy per increment of crack extension in linear or non-linear elastic material is called the J-integral and is defined by:

$$J = -\frac{dU_p}{da} = \int_{\Gamma} \left(W_{\text{strain}} dy - \underline{T} \frac{\delta \underline{u}}{\delta x} ds \right) \quad (4.2)$$

where U_p is the potential energy, Γ is the integration path counter-clockwise around the crack tip starting on one flank and ending on the other, W_{strain} is the strain energy per unit volume due to loading, x and y are rectangular co-ordinates in and normal to the crack direction respectively, \underline{T} is the outward traction vector on the integration path, \underline{u} is the displacement vector and ds is an increment of the contour path. Although the formal theoretical basis is limited to non-linear elastic material behaviour, there is consensus on its applicability for characterising crack growth initiation also in cases where this is preceded by considerable amounts of plastic deformation [81]. An important reason for this extended validity is, that under certain restrictions this non-linear elastic behaviour can be used to model plastic behaviour of a material. This is known as the deformation theory of plasticity [78]. The main restriction is that no unloading may occur in any part of a body since for actual plastic behaviour the plastic part of the deformation is irreversible. In principle, J is applicable only up to the beginning of crack extension and not for crack growth since the material at the crack tip is unloaded when crack growth occurs. However, under additional restrictions J can be used to characterise a limited amount of crack growth.

Rice has shown that the J-integral is path-independent. Because of this path independence, the contour can be chosen just as small as the crack tip area and so J can be considered a good measure for the situation at a crack tip.

J can be regarded both as an energy parameter comparable to the linear elastic energy release rate G , *i.e.* the available energy per unit new crack area (Irwin [82]) and as a stress intensity parameter comparable to K . The relation between the elastic-plastic parameter J and the elastic parameters G and K in case of limited plasticity then becomes:

$$J = G = \frac{K^2}{E'} \quad (4.3)$$

where $E' = E$ for plane stress and $E' = E/(1-\nu^2)$ for plane strain and ν is Poisson's ratio.

Rice showed that it is possible to determine J_{Ic} from a single test of certain types of specimen. As an example, J for a deeply cracked bar was derived as:

$$J = \frac{\eta}{Bb} \int_0^{V_{II}} P dV_{II} \quad (4.4)$$

where η is the work factor, B is the thickness of the specimen, b is the size of the uncracked ligament ahead of the crack, P is the load and V_{II} is the load-line displacement. To determine J , the load acting on a cracked specimen is measured as a function of the load-line displacement. J can then be determined for any displacement by calculating the area under the P - V_{II} curve up to that displacement.

4.5 Fracture Toughness Experiments

K_{Ic} tests were performed on AA6061 in as-received T651 condition and in conditions B and C. Commercial MMC was tested in as-received T6 condition and in conditions B and C, whereby the water quench temperatures were now 254°C and 300°C respectively. Experimental MMCs were all tested in T6 condition, *i.e.* 2 hours solutionizing at 530°C followed by water quenching and ageing for 8 hours at 175°C.

A 100 kN MTS servo-hydraulic fatigue testing machine was used for fatigue precracking the specimens. The control unit of this machine was an MTS 436.11 control unit providing centralised manual or automatic control of system electrical power, hydraulic pressure, program wave form and frequency. The K_{Ic} tests were performed on the same Instron testing machine as used for tensile testing.

To measure K_{Ic} values, a few standardised specimen geometries are available [83, 84], for which strict size regulations have to be met to ensure plane strain conditions at the crack tip. Since the Duralcan MMC as well as the AA6061 reference material were delivered as extruded rods with a diameter of 50.8 mm and 63.5 mm respectively, the disk-shaped compact tension specimen was selected for further use. Furthermore, specimens of such dimensions could also be produced using the powder metallurgy production facilities available to make the experimental MMCs. The specimen geometry and dimensions are shown in figure 4.6.

The specimens were all machined to a diameter of 50 mm, leading to a width of the specimen, W , of 37 mm. The specimens were then further machined using a high-pressure water jet with abrasives. The water pressure used was 3800 bar and the abrasive was HP-Barton Granat mesh#150, consisting mainly of SiO_2 , Al_2O_3 and Fe_2O_3 . A disadvantage of this technique is, that the water fans out through the thickness of the material, which could lead to some broadening of the notch on one of the sides.

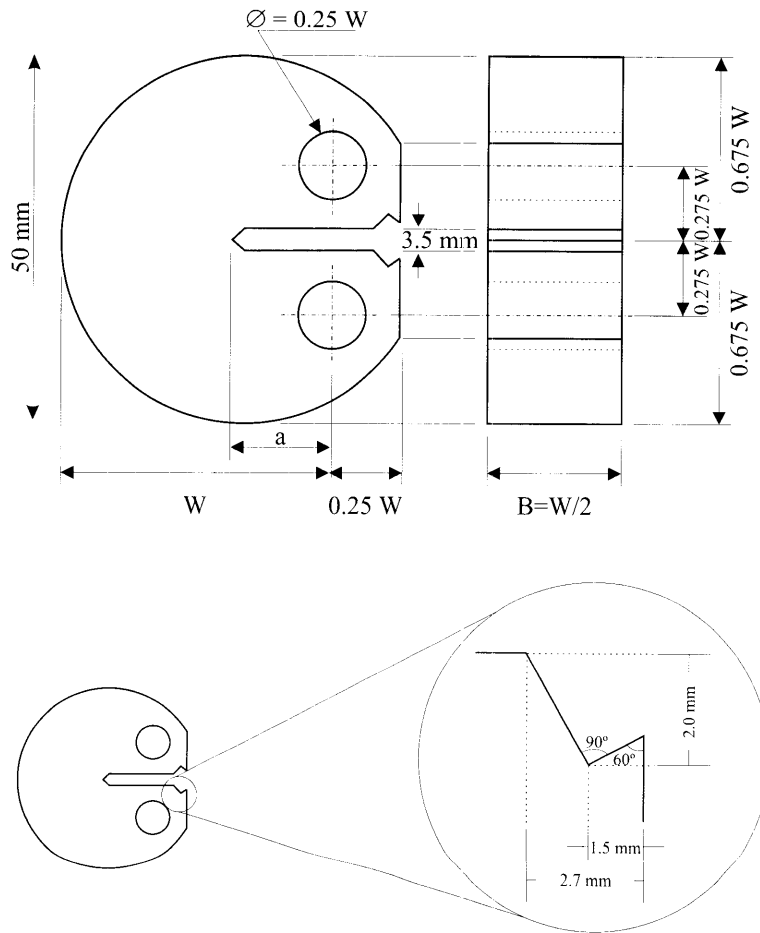


Figure 4.6
Disk-shaped compact tension specimen

4.5.1 Fatigue Precracking

For the stress intensity analysis as described in section 4.4.1 to be valid, an ideal planar crack with essentially zero tip radius needs to be created. The standard way to obtain such a crack is to fatigue load a specimen until a crack of the desired length has grown. To facilitate the initiation of a fatigue crack, a chevron starter notch produced via spark-erosion was used. The maximum stress intensity in the final stage of fatigue crack growth is not allowed to exceed 60% of the K_{Ic} value of the material. The total crack length of the crack starter configuration and the fatigue crack has to be between $0.45W$ and $0.55W$ and most of all, the crack should be straight. Since fatigue precracking must be conducted in the same material condition the K_{Ic} test is done, the specimens were heat treated before fatigue precracking.

During fatigue precracking it is important to be able to follow the growing crack until its length is between 0.45W and 0.55W. In MMC material the growing crack turned out to be invisible, due to unavoidable surface roughness. Therefore, the crack length was measured using the compliance method. If a crack grows, the compliance of the specimen will increase, *i.e.* the CMOD (crack mouth opening displacement) becomes larger under the same applied load. With a clip gauge (made in the laboratory and connected to an Hellige Mess- und Registriertechnik extensometer type 19), it was possible to measure the CMOD during fatigue precracking at $0.5P_{\max}$ and P_{\max} from which the compliance, C , could be calculated:

$$C = \frac{\Delta \text{CMOD}}{\Delta P} = \frac{\text{CMOD}_{P_{\max}} - \text{CMOD}_{0.5P_{\max}}}{P_{\max} - 0.5P_{\max}} \quad (4.5)$$

where P_{\max} is the maximum load during a fatigue cycle.

For the case where the CMOD is measured at the front face of a specimen, Jablonski *et al.* [85] fitted a polynomial function for a disk-shaped compact tension specimen:

$$\begin{aligned} \ln \left[\frac{E' V_x B}{P} \right] &= \ln[E'CB] = \\ &= 2.456 - 0.483 \left(\frac{a}{W} \right) + 13.996 \left(\frac{a}{W} \right)^2 - 18.708 \left(\frac{a}{W} \right)^3 + 8.493 \left(\frac{a}{W} \right)^4 + 3.571 \left(\frac{a}{W} \right)^5 \end{aligned} \quad (4.6)$$

where V_x is the CMOD, B is the specimen thickness and P is the applied load. With this method the crack length could be calculated and it was not necessary to detect crack growth visually.

Lack of crack front straightness was one of the biggest problems encountered during testing of AA6061-based materials, since these ductile alloys turned out to exhibit very strong crack tunnelling possibly due to the presence of residual stresses. In order to obtain reasonably straight, or at least symmetrical crack fronts during precracking, the residual stresses must be either redistributed or reduced uniformly. A fatigue precracking technique used to promote acceptable crack front shapes is the stepwise high R-ratio technique [86]. In the first stage of the precracking procedure, a lower R-ratio was used to initiate and grow the crack and during the final stage, the R-ratio was increased to straighten the crack front and propagate the fatigue crack to the desired length.

4.5.2 Fracture Toughness Test Methods Used

The American Society for Testing Materials (ASTM) published a multitude of standards for fracture toughness testing. Those standards thought to be applicable to MMCs are described here.

ASTM E399: Plane-Strain Fracture Toughness of Metallic Materials

The ASTM E399 standard provides regulations to obtain plane strain fracture toughness values for metallic materials and is especially suitable when the material to be tested is available in disc or rod shaped form [83].

After precracking, the specimens are loaded to fracture, while load and displacement (CMOD) are recorded. To prevent non-linearity at the beginning of a load-CMOD record, the specimens are preliminary loaded and unloaded with the maximum load not producing a stress intensity level exceeding that used in the final stage of fatigue cracking. The rate of the stress intensity factor increase during the K_{Ic} test must be within 0.55 and $2.75 \text{ MPa}\sqrt{\text{ms}}^{-1}$. From these records, of which three types are shown in figure 4.7, P_Q (the load value used to calculate a conditional stress intensity factor, K_Q) can be determined.

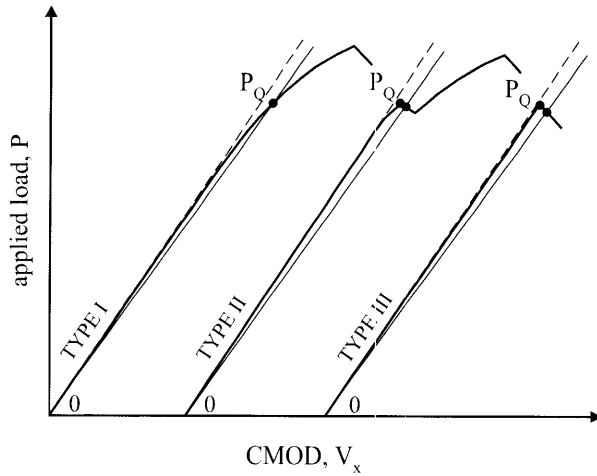


Figure 4.7
Determination of P_Q from three types of load-CMOD records [83]

To determine P_Q , a secant line with a slope 95% of that of the linear part of the load-CMOD record is drawn. This 95% secant corresponds with a crack growth of 2% of the initial crack length. This 2% crack growth more or less accounts for the effects of plasticity and stable crack growth [83]. The point at which this secant line intersects the load-CMOD record is called P_Q . If this intersection is preceded by a maximum than that maximum is defined as P_Q . The conditional critical stress intensity factor, K_Q , can now be calculated using equation (4.7):

$$K_Q = \frac{P_Q}{B\sqrt{W}} \cdot f\left(\frac{a}{W}\right) \quad (4.7)$$

For the disk-shaped compact tension specimen used, the geometry factor is given by:

$$f\left(\frac{a}{W}\right) = \frac{\left(2 + \frac{a}{W}\right) \cdot \left(0.76 + 4.8\left(\frac{a}{W}\right) - 11.58\left(\frac{a}{W}\right)^2 + 11.43\left(\frac{a}{W}\right)^3 - 4.08\left(\frac{a}{W}\right)^4\right)}{\left(1 - \frac{a}{W}\right)^{\frac{3}{2}}} \quad (4.8)$$

After fracture, the crack length has to be measured at three positions, namely at the centre of the crack front and midway between the centre of the crack front and the end of the crack

front on each surface of the specimen. The average of these three measurements is used to calculate K_Q .

For a K_Q value to be a valid K_{Ic} value according to this testing method, several requirements must be satisfied [83]:

1. For all specimen configurations, the specimen thickness and the crack length should exceed $2.5(K_Q/\sigma_{ys})^2$ to ensure a plane strain condition and an overall elastic specimen behaviour.
2. The ratio of P_{max}/P_Q is not allowed to exceed 1.10, because this could indicate the occurrence of too much plasticity and/or too much stable crack growth.
3. The difference between average and measured crack length should not exceed 10%.
4. For a chevron starter notch, the fatigue crack shall emerge from the chevron on both surfaces of the specimen, neither surface crack length shall differ from the average length by more than 10% and the difference between these two surface measurements shall not exceed 10% of the average crack length.

If and only if all these requirements are met, the calculated K_Q value is a valid K_{Ic} value for the material. In many publications, not all requirements are met, but the K_Q values are regarded as a good indication of K_{Ic} [87-89]. Reported reasons for invalidity of fracture toughness tests of AA6061 are fatigue crack front curvature and too large P_{max}/P_Q ratios [88, 89]. In MMCs, fatigue crack front curvature, non-linearity of the load-CMOD record and out of plane crack propagation can cause invalidity [90]. Considering non-linearity it is difficult to check for validity, since the standard is not specific in this. In fact, for AA6061 it is difficult to find completely valid K_{Ic} data in literature. Furthermore, in the literature little attention is paid to the set of requirements to produce reliable K_{Ic} data for MMCs [91-93].

ASTM E1737: J-Integral Characterisation of Fracture Toughness

ASTM E1737 [84] covers the determination of fracture toughness as characterised by the J-integral for ductile materials that lack sufficient size and thickness or that are too ductile to be tested for K_{Ic} in accordance with the requirements of ASTM E399 [83].

J_{Ic} can be determined from a J- Δa curve, whereby a load-CMOD record as shown in figure 4.8 is analysed. The area under the curve corresponding to small crack extensions Δa is used to calculate J with equation (4.4) and the crack length can be calculated from specimen compliance through interruptions of the standard static test with unloadings using equation (4.6). According to the standard, the crack length should be calculated from unloading compliance values measured at the load-line, but since the clip gauge was placed at the front face this was not possible.

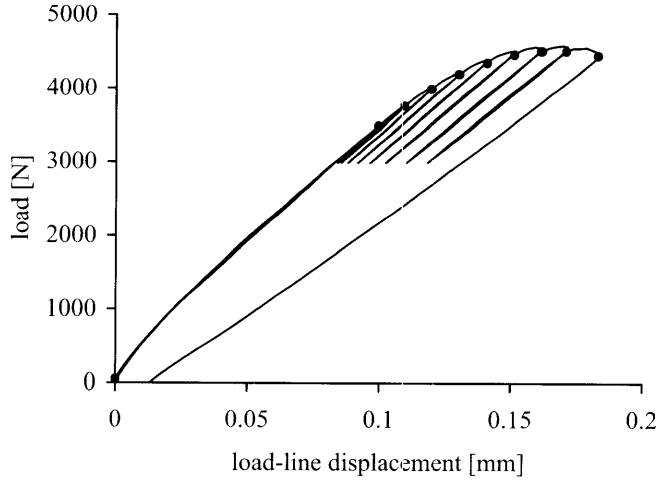


Figure 4.8

Example of a load versus load-line displacement record used for determination of the J-integral using the unloading compliance method

The initial crack length is thus defined as the crack length measurement from the first unloading in order to determine the amount of crack growth. Since the elastic modulus of the MMCs is unknown, an estimate of the modulus has to be made for crack length calculation. This value is estimated by fitting the initial crack length calculated from the unloading compliance to the actual initial crack length as measured from the fracture surface. For the calculation of J, both the load-line displacement and J need to be separated in an elastic and plastic component according to equations (4.9) and (4.10):

$$\begin{cases} V_{ll} = V_{ll,el} + V_{ll,pl} \\ V_{ll,pl} = V_{ll} - PC_{ll} \end{cases} \quad (4.9)$$

$$J = J_{el} + J_{pl} \quad (4.10)$$

The elastic component of J is formed by the stress intensity at load displacement point (i) and is determined by the crack length and applied load only:

$$J_{el} = \frac{K^2(1-\nu^2)}{E} \quad (4.11)$$

where K is the stress intensity factor in point (i) and is given in equation (4.7), where the geometry factor $f(a/W)$ is given by equation (4.8).

The plastic component of J is given by:

$$\begin{cases} J_{pl(i)} = \left[J_{pl(i-1)} + \left(\frac{\eta_{(i-1)}}{b_{(i-1)}} \right) \frac{A_{pl(i)} - A_{pl(i-1)}}{B_N} \right] \left[1 - \gamma_{(i-1)} \frac{a_{(i)} - a_{(i-1)}}{b_{(i-1)}} \right] \\ \eta_{(i)} = 2.0 + 0.522 \frac{b_{(i)}}{W} \\ \gamma_{(i)} = 1.0 + 0.76 \frac{b_{(i)}}{W} \end{cases} \quad (4.12)$$

where $A_{pl(i)}$ is the increment of area under the load versus plastic load-line displacement record, B_N is the net thickness and η is the plastic work factor.

To determine the total energy absorbed by the specimen, measurements of applied load and load-line displacement are needed. Therefore, the clip gauge has to be positioned in the load-line. Since this was not the case for the specimens used, the recorded displacements should be corrected [94]. This correction is based on the principle that pin loading a compact tension specimen is in fact a bending test, whereby the plastic component of the rotation point, r_p , for a compact specimen is between 0.46 and 0.47 depending on the value of a/W [95]. When the plastic rotation factor is known, the plastic part of the load-line displacement, $V_{ll,pl}$, can be calculated as follows:

$$V_{ll,pl} = \frac{V_{x,pl}(a + r_p(W - a))}{a + r_p(W - a) + z} \quad (4.13)$$

where $V_{x,pl}$ is the plastic component of the CMOD and z is the distance between clip gauge knife edge measuring point and the load-line in the specimen.

Determination of the fracture toughness as characterised by the J-integral now consists of the following:

- plot the J- Δa data points,
- draw a so-called theoretical blunting line $J = 2((\sigma_{ys} + \sigma_{uts})/2)\Delta a$, this line accounts for the apparent increase in crack length owing to crack tip blunting,
- draw a 0.2 mm offset line parallel to the blunting line which represents 0.2 mm stable crack growth, this line is needed since the actual onset of crack extension is hard to determine and would lead to a lot of spread,
- draw 0.15 and 1.5 mm exclusion lines parallel to the blunting line which bound the region of acceptable J-values,
- draw a least square fit of the power law $J = C_1(\Delta a)^{C_2}$ through the acceptable J- Δa points (C_1 and C_2 are fit coefficients); this line is called the regression line
- designate the intersection of the regression line with the 0.2 mm offset line, this point is J_Q , and
- draw two vertical lines (the minimum and maximum apparent crack growth lines) through the intersections of the exclusion lines with the regression line and the line $b((\sigma_{ys} + \sigma_{uts})/2)/15$ and omit data points outside this exclusion zone.

Finally, the value of J_Q can be qualified valid and called J_{Ic} when the following requirements are met [84]:

1. The difference between average and measured crack length should not exceed 5%.
2. None of the crack extension measurements should differ more than 50% from the average crack extension, whereby the difference between average and measured crack extension should not exceed 5%.
3. The number of points in the data set used for determination of the power law coefficients should be larger than or equal to 5, whereby C_2 should not exceed 1.0.
4. The correlation of the least square fit of the power law should be greater than 0.96, whereby all data that fall outside the exclusion zone must be eliminated from the least square fit procedure.
5. The sample thickness and the length of the initial ligament should exceed $25J_Q/\sigma_{ys}$.
6. The slope of the power law regression line, dJ/da , evaluated at Δa_Q should be less than $(\sigma_{ys} + \sigma_{uts})/2$.

4.6 Tensile Test Results

From the engineering stress-strain curves, see figure 4.9, the elastic modulus, the ultimate tensile strength, the yield strength and the elongation at ultimate tensile strength were determined, for which the obtained values are given in table 4.5. The hardening exponent is defined in a uniaxial stress-strain relation in the form of a piece-wise power law. It turned out to be more accurate to calculate the hardening exponent from the true stress-strain curves at the moment of necking as $1/(\text{true strain at } P_{\max})$, whereby the true stress-strain curves were determined by plotting $\ln(\epsilon+1)$ versus $\sigma(\epsilon+1)$.

$$\epsilon = \begin{cases} \frac{\sigma}{E} & \text{if } \epsilon \leq \frac{\sigma_{ys}}{E} \\ \frac{\sigma_{ys}}{E} \left(\frac{\sigma}{\sigma_{ys}} \right)^n & \text{if } \epsilon > \frac{\sigma_{ys}}{E} \end{cases} \quad (4.14)$$

Differences found when comparing the obtained results with data found in literature (table 4.3) are mostly a result of the heat treatment condition the specimens were in, but also because of the fact that tensile tests were performed on specimens with a transverse orientation to the loading direction, whereas reported values are for specimens with a longitudinal orientation.

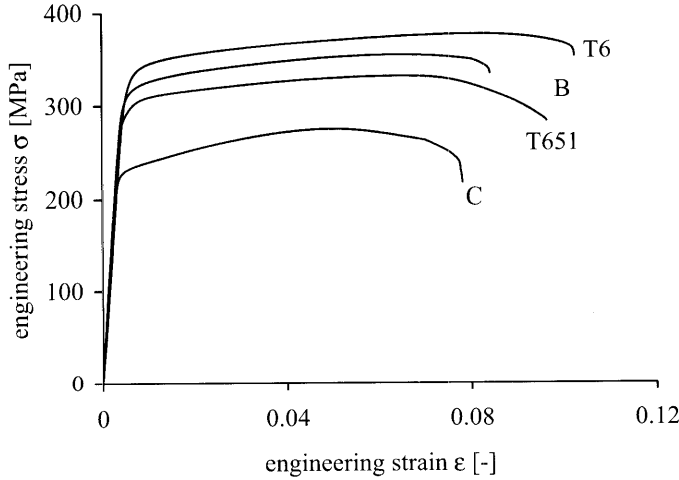


Figure 4.9
Engineering stress-strain curves for AA6061-T651, -T6, -B and -C

Table 4.5
Mechanical properties determined in tensile experiments averaged over two tests, for all tests $E = 70$ GPa

| Material | σ_{uts} [MPa] | σ_{ys} [MPa] | ϵ_{uts} [-] | n [-] |
|-------------|-----------------------------|----------------------------|-----------------------------|---------|
| AA6061-T651 | 282 | 295 | 0.10 | 15.8 |
| AA6061-T6 | 351 | 340 | 0.10 | 12.4 |
| AA6061-B | 334 | 328 | 0.08 | 15.6 |
| AA6061-C | 230 | 200 | 0.08 | 7.9 |

4.7 Fracture Toughness Test Results and Discussion

4.7.1 AA6061 Aluminium Alloy

For both the reference aluminium alloy and the Duralcan MMC various heat treatments were applied to investigate a possible influence on the fracture toughness. To put the MMC results in correct perspective, the AA6061 data are discussed first. Calculated fracture toughness values using the ASTM E399 standard [83] for the AA6061 reference alloy in the three heat treatments considered are given in table 4.6. The K_Q values found are considerably higher than the average value found in literature, *i.e.* 27 MPa $\sqrt{\text{m}}$ for T651 condition [87-89]. However, critical comparison of all fracture morphology and geometry parameters with the validity criteria for this test indicated that in all experiments at least one criterion was violated and the K_Q value may not be classified as a K_{Ic} value. The reasons for invalidity were mostly

4. Fracture Mechanical Experiments

due to too short fatigue precracking, fatigue crack front obliqueness and tunnelling, too high P_{\max}/P_Q ratios and all specimens were, in retrospect, too thin.

Table 4.6
The crack length, P_Q , K_Q and reasons for K_Q invalidity for AA6061

| Specimen | a [mm] | P_Q [kN] | K_Q [MPa \sqrt{m}] | Reasons for invalidity |
|----------|--------|------------|-------------------------|--|
| T651 (1) | 16.61 | 17.5 | 40.7 | crack too short $a, B < 2.5(K_Q/\sigma_{ys})^2$ |
| T651 (2) | 16.27 | 18.7 | 42.2 | crack too short $a, B < 2.5(K_Q/\sigma_{ys})^2$ |
| B (1) | 17.03 | 19.8 | 47.6 | $P_{\max}/P_Q > 1.10$ crack too short, oblique and tunnelled $a, B < 2.5(K_Q/\sigma_{ys})^2$ |
| B (2) | 16.74 | 18.8 | 44.0 | $P_{\max}/P_Q > 1.10$ crack too short, oblique and tunnelled $a, B < 2.5(K_Q/\sigma_{ys})^2$ |
| C (1) | 16.72 | 11.6 | 27.2 | $P_{\max}/P_Q > 1.10$ crack tunnelled $a, B < 2.5(K_Q/\sigma_{ys})^2$ |

For tough aluminium alloys Kaufman [96] suggested that the requirements for crack length and specimen thickness should be altered to $a, B > 5(K_Q/\sigma_{ys})^2$, to ensure that the specimen thickness is about 50 times the plane strain plastic zone size. In this investigation the plastic zone size in the AA6061 specimens is probably too large with regard to the thickness, leading to mixed plane strain/plane stress conditions. Increasing the thickness will thus reduce plastic yielding and therefore possibly overcome problems with load-CMOD records as were found for several specimens, see for instance figure 4.10, and a pure plane strain condition would result in less stable crack growth and thus lower P_{\max}/P_Q ratios.

Considering problems with too oblique and tunnelled fatigue crack fronts, Petrak [97] found that fatigue crack front obliqueness had no significant influence on measured K_Q values in AA2024. To this aim, he performed tests on bend specimens, violating the requirements of fatigue crack front obliqueness on purpose. The fatigue precrack intersected both surfaces of the specimens but was too oblique.

In the current investigation, the fatigue precrack in specimens in B and T651 condition was oblique in a way that the crack only started on one surface and did not reach the other surface. The fatigue crack started randomly on one of the specimen sides, so obliqueness was not due to eccentricity of the grips. As the fatigue crack tip is much sharper than the starter notch, the obliqueness in this case will probably influence the K_Q value. That is why the K_Q values of the specimens in these conditions are an overestimation of the real K_{Ic} in T651 condition. In specimens in the C condition the crack front did “touch” the other surface and the influence of the crack front obliqueness on the measured K_Q is negligible. However, in the C condition, extensive tunnelling would lead to invalid K_Q values even if crack front obliqueness could be ignored.

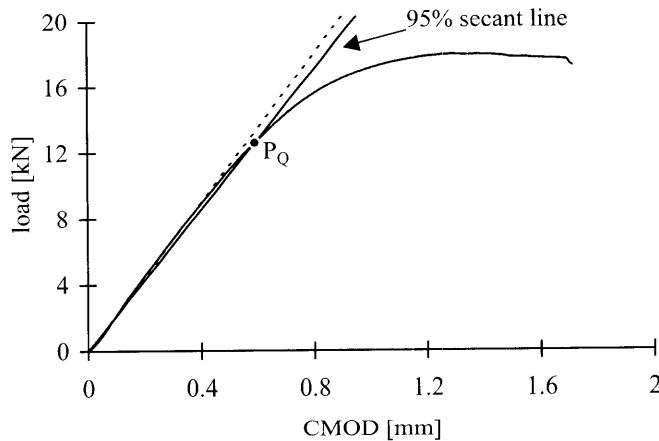


Figure 4.10

Load-CMOD record for AA6061 specimen C (1) which leads to $P_{max}/P_Q > 1.10$ and thus a K_Q value instead of a K_{Ic} value

Tunnelling, which was most severe in the C condition, is probably due to internal residual stresses [90]. To obtain the C condition the specimens were water quenched from 309°C to room temperature. The T651 and B condition specimens were water quenched from 175 and 256 °C respectively. Since the temperature difference before and after quenching is highest in the C condition and the yield stress in this condition is the lowest (200 MPa), internal residual stresses after quenching will be largest in the C condition. This results in tensile stresses in the centre and compressive stresses at the surface of a specimen leading to higher crack growth rates in the centre. This could indicate that tunnelling is indeed due to internal residual stresses. Extensive crack tunnelling can lead to plane stress conditions instead of plane strain conditions, especially near the outer surface of the specimen. Overestimation of the K_{Ic} is therefore probably largest in C condition.

In T651 condition, the unstable crack growth region of the fracture surfaces showed, except for the shearlip regions, little height variation. This flat region showed lines parallel to the crack growth direction. These lines were due to the fact that small fatigue cracks started at planes slightly different from the main crack plane and grew towards this plane. The fracture surfaces of the specimens in condition B were much rougher than those in T651 condition. In the unstable crack growth region only small shearlips were present and the fatigue crack growth region had a glistening appearance with a lot of ‘steps’ perpendicular to the crack growth direction. These steps are due to changes in orientation of the main crack plane during crack growth. In C condition more than 50% of the unstable crack growth region consisted of shearlips. There were also steps visible in the fatigue crack growth region but these steps were larger than in condition B. The steps can be explained as follows. In every grain there is a preferred crack plane which the crack follows until a grain boundary is reached, then it changes to the preferred plane in the next grain. The steps visible in the fatigue crack growth regions can be linked to the grain size in the direction perpendicular to the extrusion direction. In T651 condition the grains were very small (0.01 - 0.05 mm), but in conditions B and C they were much larger leading to large steps in the fatigue crack growth region. The step sizes were 0.3 - 0.9 mm, whereas the measured grain sizes were 0.2 - 0.7 mm.

4. Fracture Mechanical Experiments

The fracture surfaces were also investigated with a scanning electron microscope (SEM). Figures 4.11 and 4.12 show specific features found for all three heat treatment conditions for the fatigue and unstable crack growth regions respectively. The fatigue crack growth region did not show any dimples, whereas the unstable crack growth region revealed larger and smaller dimples. Regarding the three different heat treatments, the average dimple sizes became larger going from T651 to B to C condition.

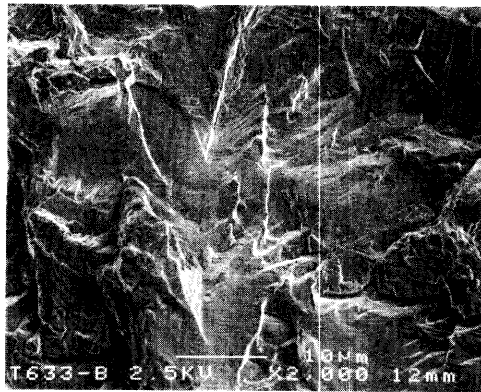


Figure 4.11

Fatigue crack growth region of AA6061 in T651 condition, crack growth direction is from bottom to top

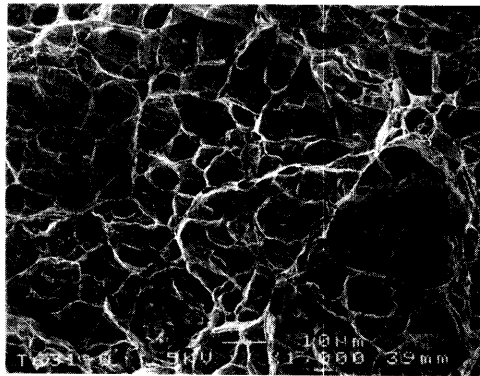


Figure 4.12

Unstable crack growth region of AA6061 in T651 condition, crack growth direction is from bottom to top

4.7.2 Commercial MMC

The effects of the three different thermal treatments on the K_Q values for the Duralcan MMC are presented in table 4.7. K_Q values range from 16.0 to 22.4 MPa√m. As in table 4.6, in table 4.7 also violations of requirements for the test to be a valid K_{Ic} test are reported. Unlike measurements on AA6061, one measurement met all requirements and the K_Q value can be classified as a valid K_{Ic} value. The other values were invalid, mostly due to fatigue crack front obliqueness and tunnelling. In T6 condition the ratio P_{max}/P_Q was higher than 1.10, which is visible in the load-CMOD record, see figure 4.13 and thus results in an underestimation of the fracture toughness. In the MMC, tunnelling of the fatigue crack front was also most severe in the C condition, as it was for AA6061. As mentioned before, Roebuck and Lord stated that tunnelling is due to internal stresses, but they also reasoned that tunnelling would be more severe in MMCs than in matrix alloy. Since thermal diffusivity of MMCs is lower and the stiffness at elevated temperatures is higher than those of the same matrix alloy, this would lead to higher internal stresses after quenching [90]. However, in this investigation tunnelling was more severe in the unreinforced AA6061 than in the MMC, which can be explained by the fact that in spite of the two factors mentioned before, the yield strength of the MMC is higher compared to AA6061.

Although there was only one K_{Ic} value, the other K_Q values in conditions B and C probably give a good indication of the K_{Ic} , as they only just failed to meet the crack front requirements. Therefore, the K_{Ic} of the MMC is likely to be around 21 MPa√m both in B and C condition.

Table 4.7

The crack length, P_Q , K_Q and reasons for K_Q invalidity for Duralcan MMC

| Specimen | a [mm] | P_Q [kN] | K_Q [MPa√m] | Reasons for invalidity |
|----------|--------|------------|---------------|------------------------|
| T6 (1) | 18.24 | 5.9 | 16.2 | $P_{max}/P_Q > 1.10$ |
| T6 (2) | 15.11 | 7.0 | 16.0 | $P_{max}/P_Q > 1.10$ |
| B (1) | 17.23 | 8.1 | 20.6 | crack oblique |
| B (2) | 17.67 | 7.6 | 20.2 | crack oblique |
| C (1) | 18.96 | 7.2 | 22.4 | crack tunnelled |
| C (2) | 18.84 | 6.9 | 20.9 | crack tunnelled |
| C (3) | 18.43 | 7.4 | 21.4 | VALID |

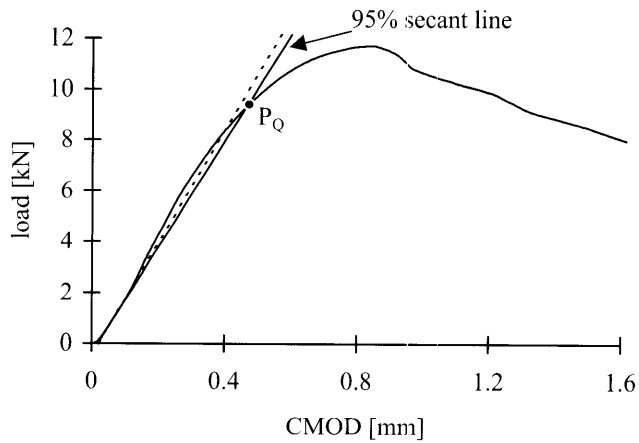


Figure 4.13

Load-CMOD record for Duralcan MMC specimen T6 (2) which leads to $P_{max}/P_Q > 1.10$ and thus a K_Q instead of a K_{Ic} value

Like for the AA6061 material, fractographic investigation with SEM revealed the same distinct differences between the fatigue and unstable crack growth regions for all three heat treatment conditions. The structures in the fatigue crack growth region were coarse, showing only a few particles in spite of the presence of 20 vol.% Al_2O_3 particles. However, the unstable crack growth regions showed a lot of particles surrounded by dimples. Figures 4.14 and 4.15 show representative fracture surfaces of both crack growth regions in C condition. The fracture surfaces of the specimens in the other conditions were alike, but the amount of particles visible on the fracture surface on the SEM photos was different, see table 4.8. As a reference, the amount of particles per same unit area (0.16 mm^2) in an arbitrary cross-section of an MMC sample is also noted in this table.

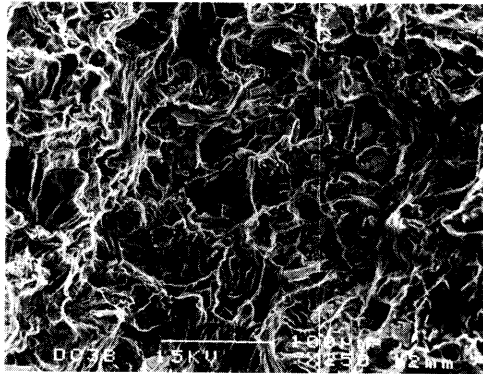


Figure 4.14

Fatigue crack growth region of Duralcan MMC in C condition, crack growth direction is from bottom to top

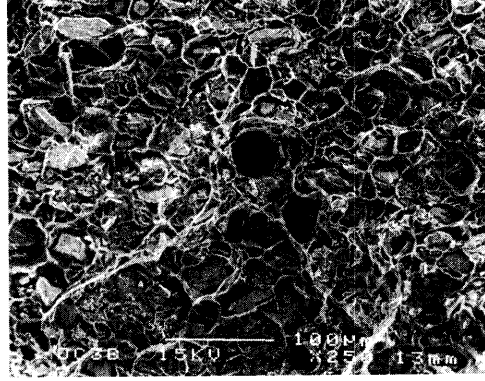


Figure 4.15

Unstable crack growth region of Duralcan MMC in C condition, crack growth direction is from bottom to top

Condition T6 showed the least number of particles in the fatigue crack growth region, indicating that the growing crack avoided the particles and the particle/matrix interface. The crack grew through the matrix material, thereby creating a very rough fracture surface. Conditions B and C on the other hand showed more particles, indicating that the crack went through the matrix as well as the particle/matrix interface.

For all three conditions, a lot of particles were seen in the unstable crack growth region. Regarding the various conditions tested, the least number of particles were counted for the T6 condition, which has the highest matrix yield strength and most particles were counted for the C condition, which has the lowest matrix yield strength. Assuming an average K_{Ic} value for the Duralcan MMC of 21 MPa \sqrt{m} and using the yield strength values from table 4.5, the plane strain plastic zone size at the crack tip can be calculated using the following equation [78]:

$$2r_p \approx \frac{1}{3\pi} \left(\frac{K}{\sigma_{ys}} \right)^2 \quad (4.15)$$

This results in a plastic zone size for the T6 condition which is approximately 3 times smaller than that for the C condition. This small plastic zone size combined with the fact that the constraining effect of the stiff particles acts to deflect a growing crack somewhat [5], causes the crack to meander through the matrix, *i.e.* few cracked particles are observed. In the C condition, the plastic zone envelopes many particles and particle cracking may become more important. This means that many more particles lie within the highly stressed region, which increases the distance from the crack in which cracking occurs. It was not possible to detect unambiguously whether particles were broken or decohesion of the particle/matrix interface had occurred, but on the fracture surfaces no empty dimples were visible, which should indicate predominantly particle fracture.

Table 4.8

Average amount of particles per unit area for the fatigue and unstable crack growth regions of Duralcan MMC (CGR is crack growth region)

| Heat treatment | Fatigue CGR | Unstable CGR |
|---|-------------|--------------|
| T6 | 6 | 46 |
| B | 36 | 98 |
| C | 16 | 102 |
| Arbitrary cross-section MMC: 82 particles | | |

Using the model of Hahn and Rosenfield [98] the fracture toughness of an MMC can be predicted when the volume fraction, f , particle diameter, d , Young's modulus and yield stress are known:

$$K_{Ic} = f^{-\frac{1}{6}} \cdot \sqrt{2\sigma_{ys}E\left(\frac{\pi}{6}\right)^{\frac{1}{3}} d} \quad (4.16)$$

This model is based on the assumption that the crack opening displacement, δ ($=K^2/\sigma_{ys}E$), equals 0.5 times λ_v , where λ_v is the distance between microcracks in front of the crack tip and also that a microcrack is associated with every reinforcing particle. It will be clear that the model is valid over a restricted range of particle volume fractions, *i.e.* it fails in the limit $f = 0$, leading to infinitely large K_{Ic} values. On the other hand, it is also not fit for very high volume fractions either, where one would deal with an inverse structure consisting of soft regions in a hard matrix. Using the appropriate material data [75] the calculated K_{Ic} value becomes typically 43 MPa \sqrt{m} and minimal 41 MPa \sqrt{m} . This is much higher than the measured K_Q value. In this case it would be wrong to use the yield stress of AA6061 in equation (4.16) because a plastic zone size of approximately 0.5 mm in the MMC is thought to be large enough to encompass both matrix material and particles, so the yield stress and Young's modulus of the MMC are used [5]. The Hahn and Rosenfield model calculates the K_{Ic} of materials with particles homogeneously distributed throughout the material. The particle distribution is homogeneous in the investigated MMC but the amount of particles in the crack plane varies a lot. If the crack is deflected towards particles, the volume fraction is higher in the crack plane. For example if the volume fraction in the crack plane would be as high as 50 vol.%, the calculated K_{Ic} would drop to 37 MPa \sqrt{m} .

4.7.3 Experimental MMC

The type of data collection as shown in figure 4.8 can be used for the determination of J , but is also suitable to determine the fracture toughness according to ASTM E399 to investigate the influence of various volume percentages reinforcing particles in experimental MMCs on the fracture toughness. Since load-CMOD records including unloadings were not available for all specimens tested, plane strain fracture toughness values were calculated according to ASTM E399 [83] for all specimens and according to ASTM E1737 [84] if possible. An overview of measured fracture toughness values using both methods (K_J calculated with equation (4.3)) is listed in table 4.9 and graphically shown in figure 4.16. In both table 4.9 and

figure 4.16, the specimen test result which is qualified valid according to the specific test method regulations is represented as bold. For the determination of K_I none of the test results satisfied all the requirements imposed by the standard. Especially the conditions regarding crack front shape and calculation were invalid. A feature often observed in this investigation was, that the load-CMOD records showed a non-linear part in the beginning of the record. Since the standard states that initial non-linearity should be ignored, this part is neglected when calculating the initial slope, because not neglecting this part would lead to improbably low fracture toughness values.

Table 4.9

*Overview of measured fracture toughness values using the various methods;
valid test result is represented as bold*

| Specimen | K_Q | K_I |
|------------|--------------|-------|
| AA6061 (1) | 40.39 | - |
| AA6061 (2) | 41.22 | 58.86 |
| AA6061 (3) | 36.98 | 55.19 |
| AA6061 (4) | 40.75 | 57.81 |
| AA6061 (5) | 42.06 | - |
| MMC 7 (1) | 13.34 | 31.57 |
| MMC 7 (5) | 12.17 | 29.07 |
| MMC 10 (1) | 13.16 | - |
| MMC 10 (2) | 12.49 | 30.85 |
| MMC 10 (3) | 13.28 | 36.54 |
| MMC 14 (1) | 13.34 | - |
| MMC 14 (5) | 15.17 | - |
| MMC 14 (6) | 14.06 | - |
| MMC 22 (2) | 13.50 | - |
| MMC 22 (4) | 12.74 | 16.21 |
| MMC 22 (5) | 13.90 | 15.63 |
| MMC 22 (6) | 13.81 | - |
| MMC 22 (7) | 11.83 | - |

It can be seen, that determination of the fracture toughness with the ASTM E399 shows a drop in fracture toughness for low volume fractions, followed by a plateau where the fracture toughness is only slightly influenced by the volume fraction reinforcing Al_2O_3 particles. ASTM E1737 results in a gradual decrease in fracture toughness with increasing volume fractions Al_2O_3 particles. Results obtained using the characterisation of fracture toughness with the J-integral seem to be most in line with physical expectations.

To illustrate the effect the crack front shape has on the load-CMOD records, the fracture surfaces and records for three specimens containing 22 vol.% Al_2O_3 particles are included in figures 4.17 and 4.18. The average crack lengths of the specimens are comparable, *i.e.* respectively 18.46, 18.32 and 17.14 mm for specimens MMC 22 (2), (6) and (7). As shown in figure 4.17, the fatigue crack front shapes are very different, being straight but heavily

tunnelled for MMC 22 (2), oblique and tunnelled for MMC 22 (6) and straight and slightly tunnelled for MMC 22 (7). The main differences observed in figure 4.18 are that the peak load values shift to larger CMOD values and are higher for the specimens with invalid crack lengths (MMC 22 (2) and (6)). Furthermore, the slope of the initial part of the load-CMOD record is higher for MMC 22 (7) and remains constant during a larger interval, whereas the other two curves show non-linearities both at the beginning and at the end of the linear part, see figure 4.19. So, fatigue crack front curvature and/or obliqueness may very well cause this variation in initial slope of the load-CMOD records. Another plausible reason may be the occurrence of crack closure in case of oblique cracks which reveals itself as a non-linearity in the beginning of the K_{Ic} test. Unfortunately this phenomenon is hard to verify.

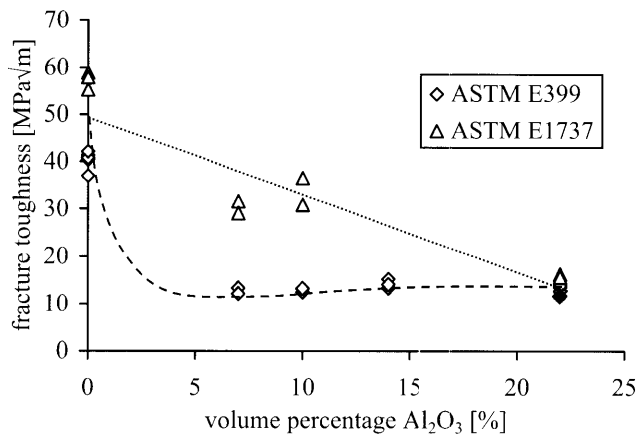


Figure 4.16
Measured fracture toughness values including all specimens and all test methods; valid test result is represented as bold

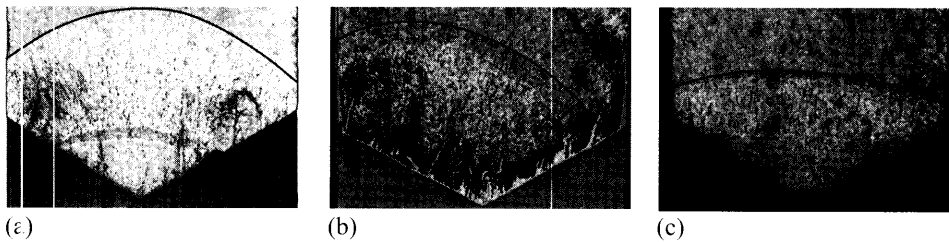


Figure 4.17
Fracture surfaces of (a) MMC 22 (2), (b) MMC 22 (6) and (c) MMC 22 (7); contrast was enhanced to visualise the fatigue precrack area

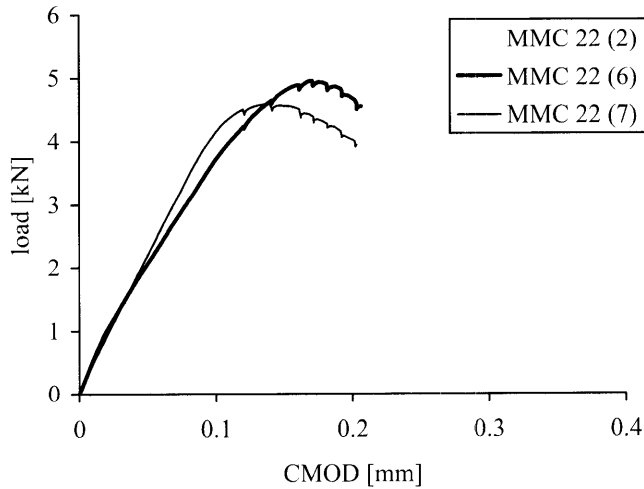


Figure 4.18
Load-CMOD records of MMCs 22 (2), (6) and (7)

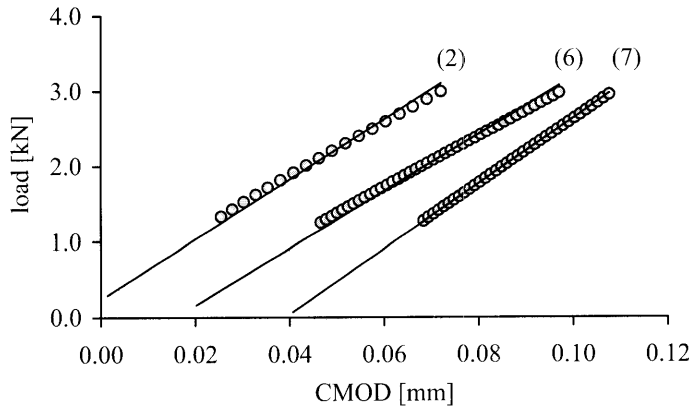


Figure 4.19
Detail of the initial part of the load-CMOD records of MMCs 22 (2), (6) and (7)

Irregularities in the linear part of the load-CMOD record have a pronounced effect on the fracture toughness as determined with ASTM E399. Although the regulations in the standard are rather strict, it can be concluded that this is rightly so since this is necessary for obtaining reliable fracture toughness values. When small irregularities are introduced by fatigue crack front curvature or obliqueness, the results may be called useless.

Besides problems with crack front geometries there is also the problem of too much plasticity and stable crack growth for various specimens. This is visualised for specimen MMC 7 (5) in figure 4.20, where the load-CMOD records of this specimen and MMC 22 (7) are compared.

4. Fracture Mechanical Experiments

These specimens have practically similar initial crack lengths and fracture toughness values, *i.e.* 17.45 compared to 17.14 mm and 12.17 compared to 11.83 MPa $\sqrt{\text{m}}$, however the load-CMOD records are entirely different. It can be concluded that MMC 7 (5) is not for nothing an invalid test result.

Summarised, the ASTM E399 method turned out to be inadequate for determination of the variation of fracture toughness versus volume percentage Al_2O_3 particles for the experimental MMCs.

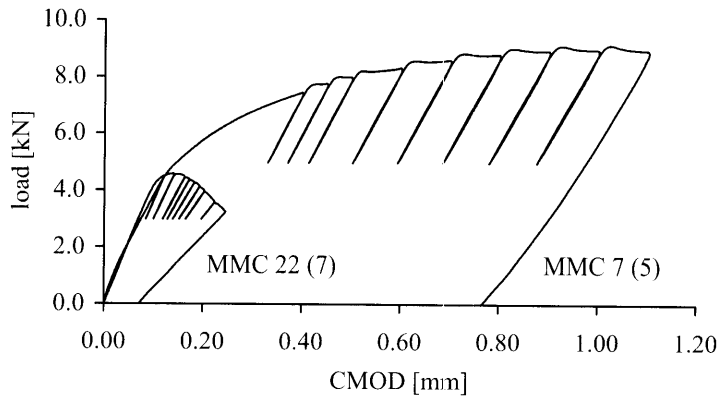


Figure 4.20

Comparison of load-CMOD records of MMC 7 (5) and MMC 22 (7)

A summary of all observations and results obtained leads to the following conclusion. For the ASTM E399 it turned out that irregularities in the initial part of the load-CMOD records for MMC specimens with low volume fractions Al_2O_3 particles resulted in unreliable, underestimated fracture toughness values. It is expected that fracture toughness values for specimens containing higher volume fractions and exhibiting less non-linearity are more reliable. Since the ASTM E399 method underestimates the fracture toughness of the experimental MMC material, it is reasonable to believe that the actual trend is predicted by ASTM E1737.

It can be concluded that the fracture toughness of an aluminium - MMC composite, where the aluminium is embedded in an MMC network, decreases linearly with an increase in volume fraction Al_2O_3 particles.

Assuming that the approximately linear relation between K_{Ic} and the volume fraction Al_2O_3 particles is correct, the results suggest that the K_{Ic} value of Al_2O_3 , *i.e.* $\approx 2.5 \text{ MPa}\sqrt{\text{m}}$ [99], is already obtained at a volume percentage of $\approx 30\%$. This very low volume percentage may be related to the inverse structure, *i.e.* MMC layers with a very high percentage Al_2O_3 particles around aluminium grains instead of an aluminium matrix surrounding Al_2O_3 particles, created in these materials, see figure 4.3. At approximately 30% the microstructure becomes such that each aluminium grain is fully surrounded by a layer of MMC, leading to fracture proceeding through this brittle MMC layer and thus a fracture toughness value of Al_2O_3 is not unrealistic. Furthermore, it should be mentioned that specimens containing 30% Al_2O_3 were produced successfully, but they fractured during precracking, indicative of a low K_{Ic} value.

Like for the commercial MMCs, the fracture surfaces of the experimental MMCs were investigated with a SEM, whereby special attention was paid to the fatigue crack growth regions compared to the stable crack growth regions. Figure 4.21 shows the fatigue crack growth region for specimens containing 10 and 22 vol.% Al_2O_3 particles respectively. For all specimens, the fatigue crack growth region was characterised by a faceted structure, caused by a preferred crack growth direction in the aluminium matrix. This was comparable with the fracture surfaces found for the commercial MMCs and it seemed that the crack propagated solely through the aluminium, since practically no particles were to be seen on the fracture surfaces. For higher volume fractions, very small amounts of Al_2O_3 particles were observed, which might indicate fracture proceeding through the MMC network. Figure 4.22 shows the stable crack growth region for specimens containing 10 and 22 vol.% Al_2O_3 particles respectively. The stable crack growth regions in the experimental MMCs were comparable with the stable crack growth regions found for the commercial MMCs. The fracture surfaces were characterised by the presence of dimples and sometimes initiation of voids at the broken particles was observed.

Based on these observations, it may be concluded that the adherence of the Al_2O_3 particles to the matrix in the experimental MMCs is at least as good as in the Duralcan material. Hence, the possible difference in K_{Ic} Duralcan and K_{Ic} MMC 22 (7) may provisionally be attributed to morphology differences.

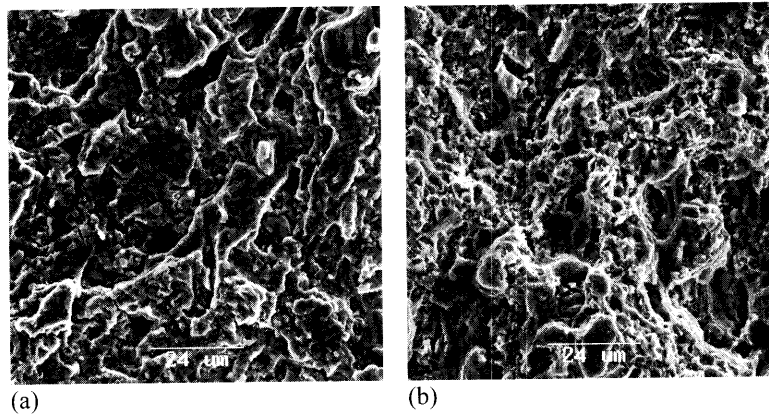


Figure 4.21
Fatigue crack growth region of MMC specimens with (a) 10 vol.% Al_2O_3 and (b) 22 vol.% Al_2O_3

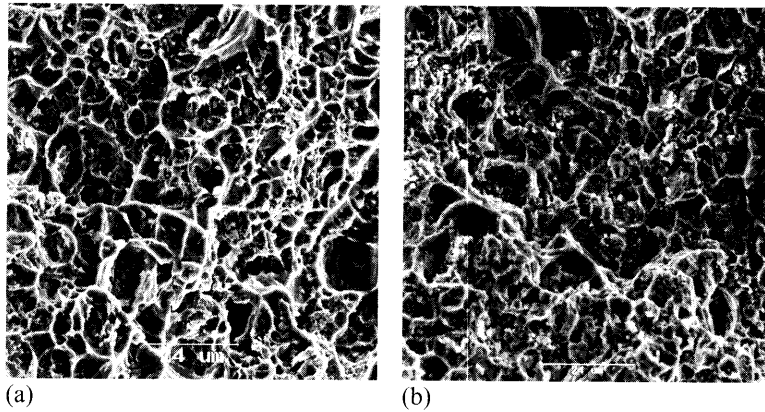


Figure 4.22

Stable crack growth region of MMC specimens with (a) 10 vol.% Al_2O_3 and (b) 22 vol.% Al_2O_3

4.8 Conclusions

- Different heat treatments leading to predominantly β'' (B), predominantly β' (C) or a mixture of these precipitates (T6 or T651), lead to large differences in yield strength in the unreinforced AA6061, *i.e.* the yield strength of the AA6061 in condition C is about 30% lower than in the other two conditions.
- It is possible to obtain valid K_{Ic} values for MMCs with the standard disk-shaped compact tension geometry, whereby the crack length during fatigue precracking can be determined using the compliance method.
- Although determination of the fracture toughness using the J-integral resulted in invalid K_J values, this method turned out to be suitable for characterising the fracture toughness of MMCs with various volume fractions Al_2O_3 particles.
- Critical evaluation of all the requirements for valid K_{Ic} values showed that many of the literature data for unreinforced AA6061, including our own, are invalid.
- The K_{Ic} of the Duralcan MMC is around 21 $MPa\sqrt{m}$ in heat treatment conditions B and C, which is only moderately lower than the K_{Ic} of AA6061 found in literature, which is on average 27 $MPa\sqrt{m}$.
- The K_{Ic} values of the Duralcan MMC in conditions B and C are similar and seem to be independent of heat treatment.
- Investigation of experimental MMCs showed that the ASTM E1737 method predicts an obvious trend for the variation of fracture toughness with volume fraction reinforcing Al_2O_3 particles whereas the ASTM E399 method does not.
- For the experimental MMCs, the fracture toughness decreases approximately linearly with increasing volume percentages of Al_2O_3 .

part B

Modelling Mechanical Behaviour

5

MODELLING PARTICLE FRACTURE USING WEIBULL STATISTICS

5.1 Introduction

Work on commercial aluminium alloys reinforced with either Al_2O_3 or SiC particles [18, 100-102] has demonstrated that reinforcements are broken progressively during plastic deformation and that the survival probability decreases with reinforcement size. In this chapter, fracture in an AA6061-based metal matrix composite (MMC) containing 20 vol.% Al_2O_3 particles is modelled using an axisymmetrical finite element model and a statistical approach for calculating the strength of reinforcing ceramic particles via the Weibull model [105]. Within this model, variables such as loading triaxiality, particle size and matrix alloy properties can be varied to investigate the parameter dependence of particle fracture. When modelling the fracture behaviour of one particle, it is assumed that the survival probability of the ceramic particle is governed by a Weibull distribution. Fracture statistics of the MMC is examined by plotting the survival probability of an Al_2O_3 particle versus the macroscopic axial stress applied on the whole MMC.

5.2 Cell Model

Micromechanical models for ductile damage and fracture are based on the notion that these physical processes can be described by the structural behaviour of relatively simple unit cells [103]. Cell model calculations are normally used to study microscopic voids in ductile materials [104]. However, in this research, a cell model is used to study metal matrix composites by simulating their behaviour for varying triaxiality of the stress state. An acceptable disadvantage of this approach is, that the relative position of the ceramic particles in the matrix is fixed.

The continuum is considered to consist of a periodic assemblage of hexagonal unit cells approximated by circular cylinders, see figure 5.1, which allows for an axisymmetrical calculation. Every cell of initial length $2L_0$ and radius R_0 contains a spherical particle of radius r_0 . In order to simulate the constraint of the surrounding material, the cylindrical cell is required to remain cylindrical throughout the deformation history, *i.e.* the top and bottom faces as well as both sides should remain flat and parallel.

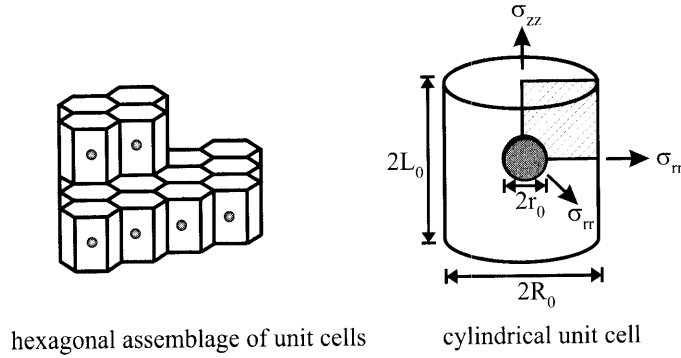


Figure 5.1
Micromechanical modelling of a matrix containing a spherical particle

During deformation, the surfaces normal to the axial and radial directions are subjected to homogeneous displacements in these directions respectively, whereby the ratio, ρ , of the average applied true stresses σ_{rr} and σ_{zz} is kept constant. This ratio is often called the stress proportionality factor and is given by [33]:

$$\rho = \frac{\sigma_{rr}}{\sigma_{zz}} \quad (5.1)$$

whereby σ_{rr} is the stress in the radial direction and σ_{zz} in the axial direction.

5.3 Weibull Model

When modelling the survival probability of ceramic, the Weibull model [105] is often found to be applicable [106]. If one can assume the flaw size distribution to be fractal-like, this approach will be valid regardless of their size [107]. The size of a critical flaw will simply become smaller and the particle strength increases, as the particle volume decreases. A fractal distribution will ensure that there is always a distribution of flaws within the particles on a scale finer than the particle size.

Using Weibull statistics, the survival probability, S , of a ceramic volume, V , in case of a uniform stress distribution is governed by:

$$S = \exp \left\{ - \frac{V}{V_0} \left(\frac{\sigma}{\sigma_0} \right)^m \right\} \quad (5.2)$$

where σ is the stress in the particle, σ_0 and V_0 are two constants with dimensions of stress and volume (σ_0 is often referred to as the characteristic stress), respectively, which are introduced for dimensional purposes [108] and m is the Weibull modulus. This equation can be rewritten, allowing a straight line representation of gradient m , when $\ln \ln(1/S)$ is plotted against $\ln \sigma$:

$$\ln \ln \frac{1}{S} = \ln \left(\frac{V}{V_0} \right) + m \cdot \ln \sigma - m \cdot \ln \sigma_0 \quad (5.3)$$

The strength of a ceramic particle is essentially limited by pre-existing critical flaws which are present in the material, *i.e.* surface and volume flaws. In the present model, it is assumed that flaws on the surface have no greater influence than those in the interior. If surface flaws dominate failure, then the volume term (V/V_0) should be replaced by an area term (A/A_0) [107].

5.4 Finite Element Calculations

The MMC is modelled with a matrix of AA6061 ($E = 69$ GPa, $\nu = 0.33$, $\sigma_{ys} = 295$ MPa) and 20 vol.% Al_2O_3 particles with a diameter of 4 μm or 8 μm ($E = 393$ GPa, $\nu = 0.27$, and a fictitious high yield strength to prevent plastic deformation in the ceramic particle). E is the elastic modulus, ν is Poisson's ratio and σ_{ys} is the yield stress. The behaviour of a ductile aluminium matrix is studied for two hardening exponent values n (*i.e.* $n = 4.35$ and 15.82). The first is a value from literature for AA6009-T4 [109] measured on tensile specimens in the extruded direction, the latter is a value measured in the laboratory, on tensile specimens AA6061-T651 taken perpendicular to the extruded direction. The hardening exponent is defined in the uniaxial stress-strain relation in the form of a piece-wise power law:

$$\epsilon = \begin{cases} \frac{\sigma}{E} & \text{if } \epsilon \leq \frac{\sigma_{ys}}{E} \\ \frac{\sigma_{ys}}{E} \left(\frac{\sigma}{\sigma_{ys}} \right)^n & \text{if } \epsilon > \frac{\sigma_{ys}}{E} \end{cases} \quad (5.4)$$

Finite element calculations are done for $\rho = 0$ (uniaxial tensile test) and $\rho = 0.1, 0.3, 0.5$ and 0.7 (triaxial tensile tests). For all calculations, a particle with a diameter of 4 μm , $m = 15$, $\sigma_0 = 350$ MPa, $\sigma_{ys} = 295$ MPa, a hardening exponent for the matrix of $n = 15.82$ and $V_0 = 1 \text{ mm}^3$ is considered to be the reference situation for the MMC.

In order to calculate the survival probability of a ceramic particle in an MMC, calculations on the cylindrical unit cell have been performed using the MARC finite element program [110]. The finite element mesh used for calculations consisted of 350 isoparametric quadrilateral 4-node elements (140 for the particle and 210 for the matrix), as shown in figure 5.2, whereby only the region hatched in figure 5.1 needs to be considered due to symmetry.

For every of the four integration points of each finite element belonging to the particle, the principal stresses σ_1 , σ_2 and σ_3 are calculated and these values are averaged to get the three principal stresses for each element. Furthermore, the volume of each element is calculated. Using the stresses, the net applied stress σ in the particle is calculated using the Drucker-Prager criterion (from this point forward this stress will be denoted as σ_{DP}):

$$\sigma_{DP} = \sqrt{\frac{1}{2}[(\sigma_1 - \sigma_2)^2 + (\sigma_2 - \sigma_3)^2 + (\sigma_3 - \sigma_1)^2]} + \frac{1}{3}\alpha(\sigma_1 + \sigma_2 + \sigma_3) \quad (5.5)$$

where α is related to the ratio of compression strength and tensile strength of the material and can be calculated using the following equation:

$$\alpha = 3 \frac{(\sigma_c / \sigma_t - 1)}{(\sigma_c / \sigma_t + 1)} \quad (5.6)$$

where σ_c and σ_t are the compression strength and tensile strength respectively. In the present calculations $\sigma_c / \sigma_t = 10$ is used. Now, for a given σ_0 and m , the survival probability S can be calculated.

It should be mentioned that debonding of ceramic particles is excluded in this investigation, since the present model does not contain a criterion with which the occurrence of interface failure between the ceramic particle and its surrounding aluminium matrix can be calculated.

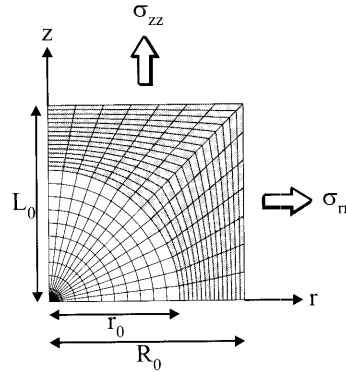


Figure 5.2 *Finite element mesh used for calculations, white elements represent the ceramic particle and grey elements represent the aluminium matrix; z is axial direction and r is radial direction*

5.5 Parameter Dependence

In this investigation, the parameter dependence of particle fracture in proportional loading histories is examined. The parameters varied are the loading ratio via the constant ρ , the Weibull modulus m , the hardening exponent n for the matrix, the characteristic stress σ_0 , the yield stress σ_{ys} for the matrix and the diameter of the ceramic particle. For all calculations, data are plotted against the macroscopic applied axial stress σ_{zz} , since σ_{DP} varies from element to element.

5.5.1 Reference Configuration

In figure 5.3, the survival probability is plotted as a function of the macroscopic axial stress applied on the unit cell for the reference state of the MMC.

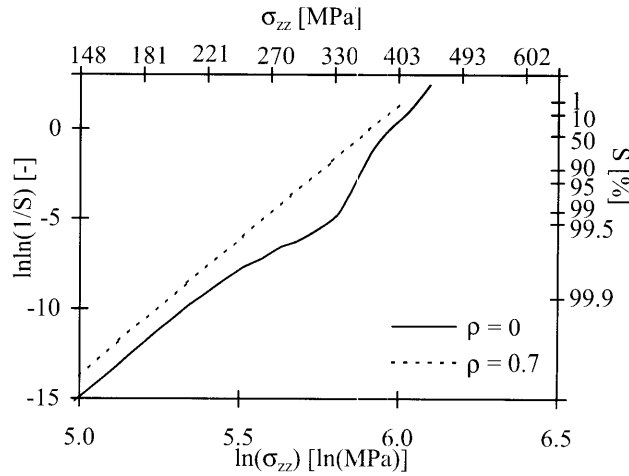


Figure 5.3

Survival probability S as a function of macroscopic axial stress σ_{zz} for a particle with a diameter of $4 \mu\text{m}$ with loading ratios $\rho = 0$ and 0.7 ($m = 15$, $\sigma_0 = 350 \text{ MPa}$, $\sigma_{ys} = 295 \text{ MPa}$ and $n = 15.82$)

Regarding $\rho = 0.7$, this calculation results in a straight line of gradient 15 which is the value that was used for the Weibull modulus m . When comparing loading ratios $\rho = 0$ and 0.7 , it can be seen that at lower stresses both calculations result in a straight line of gradient 15, *i.e.* the survival probability variation of the unit cell equals that of the ceramic particle. However, when the stress exceeds $\ln(\sigma_{zz}) = 5.5 \approx 245 \text{ MPa}$, curvature occurs in case of $\rho = 0$, whereas the calculation with $\rho = 0.7$ remains a straight line. Furthermore, it is observed that a triaxial loading ratio results in a lower survival probability of the ceramic particle than the uniaxial loaded case.

From the above, it can be concluded that in case of $\rho = 0.7$, the survival probability of the ceramic particle is governed by a Weibull distribution, whereas for $\rho = 0$ this is no longer the case from the point where curvature starts.

5.5.2 Loading History

For different loading histories, data is plotted against the macroscopic applied axial stress in figure 5.4. Regarding $\rho = 0.5$ and 0.7 , these calculations result in a straight line with slope 15 which again is the value used for the Weibull modulus m . Overall, it is observed that the higher the stress proportionality factor ρ , the lower the survival probability of the ceramic particle becomes. It can be concluded that in case of $\rho = 0.5$ and 0.7 , the survival probability

of the ceramic particle is governed by a Weibull distribution, whereas for $\rho = 0, 0.1$ and 0.3 this is no longer the case from the point where curvature starts.

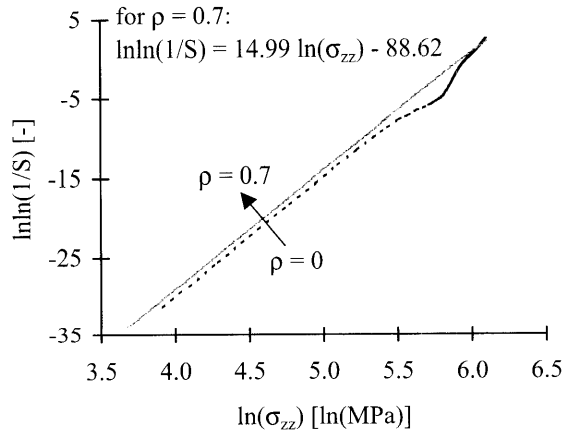


Figure 5.4

Survival probability S as a function of macroscopic axial stress σ_{zz} for a particle with a diameter of $4 \mu\text{m}$ with loading histories $\rho = 0, 0.1, 0.3, 0.5$ and 0.7 ($m = 15$, $\sigma_0 = 350 \text{ MPa}$, $\sigma_{ys} = 295 \text{ MPa}$ and $n = 15.82$)

5.5.3 Weibull Modulus

To verify whether the gradient in figures 5.3 and 5.4 is the Weibull modulus m , calculations were also done for a different value ($m = 20$). The results of these calculations are shown in figure 5.5, where the survival probability is plotted as a function of macroscopic axial stress for $m = 15$ and 20 , again with loading ratios $\rho = 0$ and 0.7 (particle diameter = $4 \mu\text{m}$, $n = 15.82$ and $\sigma_0 = 350 \text{ MPa}$). These calculations result indeed in gradients 15 and 20 , so the straight lines do represent the Weibull modulus m . The overall appearance in case of $\rho = 0$ or 0.7 remains the same, i.e. a straight line of a gradient of the applied m for $\rho = 0.7$ and the occurrence of curvature for $\rho = 0$, whereby the shape of curvature differs slightly for both m -values.

5.5.4 Stresses in the Particle

Equations (5.2) and (5.3) are valid for a uniform stress distribution in ceramics [106]. To investigate the uniformity of the stress in the particle, 15 nodes near the interface were chosen and for these nodes the actual Drucker-Prager stress σ_{DP} was calculated with equation (5.5) for both loading ratios $\rho = 0$ and 0.7 and plotted versus the macroscopic axial stress σ_{zz} in figure 5.6.

It can be seen that there is a linear relation between σ_{DP} and σ_{zz} up to approximately 330 MPa in case of $\rho = 0$ and up to approximately 850 MPa in case of $\rho = 0.7$. When the stress becomes higher than 330 MPa or 850 MPa , σ_{DP} turns out to be dependent on the position in

the particle, *i.e.* at the same macroscopic axial stress, all 15 nodes have a different Drucker-Prager stress.

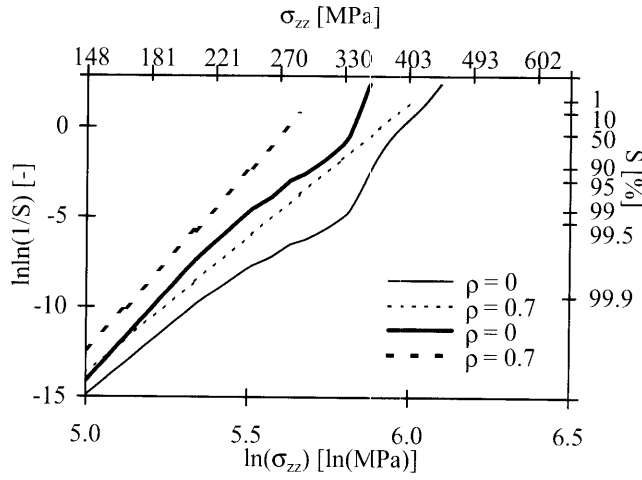


Figure 5.5

Survival probability S as a function of macroscopic axial stress σ_{zz} for $m = 15$ and 20 with loading ratios $\rho = 0$ and 0.7 (particle diameter = $4 \mu\text{m}$, $\sigma_{ys} = 295 \text{ MPa}$, $n = 15.82$ and $\sigma_0 = 350 \text{ MPa}$); thin and thick lines are for $m = 15$ and 20 respectively

Because of the stress distribution in the particle not being uniform, the applied stress σ in equations (5.2) and (5.3) should actually be replaced by $\sigma_{DP}(\underline{x}) = \sigma_{zz} f(\underline{x})$, where $f(\underline{x})$ is some function of the position \underline{x} in the particle. Equation (5.3) then becomes:

$$\ln \ln \frac{1}{S} = \ln \left(\frac{\int_V f(\underline{x})^m dV}{V_0} \right) + m \cdot \ln \sigma_{zz} - m \cdot \ln \sigma_0 \quad (5.7)$$

From this equation it can be seen, that as a result of non-uniformity of the stress, there is an additional factor, which explains the translation along the survival probability axis when going from $\rho = 0$ to 0.7 .

To explain the curvature occurring for $\rho = 0$ in figures 5.3, 5.4 and 5.5, it can be concluded from figure 5.6 that, in a plot of $\ln \ln(1/S)$ versus $\ln(\sigma_{zz})$, from the point where a straight line is no longer obtained, the stresses in the particle are not only non-uniform, but also non-proportional due to plasticity in the matrix surrounding the ceramic particle. Now, $f(\underline{x})$ in equation (5.7) is also a function of σ_{zz} . For $\rho = 0$, it turns out that the regime where the stresses become non-proportional is just where the survival probability goes rapidly from 1 to 0, while for $\rho = 0.7$ this is at a stress of approximately 850 MPa, which will not be reached in this calculation. The latter can be seen in figure 5.7, in which the survival probability is

plotted versus the Von Mises stress ($\sigma_{VM} = \sigma_{zz}(1 - \rho)$) for the reference configuration with $\rho = 0$ and 0.7 , where for the latter a survival probability of zero is already reached at a Von Mises stress just above 100 MPa. From figure 5.8, where the stress - strain relation is plotted for both ρ - values it can also be seen, that in case of $\rho = 0.7$ the ceramic particles thus fracture well below the yield stress in the elastic regime.

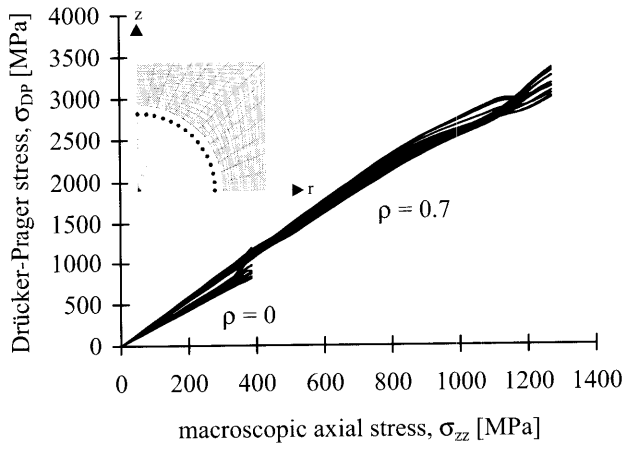


Figure 5.6

Drucker-Prager stress σ_{DP} as a function of macroscopic axial stress σ_{zz} for 15 nodes near the interface of the particle with a diameter of $4 \mu m$ ($\sigma_{ys} = 295$ MPa and $n = 15.82$)

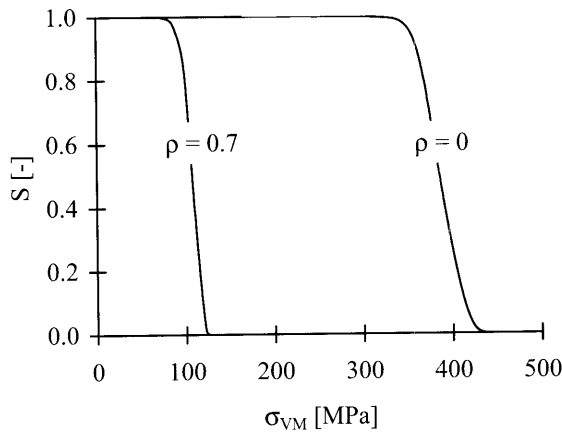


Figure 5.7

Survival probability S as a function of macroscopic axial stress σ_{zz} for a particle with a diameter of $4 \mu m$, $\rho = 0$ and 0.7 ($m = 15$, $\sigma_0 = 350$ MPa, $\sigma_{ys} = 295$ MPa and $n = 15.82$)

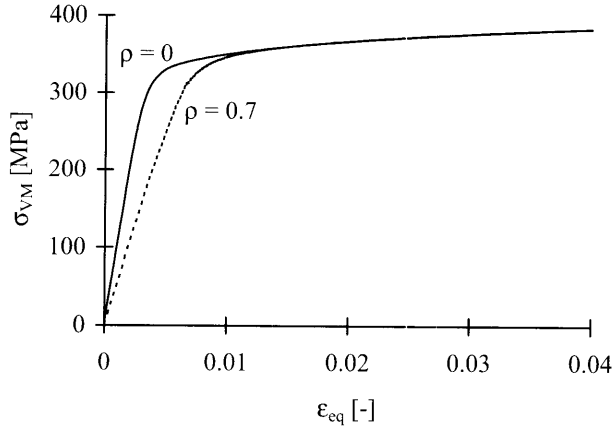


Figure 5.8

Calculated stress - strain curves for a particle with a diameter of 4 μm , $\rho = 0$ and 0.7, $\sigma_{ys} = 295$ MPa and $n = 15.82$

5.5.5 Matrix Hardening

If plasticity in the matrix surrounding the ceramic particle causes the curvature for $\rho = 0$, it seems useful to investigate the influence of different hardening exponents n for the aluminium matrix material. The results of these calculations are shown in figure 5.9. The survival probability is plotted as a function of macroscopic axial stress for an MMC with an AA6061 matrix with hardening exponents $n = 4.35$ and 15.82 respectively, and loading ratios $\rho = 0$ and 0.7 (particle diameter = 4 μm , $m = 15$ and $\sigma_0 = 350$ MPa).

Again, a straight line of gradient 15 and the curvature in case of $\rho = 0$ above $\ln(\sigma_{zz}) = 5.5$ is observed. In case of $\rho = 0.7$, both calculations coincide completely and for $\rho = 0$ the calculations coincide up to the point where curvature starts. For $\rho = 0.7$, this means that a variation of the hardening exponent is of no influence since the matrix material remains elastic throughout the loading history. However, in case of $\rho = 0$, a lower hardening exponent results in less curvature.

5.5.6 Characteristic Stress and Yield Stress

When varying the characteristic stress σ_0 , a parallel shift of the curves is observed. This can be seen in figure 5.10, in which for a particle with a diameter of 4 μm , $m = 15$ and $n = 15.82$, the results for characteristic stresses $\sigma_0 = 350$ MPa and 525 MPa are shown for a loading ratio $\rho = 0$. As indicated in this figure, the shift between the calculations can be derived from equation (5.7) as being $\ln(350/525)^{15} = -6.1$.

Since all calculations for $\rho = 0$ start with a straight line of gradient m , but start to curve when the macroscopic axial applied stress approximates the yield stress of the matrix material,

results are also shown for calculations with three different matrix yield stresses namely, $\sigma_{ys} = 200$ MPa, 295 MPa and 400 MPa.

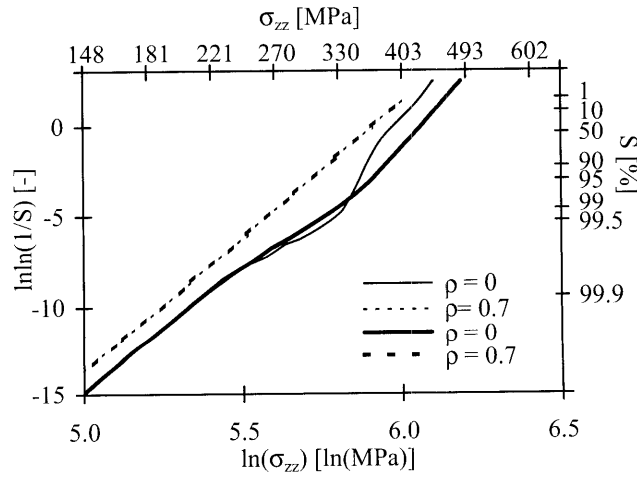


Figure 5.9

Survival probability S as a function of macroscopic axial stress σ_{zz} for hardening exponents $n = 4.35$ and 15.82 with loading ratios $\rho = 0$ and 0.7 (particle diameter = $4 \mu\text{m}$, $m = 15$, $\sigma_{ys} = 295$ MPa and $\sigma_0 = 350$ MPa); thick and thin lines are for $n = 4.35$ and 15.82 respectively

Equation (5.7) can be rewritten in the following equation:

$$\ln \ln \frac{1}{S} + m \cdot \ln \frac{\sigma_0}{\sigma_{ys}} = \ln \left(\frac{\int f(\underline{x})^m dV}{V_0} \right) + m \cdot \ln \frac{\sigma_{zz}}{\sigma_{ys}} \quad (5.8)$$

Now, if the left-hand term of this equation is plotted on the vertical axis and $m \ln(\sigma_{zz}/\sigma_{ys})$ on the horizontal axis, a 'mastercurve' can be created eliminating the effect of σ_0 and σ_{ys} . Two variables which still affect the mastercurve are the matrix hardening exponent and the Weibull modulus; the first changes the curvature and the latter results in a vertical shift. An example is given in figure 5.11 for $n = 15.82$. It turns out that, as long as all deformations in the MMC are purely elastic, $f(\underline{x})$ is independent on the applied stress, resulting in a gradient 1. As soon as plasticity in the surrounding matrix occurs, $f(\underline{x})$ becomes dependent on the applied stress and the mastercurve diverges from this gradient.

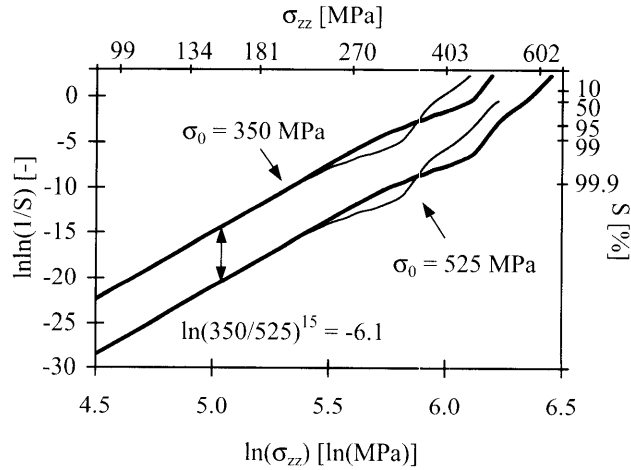


Figure 5.10

Survival probability S as a function of macroscopic axial stress σ_{zz} for characteristic stresses $\sigma_0 = 350$ MPa and 525 MPa and matrix yield stresses $\sigma_{ys} = 200$ MPa, 295 MPa and 400 MPa with loading ratio $p = 0$ (particle diameter = 4 μm , $m = 15$ and $n = 15.82$); a thicker line corresponds with a higher yield stress

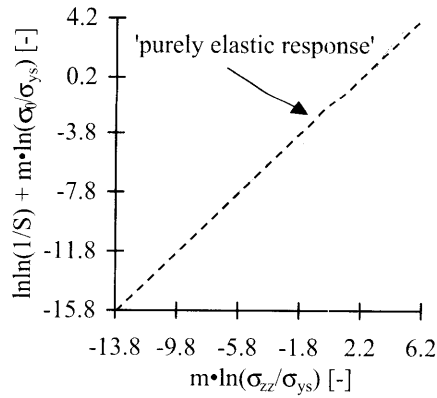


Figure 5.11

'Mastercurve' for characteristic stresses $\sigma_0 = 350$ and 525 MPa and matrix yield stresses $\sigma_{ys} = 200$ MPa, 295 MPa and 400 MPa, all for a fixed value $n = 15.82$ and $m = 15$

5.5.7 Particle Size

Finally, when the particle diameter is doubled from 4 to 8 μm diameter, it can be seen in figure 5.12 that, for the same loading ratio, the survival probability decreases with increasing particle diameter. Besides a shift along the survival probability axis which can be explained with equation (5.3) through the larger volume, calculations for a particle with a diameter of 8 μm result in comparable lines as for a diameter of 4 μm ; *i.e.* a straight line of gradient $m = 15$ in case of $\rho = 0.7$ and curvature above a certain σ_{zz} -value for $\rho = 0$. For 8 μm diameter it turns out that curvature is to a lesser extent than for 4 μm .

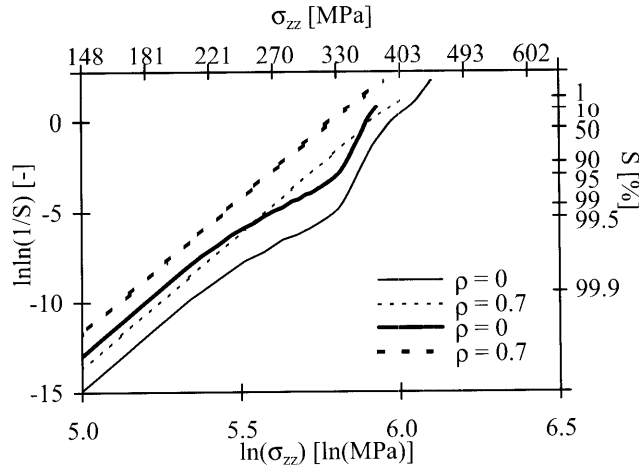


Figure 5.12

Survival probability S as a function of macroscopic axial stress σ_{zz} for particles with a diameter of 4 and 8 μm with loading ratios $\rho = 0$ and 0.7 ($m = 15$, $\sigma_0 = 350 \text{ MPa}$, $\sigma_{ys} = 295 \text{ MPa}$ and $n = 15.82$); thin and thick lines are for $d = 4$ and 8 μm respectively

5.6 Conclusions

- Based on present calculations it can be concluded that the relation between the macroscopic applied stress on the MMC and the survival probability of the ceramic particle can be described by the Weibull modulus m , as long as the stress distribution in the matrix surrounding the particle is proportional to the applied load, *e.g.* in figure 5.6, the particle should fail at a stress in the range where there is a linear relation between the Drucker-Prager stress σ_{DP} and the macroscopic axial stress σ_{zz} .
- When loading the metal matrix composite triaxially ($\rho > 0$) instead of uniaxially ($\rho = 0$), the survival probability of the Al_2O_3 particle is lower and the particle is likely to fail before plasticity in the matrix occurs.

5. Modelling Particle Fracture Using Weibull Statistics

- Considering the parameter dependence of particle fracture, it can be concluded that for the same loading ratio,
 - an increase in the hardening exponent n of the matrix, results in coinciding calculations for $\rho = 0.7$ and for $\rho = 0$ the calculations coincide up to the point where curvature starts, whereby a lower hardening exponent results in less curvature,
 - a variation of the characteristic stress σ_0 results in a parallel shift of the curves for both $\rho = 0$ and $\rho = 0.7$,
 - a 'mastercurve' for a fixed value of n can be made independent of characteristic stresses σ_0 and matrix yield stresses σ_{ys} and
 - an increase of particle diameter (and thus volume of the ceramic particle) decreases the survival probability of an Al_2O_3 particle in an AA6061 aluminium matrix.

6

MODELLING DAMAGE IN MMCS USING GURSON'S MODEL

6.1 Introduction

In ductile metals, voids mainly nucleate during plastic deformation, when second phase particles crack or debond from the surrounding matrix, and final fracture involves the growth of neighbouring voids to coalescence. This concept can be applied to metal matrix composites (MMCs), whereby the reinforcing particles act as nucleation sites for voids, either by decohesion of the particle/matrix interface or by particle fracture. Final fracture of the material also involves the growth of neighbouring voids to coalescence. Based on the approximation of a porous plastic solid, Gurson [31] proposed a constitutive relation for a progressively cavitating solid. The model has been modified by Tvergaard and Needleman [111]. Their model is used here to simulate the fracture mechanical behaviour of MMCs and to predict the fracture toughness as a function of heat treatment. The analysis in this chapter relies on the simplifying assumption that all voids are initially present in the material due to fracture of the ceramic particles. It should be mentioned that assuming broken particles in front of the crack tip replaced by voids is a rather rough assumption, since the volume of a void is much more than that of a broken particle.

In cracked configurations the assumption that all particles in front of the crack tip are broken, is justified by the fact that the fracture process takes place in the direct vicinity of the crack tip, where the constraint in terms of the p parameter as used in chapter 5 is approximately equal to 0.7 [112]. It was also demonstrated in chapter 5 that at this level of constraint particle fracture already occurs during elastic deformation, *i.e.* prior to plastic deformation during which the process of void growth and final coalescence takes place. The model is tested on disk-shaped compact tension specimens to investigate the influence of various heat treatment conditions and various volume fractions reinforcing particles on the fracture toughness. Similar modelling of the experimental MMC, of which the production and fracture toughness is discussed in chapter 4, was not possible because the Gurson model cannot handle the extremely high void volume fractions resulting from fracture of the ceramic particles as found in the MMC network of this material.

6.2 Continuum Model for Voided Material

Since plastic dilatation will be the apparent macroscopic effect of void growth in a ductile material, this must be accounted for when representing the response of a ductile void-containing material with a continuum model. The approximate yield condition formulated by Gurson [31] is based on spherically symmetric deformations around a single spherical void and in a form modified by Tvergaard [32] is given in equation (6.1):

$$\Phi = \left(\frac{\sigma_{VM}}{\sigma_M} \right)^2 + 2f^* q_1 \cosh \left\{ \frac{q_2 \sigma_{kk}}{2\sigma_M} \right\} - \left[1 - (q_1 f^*)^2 \right] = 0 \quad (6.1)$$

where Φ is the flow potential, σ_{VM} is the macroscopic Von Mises stress, σ_M is the average Von Mises stress in the matrix, σ_{kk} is the hydrostatic stress and f^* is a function of the void volume fraction f . Tvergaard introduced the additional parameters q_1 and q_2 because Gurson's yield function resulted in too high maximum loads and bifurcation at loads that were too small and strains that were twice the values found numerically. With f^* equal to f and $q_1 = q_2 = 1$, equation (6.1) reduces to the function as originally proposed by Gurson.

Although the original Gurson model does permit a complete loss of stress carrying capacity at a critical void volume fraction, this critical void volume fraction is unrealistically high. Therefore, Tvergaard and Needleman [111] introduced the function $f^*(f)$ to model the rapid decrease in load carrying capacity if void coalescence occurs:

$$\begin{cases} f^*(f) = f & \text{if } f \leq f_c \\ f^*(f) = f_c + \frac{f_u^* - f_c}{f_F - f_c} (f - f_c) & \text{if } f > f_c \end{cases} \quad (6.2)$$

where f_c is the critical void volume fraction at which void coalescence starts, f_u^* is the ultimate void volume fraction ($= 1/q_1$) and f_F is the failure void volume fraction. So, in equation (6.2), the function $f^*(f)$ becomes active when f exceeds a critical value f_c and complete loss of stress carrying capacity (coalescence of voids) occurs when $f = f_F$. When the material reaches f_F , the material is considered to be failed. At this point, the stiffness and the stress for that specific element in a finite element mesh are reduced to zero.

The evolution of damage as measured by the void volume fraction, f , is due to the nucleation of new voids and the growth of existing voids, so the growth rate of f can be expressed by:

$$\dot{f} = \dot{f}_{\text{growth}} + \dot{f}_{\text{nucleation}} \quad (6.3)$$

In this investigation, nucleation of new voids is left out of consideration, since figures 5.7 and 5.8 in chapter 5 indicate that for high constraint ($\rho = 0.7$) the ceramic particles fracture well below the yield strength.

The derivation of stress-strain relations, together with the relations describing the rate of increase of the void volume fraction with plastic straining, from volume conservation and the yield function as formulated in equation (6.1) are given in various literature sources, *e.g.*

Tvergaard [32]. Therefore, this will not be repeated here. These relations now form a constitutive model including the softening effect due to the presence of voids and the development of the void volume fraction with plastic straining. This model is, however, fully non-dimensional, whereas various studies, *e.g.* Rice and Johnson [113], have shown that the mutual distance between voids play a dominant role in the ductile tearing process.

This is one important reason why a dimensional material parameter should be included in the model. A second reason for this is a more practical one. It is well-known that a non-dimensional (also called local) damage model causes mesh-dependent results in finite element simulations of situations with large spatial strain gradients, whereas a correct finite element simulation should converge to the exact solution with vanishing mesh size.

One way of introducing a dimensional parameter in the constitutive model is not to apply the local rate of the damage parameter (in this case the void volume fraction), but a weighted average value over a characteristic volume around the point of consideration; a method as proposed by Bazant *et al.* [114] for crack growth in concrete. A similar model for metal plasticity, using the modified Gurson model, was developed by Leblond *et al.* [115] and later used by Tvergaard and Needleman [116, 117]. They showed that with these so-called non-local constitutive models, practically mesh independent results can be achieved.

Another, more pragmatic method to include a dimensional parameter into the model is by applying the local model to a fixed size element mesh in the regions with large spatial gradients of plastic strains. Volume integrations over elements are done by numerical integration. For square (2D) or cubic (3D) regular Gaussian schemes are used, where the integration point value of a quantity (like the damage parameter) represents more or less the mean value of that quantity over the volume covered by that integration point. For a fixed size element mesh, the element size can then be regarded as a dimensional material parameter (also called the characteristic material length), *e.g.* Sun, Brocks and Schmitt [118] and Koppenhoefer and Dodds [119]. This solution will, however, only work when the characteristic material length is smaller than the element size required for a sufficiently converged solution.

The local model with a fixed size element mesh can be applied with any finite element system which has the modified Gurson model incorporated. However, the non-local model requires substantial additions and modifications to such finite element systems. Using a general purpose, commercial finite element program [110], this could not be achieved within the time available for this study. It was therefore decided to apply the local model with a fixed size element mesh.

6.3 Void Growth and Coalescence in MMCs

Apart from the known length scale problem, there is an important aspect in applying the (modified) Gurson model [120], namely how to specify the material parameters in the model. Besides the fully defined matrix yield strength, the parameters involved in the Gurson model can be classified as constitutive parameters, the initial parameter, the critical parameter and the failure parameter. The constitutive parameters, q_1 and q_2 decide the form of the constitutive equation and can usually be taken as constant for different materials, but the

initial, critical and failure parameters, f_0 and f_c , are material specific. The latter parameters can be obtained from comparison of numerical simulations with experiments.

When investigating damage in MMCs, it should be kept in mind that two different mechanisms play a role, *i.e.* damage evolution in the MMC as well as in the matrix material itself. The matrix material of all MMCs investigated is the aluminium alloy AA6061 of which tensile test results in various heat treatment conditions are available. Søvik [36] suggests an initial void volume fraction $f_0 = 0.001$ for this specific aluminium alloy, which will also be used in this study. Simulations with $f_0 = 0.001$ and values for f_c ranging from 0.0015 to 0.0030 were done and it turned out that the influence of the chosen f_c - value was very small. Therefore, the critical void volume fraction was taken as the calculated void volume fraction at the neck of the specimen at the moment that the calculated diameter reduction at the neck was approximately equal to that of the experimental specimen after fracture, *i.e.* $f_c = 0.0015$. The final fracture phase, *i.e.* when $f > f_c$ until f approaches f_F , is a rapid process which is not or hardly visible on the load record of the experiment and appears rather insensitive to the choice of f_F . A value of $f_F = 0.15$ was chosen. Figure 6.1 compares a finite element simulation of a tensile test using this initial void volume fraction with experimental results. These parameters will now be used for the matrix material in the subsequent cell model simulating the MMC with broken ceramic particles.

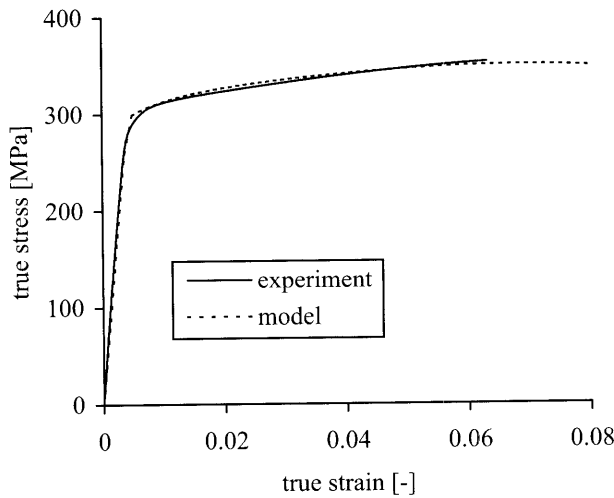


Figure 6.1

Parameter fitting for an AA6061-T651 tensile specimen ($\sigma_{ys} = 295$ MPa, $n = 15.82$)

Starting with broken ceramic particles in a ductile aluminium matrix, void growth can be calculated using an axisymmetric cell model as shown in figure 6.2. The approach used is identical to the one in chapter 5, so a periodic array of spherical voids is subjected to both axial and radial stresses via the stress proportionality factor ρ . Furthermore, the cylindrical cell surrounding each void must remain cylindrical throughout the deformation history in order to simulate the constraint of the surrounding aluminium. Note that this is a rather simplifying approach, as the rigid Al_2O_3 particle is now completely replaced by a void.

However, in the case of high stress triaxiality, *i.e.* at a crack tip, the approach used is considered to be acceptable.

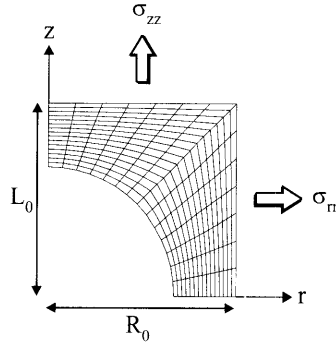


Figure 6.2

Finite element mesh used for void growth calculations, consisting of 210 axisymmetric isoparametric quadrilateral 4-node elements; z is axial direction and r is radial direction

Calculations are performed for proportional stress histories $0.1 \leq \rho \leq 0.7$, which cover the range from rather blunted crack tips to the triaxiality prevailing in sharp crack tip fields for weakly hardening solids [103]. In correspondence with MMCs containing 10, 20 or 30 vol.% reinforcing ceramic particles, three initial void volume fractions are considered, *i.e.* $f_0 = 0.10$, 0.20 and 0.30. Figures 6.3 and 6.4 show the unit cell response for a calculation with an initial void volume fraction $f_0 = 0.20$ and for which damage evolution in the surrounding matrix of AA6061-T651 is also accounted for ($\sigma_{ys} = 295$ MPa and $n = 15.82$). The evolution of the void volume fraction, is shown in figure 6.3 and calculated via [103]:

$$f = 1 - \frac{V_0}{V} (1 - f_0) - \frac{\Delta V_e}{V} \quad (6.4)$$

where V is the volume of the deformed cell, V_0 is the volume of the undeformed cell and ΔV_e the volume increase due to elastic dilatation as given in equation (6.5).

$$\Delta V_e = V_0 (1 - f_0) \frac{(1 - 2\nu)}{E} (\sigma_{zz} + 2\sigma_{rr}) \quad (6.5)$$

Calculations for $\rho = 0.5$ and $\rho = 0.7$ show overlap when regarding the void volume fraction evolution and unlike the case of $\rho = 0.1$ and 0.3 do not show a distinct critical void volume fraction from which an acceleration in void growth starts. Knowing $d\epsilon/d\epsilon_e$ and $\sigma_{VM,max}$, cell model predictions for $\rho = 0.7$, which represents the stress state existing at a crack tip, can be compared with the numerically solved constitutive equations of the Gurson model for the various initial void volume fractions (a variation in hardening exponent turned out to have no effect on these parameters). From the best fits found, it turned out that the parameters q_1 and q_2 can not be taken as constant for the three volume fractions considered here. The best-fit

values for q_1 , q_2 , f_c and f_F needed for the fracture toughness calculations on DSCT-specimens could be determined and are given in table 6.1. Cell model calculations are also performed with an aluminium matrix without damage accumulation and it turned out that void growth in the surrounding aluminium matrix is negligible with regard to voids present as a result of broken ceramic particles.

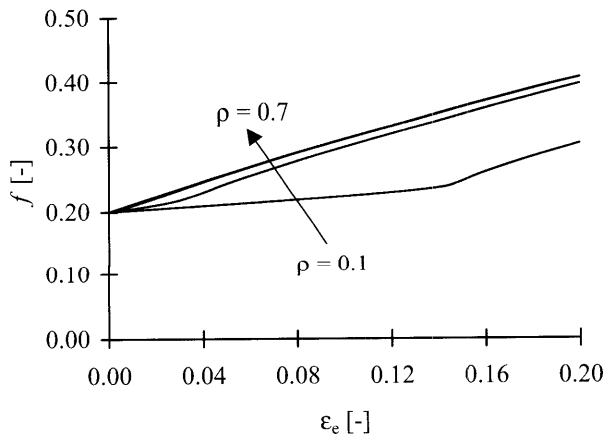


Figure 6.3

Evolution of the void volume fraction for $f_0 = 0.20$, $\sigma_{ys} = 295$ MPa and $n = 15.82$ with stress proportionality ratios $\rho = 0.1, 0.3, 0.5$ and 0.7

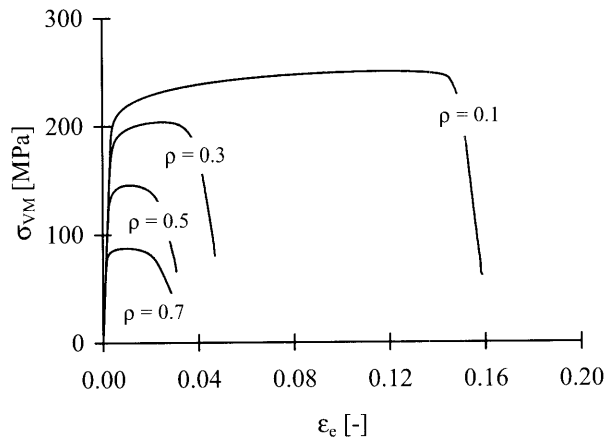


Figure 6.4

Macroscopic Von Mises stress variation with the macroscopic effective strain for $f_0 = 0.20$, $\sigma_{ys} = 295$ MPa and $n = 15.82$ with stress proportionality ratios $\rho = 0.1, 0.3, 0.5$ and 0.7

Table 6.1

Fitting parameters after comparison of cell model predictions with the Gurson model ($\rho = 0.7$)

| f_0 | f_c | f_F | q_1 | q_2 |
|-------|-------|-------|-------|-------|
| 0.10 | 0.112 | 0.15 | 1.67 | 0.93 |
| 0.20 | 0.225 | 0.25 | 1.98 | 0.73 |
| 0.30 | 0.330 | 0.36 | 1.92 | 0.64 |

6.4 Calculation of Fracture Toughness on DSCT-Specimens

Since it was not possible to perform tensile tests on the Duralcan MMC material, the hardening exponent and yield strength had to be calculated from stress-strain curves obtained with unit cell calculations. To do so, the finite element mesh from chapter 5 to calculate the survival probability was used (see figure 5.2). For each calculation the Al_2O_3 particles were modelled with a diameter of 4 μm ($E = 393$ GPa, $\nu = 0.27$ and a fictitious high value of the yield strength sufficient to prevent plastic deformation in the ceramic particle). The AA6061 matrix material is modelled with hardening exponents and yield strengths determined from tensile tests on this alloy in various heat treatment conditions ($E = 69$ GPa and $\nu = 0.33$). E is the Young's modulus and ν is Poisson's ratio. Typically the hardening exponent was reduced by 5% and the yield strength increased by 10% with respect to that of the unreinforced matrix material. The changes will be described in more detail in section 6.5.

To calculate the fracture toughness of the various materials, the finite element mesh for the DSCT specimen as shown in figure 6.5 is split up in three regions. The first region (light grey) consists of all elements surrounding the pin hole, the second of 4 rows of equally sized elements in front of the crack tip inside the trapezium (dark grey) and the third region is the remainder of the specimen. All elements are 4-node plane strain quadrilaterals with a 2×2 Gaussian integration scheme. The material around the pin hole is simulated with a sufficiently high yield strength to prevent plastic deformation in this area due to imposed displacements. For the elements in front of the crack tip, damage is accumulated by assuming that all voids are initially present in the material due to fracture of the ceramic particles. So, the material properties are those determined for aluminium with the initial volume fraction ceramic particles being voids; *i.e.* the parameters from table 6.1 are implemented here. The size of the elements (*i.e.* the characteristic material length parameter in the local constitutive description) is equal to 0.0273 mm, which is approximately 4 times the particle spacing. For a non-local description this would mean a characteristic length equal to the particle spacing, as the elements have 2 integration points in each direction and the length covered by each integration point is equal to twice the characteristic length in the non-local description. The third region then behaves as the uncracked MMC material.

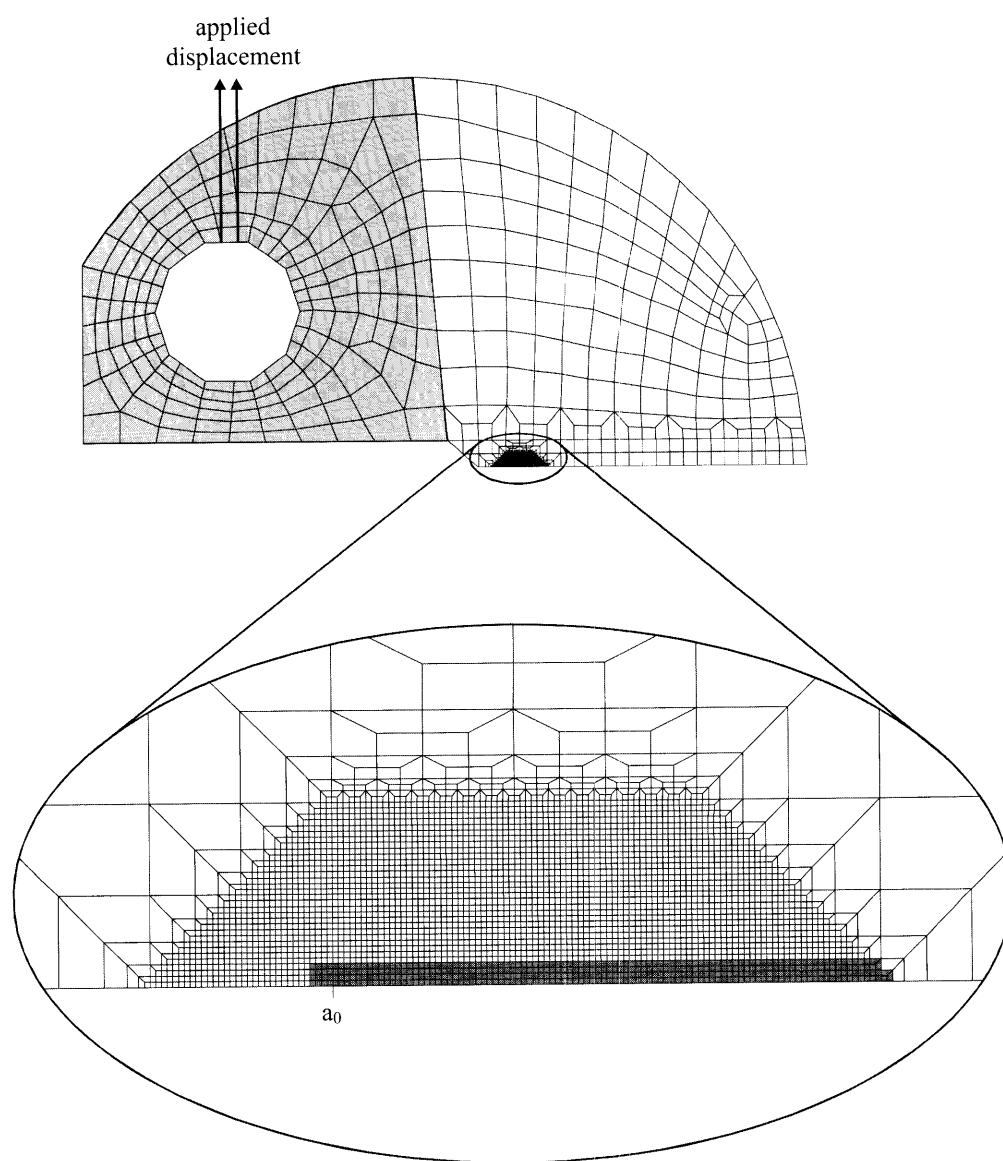


Figure 6.5
Finite element mesh of a DSCT-specimen to calculate K_Q , consisting of 3988 plane strain quadrilateral 4-node elements

During deformation of the model, an incremental displacement of 0.0002 mm is applied on the pin hole for each loading step. The applied load can be plotted versus the load-line displacement of the nodes used for deformation, after which a value of P_Q and thus K_Q can be derived using the standard tangent method as described in ASTM E399 [83].

6.5 Effect of Heat Treatment on Fracture Toughness

As mentioned in the previous section, the hardening exponent and yield strength of the MMC in various heat treatment conditions, which values are needed to calculate the fracture toughness, had to be determined using the unit cell approach. Tensile tests were performed on AA6061 matrix material in four conditions: the as-received T651 condition for which the specimen was tested perpendicular to the extruded direction, a self-made T6 condition and conditions B and C as described in chapter 2. Since the Duralcan MMC was tested in an as-received T6 condition and in conditions B and C, these three conditions are considered here. The DSCT-specimen was modelled with an initial crack length of 17.75 mm, an elastic modulus for the aluminium of 69 GPa and the elastic modulus for the MMC was calculated to be 98.8 GPa. The load-load-line displacement records obtained for these three finite element calculations are shown in figure 6.6. In table 6.2 the measured hardening exponents and yield strengths for the aluminium alloy as well as the calculated values for the MMC containing 20 vol.% Al_2O_3 particles, the calculated P_Q values and resulting K_Q values are listed.

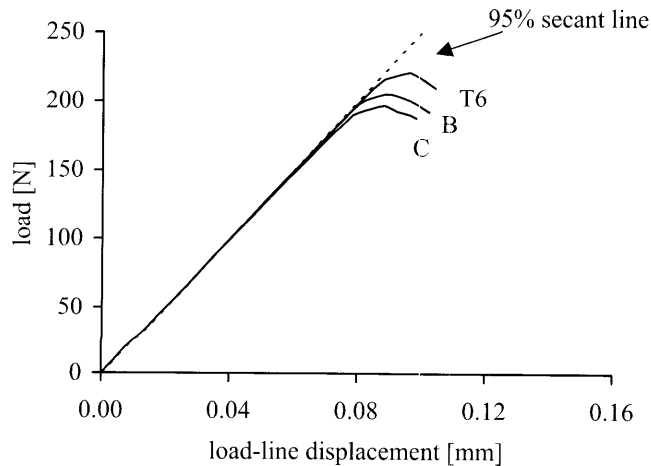


Figure 6.6

Load versus load-line displacement records for the Duralcan MMC in T6, B and C condition; crack tip elements of 0.0273 mm in size were used

Table 6.2

Measured (AA6061) and calculated (MMC) hardening exponents and yield strengths, which are used to calculate P_Q and K_Q in various heat treatment conditions

| Condition | n_{AA6061} | $\sigma_{\text{ys,AA6061}}$ | n_{MMC} | $\sigma_{\text{ys,MMC}}$ | P_Q | K_Q |
|-----------|---------------------|-----------------------------|------------------|--------------------------|-------|-------|
| B | 15.58 | 328 | 14.71 | 361 | 204 | 10.1 |
| T6 | 12.37 | 340 | 11.76 | 369 | 219 | 10.9 |
| C | 7.87 | 200 | 7.63 | 222 | 194 | 9.6 |

From this table no logical trend for the fracture toughness as a function of heat treatment is observed. For instance, the B condition has the highest hardening exponent of 15.58, but the calculated fracture toughness value is the middle one. On the other hand, the T6 condition has the highest yield strength and the middle hardening exponent, but this condition results in the highest calculated fracture toughness value. Overall, it can be concluded that the influence of the applied heat treatment on the fracture toughness is negligible, *i.e.* $K_{Ic,B} = 1.05 \times K_{Ic,C} = 0.93 \times K_{Ic,T6}$.

In comparison with the experiments described in chapter 4, section 4.6, the calculated K_Q values are rather low, *i.e.* the true experimental values range from 16.0 MPa√m in T6 condition to 22.4 MPa√m in the C condition. The calculated values can be increased by coarsening the crack path elements of the finite element mesh, *i.e.* by enlarging the characteristic material length parameter in the local constitutive model. The K_Q values listed in table 6.2 were derived from calculations using crack tip elements of 0.0273 mm in size, whereas table 6.3 shows K_Q values found for elements with double and fourfold this element size. Also the average fracture toughness values found experimentally are listed in this table.

Table 6.3
Calculated K_Q values in various heat treatment conditions, using various crack tip element sizes

| Condition | K _Q for various element sizes [MPa√m] | | | Experimental <K _Q > |
|-----------|--|-----------|-----------|-----------------------------------|
| | 0.0273 mm | 0.0546 mm | 0.1094 mm | |
| B | 10.1 | 13.8 | 17.5 | 20.4 |
| T6 | 10.9 | 14.8 | 18.4 | 16.1 |
| C | 9.6 | 12.9 | 14.9 | 21.6 |

Figure 6.7 compares the results of all calculations with the experimental observations. A shift to higher critical stress intensity values with increasing element size is indeed observed. For the largest element size, the predictions are close to the experimental values for the T6 and B conditions, but for the C condition the prediction is still relatively low.

The T6 condition is the only one for which the prediction is higher than the experimental values. However, these experimental values are rather questionable. They were both invalid due to a P_{max}/P_Q ratio larger than 1.10, most probably resulting in an underestimation of the fracture toughness. Another argument for this can be found from the results for the experimental material reinforced with 22 vol.% Al₂O₃ which is in T6 condition, as described in chapter 4. From the results in table 4.9, a fracture toughness value according to the ASTM E1737 standard [84] (which is considered to be the most reliable) of approximately 16 MPa√m is thought to be reasonable for this material. In view of the inverse microstructure of this experimental material, *i.e.* aluminium particles embedded in an MMC network with an extremely high volume fraction of Al₂O₃ particles, a fracture toughness value of approximately 16 MPa√m may be considered as a lower bound fracture toughness for the Duralcan MMC, in which case *all* numerical predictions still underestimate the fracture toughness.

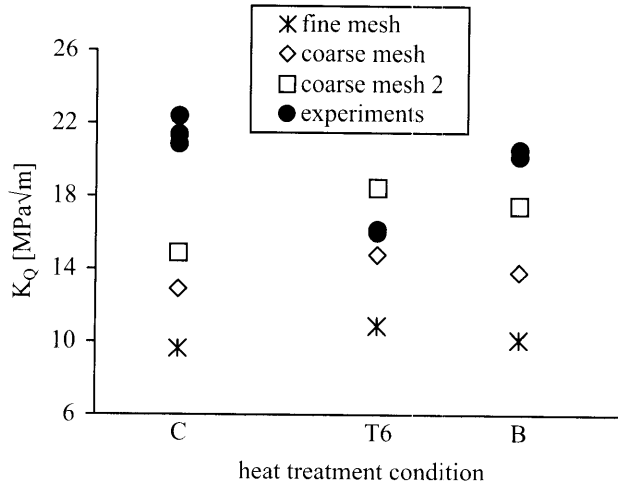


Figure 6.7

K_Q as a function of the hardening exponent for conditions T6, B and C, for three crack tip element sizes compared with experimental data for Duralcan MMC (fine mesh: 0.0273 mm; coarse mesh: 0.0546 mm; coarse mesh 2: 0.1094 mm)

Increasing the element size even more did not work, because this resulted in numerical instabilities, most probably because the element mesh then becomes too coarse to be able to describe the strain distribution around the crack tip correctly. Several explanations can be given for the relatively low values of the predictions:

1. The load carrying capability of the material along the fracture path is underestimated, because after fracture of a ceramic particle, it still remains bonded to the matrix, which means that the particle still contributes to the stiffness and strength of the damaged material. An attempt to model such material response in terms of the modified Gurson model was not successful. To describe this phenomenon, a completely different damage concept would be required. Another complication is, that both types of fracture behaviour, *i.e.* complete disintegration of the particles leaving a true void and single fracture of particles with fractions remaining bonded to the matrix, were observed.
2. The load carrying capability of the material along the fracture path is underestimated, because the matrix material is stronger than assumed in the cell model calculations, where a too small characteristic material parameter, *i.e.* element size, for this material had to be used. This problem can only be solved by applying a non-local material model for the matrix material, with a characteristic material length parameter larger than the applied element size.
3. The characteristic material length parameter of the damaged material along the crack path is larger than the element size required for a sufficiently converged solution. This problem also can only be solved by application of a non-local constitutive description of the material response.

Within the scope of this study, none of the above possible solutions could be explored. Irrespective of this, it can be concluded that both experiments and numerical predictions indicate that there is no significant influence of the applied heat treatment conditions on the fracture toughness of the Duralcan MMC.

6.6 Extrapolation of Concept

The experimental MMC, of which the production and measured fracture toughness is discussed in chapter 4, turned out to consist of an inverse microstructure, *i.e.* aluminium particles embedded in an MMC network. Since the added Al_2O_3 particles are located in this network, this resulted in extremely high volume fractions of Al_2O_3 particles. When extrapolating the concept as applied in the previous section for this material, it had to be concluded that the Gurson model cannot handle the extremely high void volume fractions resulting from fracture of ceramic particles which are located in this network.

However, experiments done on the experimental material showed that the fracture toughness decreased approximately linearly with increasing volume fractions Al_2O_3 particles. Therefore, cell model as well as fracture toughness calculations were done for MMCs with a microstructure comparable to that of the Duralcan MMC, containing 10, 20 and 30 vol.% ceramic particles. Since the experimental MMCs were tested in T6 condition, all cell model calculations were done with a hardening exponent for the matrix material of 12.4 and a yield strength of 340 MPa (see table 4.5).

Figure 6.8 shows the load versus load-line displacement records for the fracture toughness calculations on MMCs reinforced with either 20 or 30 vol.% Al_2O_3 particles. With regard to the 20 vol.% reinforced MMC, a reinforcement with 30 vol.% ceramic particles resulted in a fracture toughness decrease from $9.7 \text{ MPa}\sqrt{\text{m}}$ to $8.9 \text{ MPa}\sqrt{\text{m}}$. Cell model calculations on the MMC with 10 vol.% were successfully done, but those on the DSCT-specimen consistently resulted in numerical problems which could not be understood and solved.

As was already found experimentally, a decrease of the fracture toughness through the addition of 10% more ceramic particles is indeed observed, but unfortunately just for two volume percentages Al_2O_3 particles.

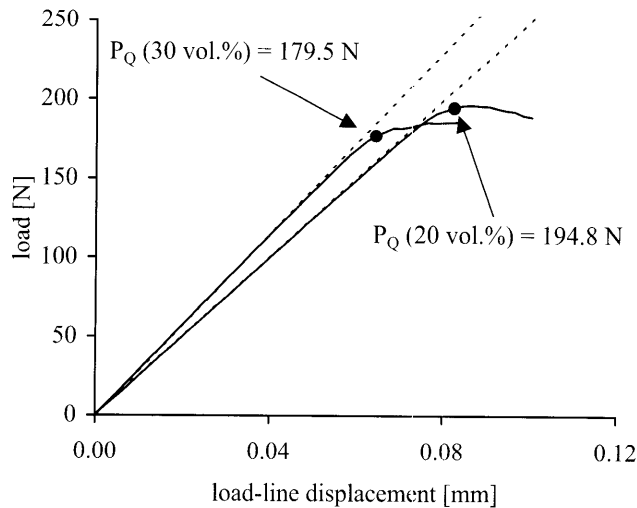


Figure 6.8

Load versus load-line displacement record for an MMC reinforced with 20 or 30 vol.% Al₂O₃ particles in T6 condition; crack tip elements of 0.0273 mm in size were used

6.7 Conclusions

- Numerical predictions indicate that no significant influence of the applied heat treatment conditions on the fracture toughness of the Duralcan MMC are to be expected. This effect is supported by experimental results.
- The Gurson model which in this numerical research is applied as a local model with a fixed sized element mesh turned out to be unfit for calculating the damage evolution in metal matrix composites properly, *i.e.* the predicted fracture toughness values are all rather low values.
- Calculations on MMCs containing 20 or 30 vol.% ceramic particles using the Gurson model resulted in a converged solution and showed a trend similar to the trend found experimentally, *i.e.* a decrease in fracture toughness with increasing volume fraction reinforcing particles. Calculations on an MMC reinforced with 10 vol.% could not converge due to numerical problems.
- The experimental MMC of which production and measured fracture toughness is described in chapter 4, cannot be modelled at all with the Gurson model since the MMC network in this material exhibits such a high void volume fraction due to fracture of the ceramic particles that the model exceeds its limits.

6.8 Concluding Remarks

The work presented in this thesis has been performed to investigate the fracture mechanical behaviour of precipitation hardenable aluminium-based MMCs. This fracture mechanical behaviour is mapped out with the use of the differential scanning calorimetry technique, the nanoindentation technique and fracture toughness measurements. These experimental techniques form the foundation for finite element calculations which are performed to calculate the influence of various variables such as the reinforcing particle size, the reinforcement volume fraction and the matrix ageing condition in isolation and to predict the fracture toughness as a function of heat treatment condition and volume fraction reinforcing particles.

Despite a lot of different precipitation sequences proposed in the literature, the differential scanning calorimetry technique has turned out to be very suitable for comparing the precipitation behaviour in AA6061 with an MMC based on this same alloy. Since the age-hardening sequence in the MMC turned out to be similar to that in the unreinforced AA6061 alloy, this simplified the finite element calculations, since mechanical properties of the various constituents could be applied independent of one another.

The same applies to the nanoindentation technique. This technique is not accurate in a way that it can measure the elastic modulus and hardness of the various constituents in an MMC exactly, but it turned out that there were hardly any differences between the AA6061 reference material and the AA6061 matrix of the MMC. This again supports the assumption in finite element calculations that the MMC matrix behaves similar as the same aluminium alloy without ceramic reinforcements.

Considering the fracture toughness experiments done in this research, the major conclusion might be that determination of stress intensity factors is even more difficult for MMCs than for a lot of other materials. First of all, MMCs are very difficult to machine into appropriate specimens for testing and crack growth during precracking can not be monitored easily. Therefore, the obtained results can only be put in perspective against a multitude of contradictory results reported in the literature. Another difficulty with this experimental part of this investigation is the fact that objections can be made against the results of the experimental MMCs.

As far as the finite element calculations are concerned, it is possible to investigate the influence of various variables such as the reinforcing particle size, the reinforcement volume fraction and the matrix ageing condition in isolation as long as the stress distribution in the matrix surrounding the ceramic particle is proportional to the applied load. Even a 'mastercurve' independent of characteristic stresses and matrix yield stresses can be made for a fixed value of the hardening exponent.

Using the Gurson model, an attempt was made to predict the fracture toughness of MMCs as a function of heat treatment condition and volume fraction reinforcing particles. With this model trends can be visualized to a certain extent, but the model turned out to be unfit for calculating the damage evolution in metal matrix composites properly. To improve the prediction of fracture toughness of MMCs, the assumptions should be refined or even a completely different strategy should be used.

REFERENCES

- [1] I. J. Polmear, *Light Alloys, Metallurgy of the Light Metals*, Edward Arnold, London, Great Britain, 1989
- [2] K. R. van Horn, *Aluminum - Volume I, Properties, Physical Metallurgy and Phase Diagrams*, American Society for Metals, Metals Park, Ohio, USA, 1967
- [3] B. Terry and G. Jones, *Metal Matrix Composites - Current Developments and Future Trends in Industrial Research and Applications*, Elsevier Science Publishers Ltd., Oxford, England, 1990
- [4] M. J. Starink, *Precipitation Phenomena in Aluminium-Based Metal Matrix Composites: Effects of Reinforcement on Kinetics and Misfit Accommodation*, PhD Thesis T.U. Delft, 1992
- [5] T. W. Clyne and P. J. Withers, *An Introduction to Metal Matrix Composites*, Cambridge University Press, Cambridge, Great Britain, 1993
- [6] P. M. Mummery and B. Derby, 'The Influence of Microstructure on the Fracture Behaviour of Particulate Metal Matrix Composites', *Materials Science and Engineering*, **A135** (1991), pp. 221-224
- [7] S. V. Nair, J. K. Tien and R. C. Bates, 'SiC-Reinforced Aluminium Metal Matrix Composites', *International Metals Reviews*, **30** (1985), pp. 275-288
- [8] C. P. You, A. W. Thompson and I. M. Bernstein, 'Proposed Failure Mechanism in a Discontinuously Reinforced Aluminum Alloy'. *Scripta Metallurgica*, **21** (1987), pp. 181-185
- [9] B. Roebeck, 'Fractography of a SiC Particulate Reinforced Aluminium Metal Matrix Composite', *Journal of Material Science Letters*, **6** (1987), pp. 1138-1140
- [10] M. J. Hadianfard, J. C. Healy and Y. -W. Mai, 'Fracture Characteristics of a Particulate-Reinforced Metal Matrix Composite', *Journal of Materials Science*, **29** (1994), pp. 2321-2327
- [11] J. J. Lewandowski, C. Liu and W. H. Hunt, 'Effects of Matrix Microstructure and Particle Distribution on Fracture of an Al MMC', *Materials Science & Engineering*, **A107** (1989), pp. 241-255
- [12] A. Mortensen, *A Review of the Fracture Toughness of Particle Reinforced Aluminium Alloys*, ASM Conference Proceedings: Fabrication of Particulate Reinforced Metal Composites, Montreal, Canada, eds. J. Masounave and F. G. Hamel, 1990, pp. 217-233

- [13] T. J. A. Doel and P. Bowen, 'Effect of Particle Size and Matrix Aging Condition on Toughness of Particle Reinforced Aluminium Based Metal Matrix Composites', *Materials Science and Technology*, **12** (1996), pp. 586-594
- [14] Y. Marchal, F. Delannay and L. Froyen, 'The Essential Work of Fracture as a Means for Characterizing the Influence of Particle Size and Volume Fraction on the Fracture Toughness of Plates of Al/SiC Composites', *Scripta Materialia*, **35** (1996), pp. 193-198
- [15] J. R. Brockenbrough, S. Suresh and H. A. Wienecke, 'Deformation of Metal-Matrix Composites with Continuous Fibres: Geometrical Effects of Fiber Distribution and Shape', *Acta Metallurgica et Materialia*, **39** (1991), pp. 735-752
- [16] J. R. Brockenbrough and S. Suresh, 'Plastic Deformation of Continuous Fiber-Reinforced Metal-Matrix Composites: Effects of Fiber Shape and Distribution', *Scripta Metallurgica et Materialia*, **24** (1990), pp. 325-330
- [17] S. G. Song, N. Shi, G. T. Gray and J. A. Roberts, 'Reinforcement Shape Effects on the Fracture Behavior and Ductility of Particulate-Reinforced 6061-Al Matrix Composites', *Metallurgical and Materials Transactions A*, **27A** (1996), pp. 3739-3746
- [18] D. J. Lloyd, 'Aspects of Fracture in Particulate Reinforced Metal Matrix Composites', *Acta Metallurgica et Materialia*, **39** (1991), pp. 59-71
- [19] T. S. Srivatsan, 'Microstructure, Tensile Properties and Fracture Behaviour of Al₂O₃ Particulate-Reinforced Aluminium Alloy Metal Matrix Composites', *Journal of Materials Science*, **31** (1996), pp. 1375-1388
- [20] M. Manoharan and J. J. Lewandowski, 'In Situ Scanning Electron Microscope Studies of Crack Growth in an Aluminum Metal-Matrix Composite', *Scripta Metallurgica et Materialia*, **24** (1990), pp. 2357-2362
- [21] P. Poza and J. Llorca, 'Fracture Toughness and Fracture Mechanisms of Al-Al₂O₃ Composites at Cryogenic and Elevated Temperatures', *Materials Science and Engineering*, **A206** (1996), pp. 183-193
- [22] H. -J. Kim, H. Iwananri, E. -P. Yoon and T. Kobayashi, 'Effect of Particle Volume Fraction on Fracture of SiC/6061 Al Composites', *Journal of Materials Science Letters*, **11** (1992), pp. 950-952
- [23] J. E. King and D. Bhattacharjee, 'Interfacial Effects on Fatigue and Fracture in Discontinuously Reinforced Metal Matrix Composites', *Materials Science Forum*, **189-190** (1995), pp. 43-56
- [24] H. Ribes, R. Da Silva, M. Suéry and T. Bretheau, 'Effect of Interfacial Oxide Layer in Al-SiC Particle Composites on Bond Strength and Mechanical Behaviour', *Materials Science and Technology*, **6** (1990), pp. 621-628
- [25] Y. Flom and R. J. Arsenault, 'Deformation of SiC/Al Composites', *Journal of Metals*, **38** (1986), pp. 31-34
- [26] D. L. Davidson, 'Fracture Characteristics of Al-4 Pct Mg Mechanically Alloyed with SiC', *Metallurgical Transactions A*, **18A** (1987), pp. 2115-2128

References

- [27] M. Manoharan and J. J. Lewandowski, 'Crack Initiation and Growth Toughness of an Aluminum Metal-Matrix Composite', *Acta Metallurgica et Materialia*, **38** (1990), pp. 489-496
- [28] G. Liu, Z. Zhang and J. K. Shang, 'Interfacial Microstructure and Fracture of Al_2O_3 Particulate Reinforced Al-Cu Composite', *Acta Metallurgica et Materialia*, **42** (1994), pp. 271-282
- [29] T. Das, P. Munroe, S. Bandyopadhyay, T. Bell and M. V. Swain, 'Interfacial Behaviour of 6061/ Al_2O_3 Metal Matrix Composites' *Materials Science and Technology*, **13** (1997), pp. 778-784
- [30] H. J. Böhm, Lecture Notes, European Advanced Summer School, 'Frontiers for Computational Micromechanics in Industrial and Engineering Materials', National University of Ireland, Galway, Ireland, 1998
- [31] A. L. Gurson, 'Continuum Theory of Ductile Rupture by Void Nucleation and Growth: Part I - Yield Criteria and Flow Rules of Porous Ductile Media', *Journal of Engineering Materials and Technology*, Transactions of the ASME, (1977), pp. 2-15
- [32] V. Tvergaard, 'Influence of Voids on Shear Band Instabilities Under Plane Strain Conditions', *International Journal of Fracture*, **17** (1981), pp. 389-407
- [33] W. Brocks, D. -Z. Sun and A. Hönl, 'Verification of Micromechanical Models for Ductile Fracture by Cell Model Calculations', *Computational Materials Science*, **7** (1996), pp. 235-241
- [34] D. -Z. Sun, D. Siegele, B. Voss and W. Schmitt, 'Application of Local Damage Models to the Numerical Analysis of Ductile Rupture', *Fatigue and Fracture of Engineering Materials and Structures*, **12** (1989), pp. 201-212
- [35] R. W. J. Koers, A. H. M. Krom and A. Bakker, 'Prediction of Cleavage Fracture in the Brittle to Ductile Transition Region of a Ferritic Steel', in Constraint Effects in Fracture Theory and Applications: second volume, ASTM STP 1244, eds. M. Kirk and A. Bakker, American Society for Testing and Materials, Philadelphia, 1995, pp. 191-208
- [36] O. P. Sövik, 'The Effect of Non-Spherical Void Shape on the Evolution of Ductile Damage', Proceedings of the 11th Biennial European Conference on Fracture (ECF11 - Mechanisms and Mechanics of Damage and Failure (Poitiers-Futuroscope, France)), eds. J. Petit, J. de Fouquet, G. Henaff, P. Villechaise and A. Dragon, Emas Publishing, Cradley Heath, UK (1996), pp. 935-940
- [37] Z. L. Zhang and M. Hauge, 'Fitting the Gurson Parameters by using a Physical Void Coalescence Mechanism', Proceedings of the 11th Biennial European Conference on Fracture (ECF11 - Mechanisms and Mechanics of Damage and Failure (Poitiers-Futuroscope, France)), eds. J. Petit, J. de Fouquet, G. Henaff, P. Villechaise and A. Dragon, Emas Publishing, Cradley Heath, UK (1996), pp. 941-946
- [38] H. J. Rack and R. W. Krenzer, 'Thermomechanical Treatment of High Purity 6061 Aluminum', *Metallurgical Transactions*, **8A** (1977), pp. 335-345
- [39] J. M. Papazian, 'Effects of SiC Whiskers and Particles on Precipitation in Aluminum Matrix Composites', *Metallurgical Transactions*, **19A** (1988), pp. 2945-2953

- [40] A. K. Gupta and D. J. Lloyd, *The Precipitation in a Super Purity Al-Mg-Si Alloy*, The Third International Conference on Al Alloys, pp. 21-26
- [41] G. A. Edwards, K. Stiller, G. L. Dunlop and M. J. Couper, 'The Composition of Fine-Scale Precipitates in Al-Mg-Si Alloys', *Materials Science Forum*, **217-222** (1996), pp. 713-718
- [42] I. Dutta and S. M. Allen, 'A Calorimetric Study of Precipitation in Commercial Aluminium Alloy 6061', *Journal of Materials Science and Letters*, **10** (1991), pp. 323-326
- [43] M. S. Vossenbergh, 'A Differential Scanning Calorimetry Study on the Influence of Aging Treatments on the Precipitation Behaviour in Al-Mg-Si Alloys', Graduate Report, (1998), p. 4
- [44] F. W. Fifield and D. Kealey, *Principles and Practise of Analytical Chemistry*, 3rd Edition, Chapman & Hall, 1990, pp. 455-458
- [45] M. E. Brown and C. A. R. Phillpotts, 'Non-Isothermal Kinetics', *Journal of Chemical Education*, **55** (1978), pp. 556-560
- [46] J. M. Criado, M. González, A. Ortega and C. Real, 'Discrimination of the Kinetic Model of Overlapping Solid-State Reactions from Non-Isothermal Data', *Journal of Thermal Analysis*, **34** (1988), pp. 1387-1396
- [47] J. Zsakó, 'Remarks on "A New Equation for Modelling Nonisothermal Reactions"', *Journal of Thermal Analysis*, **34** (1988), pp. 1489-1494
- [48] I. N. A. Oguocha and S. Yannacopoulos, 'Precipitation and Dissolution Kinetics in Al-Cu-Mg-Fe-Ni Alloy 2618 and Al-Alumina Particle Metal Matrix Composite', *Materials Science and Engineering*, **A231** (1977), pp. 25-33
- [49] A. Luo, D. J. Lloyd, A. Gupta and W. V. Youdelis, 'Precipitation and Dissolution Kinetics in Al-Li-Cu-Mg Alloy 8090', *Acta Metallurgica et Materialia*, **41** (1993), pp. 769-776
- [50] E. J. Mittemeijer, L. Cheng, P. J. van der Schaaf, C. M. Brakman and B. M. Korevaar, 'Analysis of Nonisothermal Transformation Kinetics; Tempering of Iron-Carbon and Iron-Nitrogen Martensites', *Metallurgical Transactions*, **19A** (1988), pp. 925-931
- [51] E. J. Mittemeijer, *Journal of Materials Science*, 'Analysis of the Kinetics of Phase Transformations', **27** (1992), pp. 3977-3987
- [52] J. D. Bryant, *The Effects of Preaging Treatments on Formability and Paint Bake Response in Aluminium Autobody Sheet Alloys*, Automotive Alloys, eds. S. K. Das and G. J. Kipourous, The Minerals, Metals and Materials Society, London, 1997, pp. 19-36
- [53] D. Turnbull and R. L. Cormia, 'Kinetics of Later Stages of Clustering in Al-Cu Alloy', *Acta Metallurgica*, **8** (1960), pp. 747-750
- [54] M. Taya, K. E. Lulay and D. J. Lloyd, 'Strengthening of a Particulate Metal Matrix Composite by Quenching', *Acta Metallurgica et Materialia*, **39** (1991), pp. 73-87
- [55] I. Dutta and D. L. Bourell, 'Influence of Dislocation Density and Distribution on the Aging Behavior of 6061 Al-SiC_w Composites', *Acta Metallurgica et Materialia*, **38** (1990), pp. 2041-2049

References

- [56] S. K. Pabi, 'On the Dissolution Kinetics of Silicon in an Aluminium-rich Matrix', *Materials Science and Engineering*, **43** (1980), pp. 151-158
- [57] K. Matsuda, S. Tada, S. Ikeno, T. Sato and A. Kamio, 'Crystal Structure of β ' Phase in an Al-1.0 mass% Mg₂Si Alloy', The Fourth International Conference on Aluminum Alloys (ICAA4), eds. T. H. Sanders, Jr. and E. A. Starke, Jr., Atlanta, Georgia USA (1994), pp. 598-604
- [58] M. Takeda, F. Ohkubo, T. Shirai and F. Fukui, 'Precipitation Behaviour of Al-Mg-Si Ternary Alloys', *Materials Science Forum*, **217-222** (1996), pp. 815-820
- [59] B. Chalmers, *Progress in Materials Science Volume 10*, Pergamon Press Ltd., London, England, 1963, pp. 172-178
- [60] P. van Mourik, E. J. Mittemeijer and T. H. Keijser, 'On Precipitation in Rapidly Solidified Aluminium-Silicon Alloys', *Journal of Materials Science*, **18** (1983), pp. 2706-2712
- [61] J. M. Papazian, 'Calorimetric Studies of Precipitation and Dissolution Kinetics in Aluminum Alloys 2219 and 7075', *Metallurgical Transactions*, **13A** (1982), pp. 761-768
- [62] R. J. Arsenault and N. Shi, 'Dislocation Generation Due to Differences between the Coefficients of Thermal Expansion', *Materials Science and Engineering*, **81** (1986), pp. 175-187
- [63] I. Dutta, S. M. Allen and J. L. Hafley, 'Effect of Reinforcement on the Aging Response of Cast 6061 Al-Al₂O₃ Particulate Composites', *Metallurgical Transactions A*, **22A** (1991), pp. 2553-2563
- [64] T. Das, P. R. Munroe and S. Bandyopadhyay, 'The Effect of Al₂O₃ Particulates on the Precipitation Behaviour of 6061 Aluminium-Matrix Composites', *Journal of Materials Science*, **31** (1996), pp. 5351-5361
- [65] E. Söderlund, I. Reineck and D. J. Rowcliffe, 'Ultralow Load Indentation Hardness and Modulus of K- and α -Al₂O₃ CVD Coatings', *Journal of Materials Research*, **9** (1994), pp. 1683-1692
- [66] J. W. Leggoe, X. Z. Hu, M. V. Swain and M. B. Bush, 'An Ultra-Micro Indentation Investigation of Aspects of the Fracture Process in Particulate Reinforced Metal Matrix Composites', *Scripta Metallurgica & Materialia*, **31** (1994), pp. 577-582
- [67] S. P. Chen, K. M. Mussert and S. van der Zwaag, 'Precipitation Kinetics in Al6061 and in an Al6061-Alumina Particle Composite', *Journal of Materials Science*, **33** (1998), pp. 4477-4483
- [68] W. C. Oliver and G. M. Pharr, 'An Improved Technique for Determining Hardness and Elastic Modulus using Load and Displacement Sensing Indentation Experiments', *Journal of Materials Research*, **7** (1992), pp. 1564-1583
- [69] M. F. Doerner and W. D. Nix, 'A Method for Interpreting the Data from Depth-Sensing Indentation Instruments', *Journal of Materials Research*, **1** (1986), pp. 601-609

- [70] I. N. Sneddon, 'The Relation Between Load and Penetration in the Axisymmetric Boussinesq Problem for a Punch of Arbitrary Profile', *International Journal of Engineering Science*, **3** (1965), pp. 47-57
- [71] D. J. Lloyd, 'Particle Reinforced Aluminium and Magnesium Matrix Composites', *International Materials Reviews*, **39** (1994), pp. 1-23
- [72] I. A. Ibrahim, F. A. Mohamed and E. J. Lavernia, 'Particulate Reinforced Metal Matrix Composites - A Review', *Journal of Materials Science*, **26** (1991), pp. 1137-1156
- [73] J. S. Zhang, X. J. Liu, H. Cui, Z. Q. Sun and G. L. Chen, 'Nanoindentation Characterisation of the Properties around Reinforcements in a Heat Treated Spray Deposited 2014+15vol% SiC_p Metal-Matrix Composite', *Scripta Materialia*, **35** (1996), pp. 1115-1120
- [74] J. R. Davis, *ASM Specialty Handbook, Aluminum and Aluminum Alloys*, ASM International, pp. 685-686
- [75] *Duralcan Composites for Wrought Products: Mechanical and Physical Property Data*, Duralcan USA
- [76] A. H. C. Duwel, 'Determination of Fracture Toughness versus Volume Fraction Behaviour in an Aluminium Metal Matrix Composite', Graduate Report, (2000), p. 35-38, 65-80
- [77] ASTM E8M-94a, *Standard Test Methods for Tension Testing of Metallic Materials [Metric]*, Annual Book of ASTM Standards, 1994, pp. 81-100
- [78] H. L. Ewalds and R. J. H. Wanhill, *Fracture Mechanics*, Delftse Uitgevers Maatschappij, Delft, The Netherlands, 1993
- [79] P. C. H. Ament, *Corrosion Fatigue of Structural Steel in Sea Water*, PhD Thesis T.U. Delft, 1998
- [80] J. R. Rice, 'A Path Independent Integral and the Approximate Analysis of Strain Concentration by Notches and Cracks', *Journal of Applied Mechanics*, **35** (1968), pp. 379-386
- [81] A. Bakker, *The Three-Dimensional J-Integral, An Investigation into Its Use for Post-Yield Fracture Safety Assessment*, PhD Thesis Technische Hogeschool Delft, 1984
- [82] G. R. Irwin, 'Analysis of Stresses and Strains near the End of a Crack Traversing a Plate', *Journal of Applied Mechanics*, **24** (1957), pp. 361-364
- [83] ASTM E399-90, *Standard Test Method for Plane Strain Fracture Toughness of Metallic Materials*, Annual Book of ASTM Standards, 1994, pp. 407-437
- [84] ASTM E1737-96, *Standard Test Method for J-Integral Characterization of Fracture Toughness*, Annual Book of ASTM Standards, 1997, pp. 968-991
- [85] D. A. Jablonski, B. Journet, R. S. Vecchio and R. Hertzberg, 'Compliance Functions for Various Fracture Mechanics Specimens', *Engineering Fracture Mechanics*, **22** (1985), pp. 819-823

References

- [86] H. S. Reemsnyder, H. G. Pisarki and M. G. Dawes, 'Residual Stresses and Fatigue Precracking Techniques for Weldment Fracture Toughness Specimen', *Journal of Testing and Evaluation*, **20** (1992), pp. 416-423
- [87] F. G. Nelson, P. E. Schilling and J. G. Kaufman, 'The Effect of Specimen Size on the Results of Plane-Strain Fracture-Toughness Tests', *Engineering Fracture Mechanics*, **4** (1972), pp. 33-50
- [83] F. G. Nelson and J. G. Kaufman, 'Fracture Toughness of Plain and Welded 3-In.-Thick Aluminum Alloy Plate', in *Progress in Flaw Growth and Fracture Toughness Testing*, ASTM STP 536, American Society for Testing and Materials, 1973, pp. 350-376
- [89] F. G. Nelson and D. J. Brownhill, 'Fracture Characteristics of Plain and Welded 3-In.-Thick Aluminum Alloy Plate at Various Temperatures', in *Flaw Growth and Fracture*, ASTM STP 631, American Society for Testing and Materials, 1977, pp. 285-309
- [90] B. Roebuck and L. D. Lord, 'Plane Strain Fracture Toughness Test Procedure for Particulate Metal Matrix Composites', *Materials Science and Technology*, **6** (1990), pp. 1199-1209
- [91] M. J. Hadianfard, G. Heness, J. C. Healy and Y. -W. Mai, 'Fracture Toughness Measurements and Failure Mechanisms of Metal Matrix Composites', *Fatigue & Fracture of Engineering Materials and Structures*, **17** (1994), pp. 253-263
- [92] M. J. Hadianfard, J. C. Healy and Y. -W. Mai, *The Influence of Heat Treatment on Mechanical and Fracture Properties of an Alumina Microsphere Reinforced Aluminium Matrix Composite*, International Conference on Advanced Composite Materials, eds. T. Chandra and A. K. Dhingra, 1993, pp. 1199-1204
- [93] T. F. Klimowicz and K. S. Vecchio, *The Influence of Aging on the Fracture Toughness of Alumina-Reinforced Aluminum Composites*, Fundamental Relationships between Microstructure and Mechanical Properties of MMCs, TMS, eds. P. K. Liaw and M. N. Gungor, 1990, pp. 255-267
- [94] ASTM E1290 - 93, *Standard Test Method for Crack-Tip Opening Displacement (CTOD) Fracture Toughness Measurement*, Annual Book of ASTM Standards, 1997, pp. 828-837
- [95] ASTM E1820-96, *Standard Test Method for Measurement of Fracture Toughness*, Annual Book of ASTM Standards, 1997, pp. 992-1024
- [96] J. G. Kaufman, 'Experience in Plane-Strain Fracture Toughness Testing per ASTM E399', in *Developments in Fracture Mechanics Test Methods Standardization*, ASTM STP 632, eds. W. F. Brown, Jr. and J. G. Kaufman, American Society for Testing and Materials, 1977, pp. 3-24
- [97] G. J. Petrak, 'A Note on Fatigue Crack Front Straightness in K_{Ic} Testing', *Engineering Fracture Mechanics*, **4** (1972), pp. 311-313
- [98] G. T. Hahn and A. R. Rosenfield, 'Metallurgical Factors Affecting Fracture Toughness of Al Alloys', *Metallurgical Transactions*, **6A** (1975), pp. 653-670
- [99] R. W. Hertzberg, *Deformation and Fracture Mechanics of Engineering Materials*, John Wiley & Sons, Inc., United States of America, 1989

- [100] Y. Brechet, J. D. Embury, S. Tao and L. Luo, 'Damage Initiation in Metal Matrix Composite', *Acta Metallurgica et Materialia*, **39** (1991), pp. 1781-1786
- [101] T. Mochida, M. Taya and D. J. Lloyd, 'Fracture of Particles in a Particle/Metal Matrix Composite under Plastic Straining and its Effect on the Young's Modulus of the Composite', *Materials Transactions, JIM*, **32** (1991), pp. 931-942
- [102] J. Llorca, A. Martín, J. Ruiz and M. Elices, 'Particulate Fracture during Deformation of a Spray Formed Metal-Matrix Composite', *Metallurgical Transactions A*, **24A** (1993), pp. 1575-1588
- [103] J. Koplik and A. Needleman, 'Void Growth and Coalescence in Porous Plastic Solids', *International Journal of Solids and Structures*, **24** (1988), pp. 835-853
- [104] V. Tvergaard, 'On Localization in Ductile Materials Containing Spherical Voids', *International Journal of Fracture*, **18** (1982), pp. 237-252
- [105] W. Weibull, 'A Statistical Distribution Function of Wide Applicability', *Journal of Applied Mechanics*, **18** (1951), pp. 293-297
- [106] G. Weaver, 'Engineering with Ceramics Part 1. The Weibull Model', *Journal of Materials Education*, 1983, pp. 768-804
- [107] C. A. Lewis and P. J. Withers, 'Weibull Modelling of Particle Cracking in Metal Matrix Composites', *Acta Metallurgica et Materialia*, **43** (1995), pp. 3685-3699
- [108] J. Llorca, 'An Analysis of the Influence of Reinforcement Fracture on the Strength of Discontinuously-Reinforced Metal-Matrix Composite', *Acta Metallurgica et Materialia*, **43** (1995), pp. 181-192
- [109] Metals Handbook, 9th edition, American Society for Metals, Metals Park, Ohio, **8**, 1985, pp. 555
- [110] MARC K7, MARC Analysis Research Corporation, Palo Alto, USA (1997)
- [111] V. Tvergaard and A. Needleman, 'Analysis of the Cup-cone Fracture in a Round Tensile Bar', *Acta Metallurgica*, **32** (1984), pp. 157-169
- [112] R. M. McMeeking, 'Finite Deformation Analysis of Crack-tip Opening in Elastic-Plastic Materials and Implications for Fracture', *Journal of the Mechanics and Physics of Solids*, **25** (1977), pp. 357-381.
- [113] J. R. Rice and M. A. Johnson, 'The Role of Large Crack Tip Geometry Changes in Plane Strain Fracture', in *Inelastic Behaviour of Solids*, eds. M. F. Kanninen *et al.* McGraw-Hill, New York, 1970, pp. 641-672
- [114] Z. P. Bazant, T. P. Belytschko and T. P. Chang, 'Continuum Theory for Strain Softening', *Journal of the Engineering Mechanics Division*, **110** (1984), pp. 1666-1692
- [115] J. B. Leblond, G. Perrin and J. Devaux, 'Bifurcation Effects in Ductile Metals with Damage Localization', *Journal of Applied Mechanics*, **61** (1994), PP. 236-242
- [116] V. Tvergaard and A. Needleman, 'Effects of Nonlocal Damage in Porous Plastic Solids', *International Journal of Solids and Structures*, **32** (1995), pp. 1063-1077
- [117] V. Tvergaard and A. Needleman, 'Nonlocal Effects on Localization in a Void-Sheet', *International Journal of Solids and Structures*, **34** (1997), pp. 2221-2238

References

- [118] D. -Z. Sun, W. Brocks and W. Schmitt, 'Fracture Toughness Evaluation by Tensile and Charpy-Type Tests Based on Micromechanical Models of Materials', *Materials Science*, **30** (1994), pp. 223-229
- [119] K. C. Koppenhoefer and R. H. Dodds, 'Ductile Crack Growth in Pre-Cracked CVN Specimens: Numerical Studies', *Nuclear Engineering and Design*, **180** (1998), pp. 221-241
- [120] Z. L. Zhang, 'A Sensitivity Analysis of Material Parameters for the Gurson Constitutive Model', *Fatigue & Fracture of Engineering Materials & Structures*, **19** (1996), pp. 561-570
- [121] D. Steglich and W. Brocks, 'Micromechanical Modelling of the Behaviour of Ductile Materials Including Particles', *Computational Materials Science*, **9** (1997), pp. 7-17
- [122] D. Steglich, T. Siegmund and W. Brocks, 'Micromechanical Modeling of Damage due to Particle Cracking in Reinforced Metals', *Computational Materials Science*, **16** (1999), pp. 404-413
- [123] D. Steglich, *Bestimmung von mikrostrukturellen Parametern in Schädigungsmodellen für duktile Metalle*, Dissertation der Technischen Universität Berlin, 1999

SUMMARY

Aluminium alloys possess advantages such as a low density in combination with an adequate stiffness, strength and ductility and excellent corrosion resistance, but these alloys also have some intrinsic disadvantages like a rather low stiffness of 69 GPa, a moderate wear resistance and a poor high temperature performance. Aiming at even better materials, it is desirable to improve the mechanical properties of current aluminium alloys.

The development of metal matrix composites (MMCs) is one of the last few decades and aims at the production of such improved materials when compared with current unreinforced aluminium alloys, *i.e.* an improvement of stiffness, wear resistance and high temperature performance. In general, MMCs consist of ceramic particles embedded in an aluminium matrix, whereby the reinforcement can be continuous in the form of fibres, or discontinuous in the form of whiskers or particles. Aluminium and its alloys are the most widely applied metals as matrix material for MMCs, since their ductility, formability and low density can be combined with the stiffness and load-bearing capacity of the reinforcement used.

The subject of this thesis is the investigation of the fracture mechanical behaviour of MMCs based on the heat treatable AA6061 aluminium alloy, which contains both Mg and Si, reinforced with Al_2O_3 particles. This is done both experimentally using a range of techniques, as well as numerically using finite element models, whereby the experimentally obtained results are implemented in finite element models to simulate the mechanical behaviour. Since experiments as well as calculations are performed to achieve this aim, this thesis is arranged in two parts, namely part A, an experimental part devoted to material behaviour and part B, a theoretical part on modelling fracture mechanical behaviour.

Two MMC grades are investigated. The first is a commercial MMC consisting of AA6061 reinforced with 20 vol.% Al_2O_3 in different heat treatment conditions. This material is produced industrially via the stir casting process, whereby the reinforcing powder is added and mixed into the molten matrix through melt agitation by a stirrer. After stir casting, the material is extruded into a rod. The second MMC grade investigated is an experimentally produced MMC, which is given a fixed T6 heat treatment after production. This MMC is tested for four different reinforcement volume fractions, namely 7, 10, 14 or 22 vol.% Al_2O_3 particles and is produced by means of powder metallurgy. Production of each sample consists of powder mixing, powder cold compaction and powder hot compaction/sintering. Differences in particle sizes between AA6061 and Al_2O_3 powder turn out to complicate the production of a microstructure comparable to the microstructure of the commercial MMC, *i.e.* the experimental MMC results in an inverse microstructure whereby aluminium grains are embedded in an MMC network. Since this network phase is fully wetted with aluminium, a good bonding is expected all the same.

Since the matrix of the MMCs investigated is of the precipitation hardenable type, it responds to a solutionize-quench-age treatment. It has been reported that an increase in strength in an AA6061 alloy due to age hardening is positively affected by the introduction of reinforcing ceramic particles [38, 39]. As the reinforcements are thought not to affect the overall chemistry of the matrix, this effect must be due to a stimulated precipitation response of the matrix. The nature of this stimulated precipitation is not easy to predict, in particular not for AA6xxx-based alloys containing both Mg and Si where even for the unreinforced base material the exact order of the various precipitation reactions is subject of debate [39-42]. Therefore, the commercial MMC is investigated using the differential scanning calorimetry (DSC) technique, to examine the MMC matrix response to heat treating compared with that of an unreinforced AA6061 alloy. Based on this investigation, which is described in part A, chapter 2, the following precipitation sequence is found for both the AA6061 reference alloy and the 20 vol.% Al₂O₃/AA6061 MMC:

- (i) vacancy related clusters,
- (ii) competitive formation of GP-I and GP-II (β'') zones,
- (iii) precipitation of the β' phase, and
- (iv) formation of the β -Mg₂Si phase

Furthermore, the addition of Al₂O₃ particles reduces the amount of peaks formed at steps (i) and (iii) in AA6061 and shifts the peak temperatures to lower temperatures. Another result of the addition of Al₂O₃ particles to an AA6061 matrix is that these particles promote the formation of the β'' phase. This phase contributes to the strengthening and will increase the strength of the composite.

A considerable contribution to the macroscopic mechanical properties is due to the behaviour of the particle/matrix interface and is certainly not only determined by the mechanical properties of the various constituents of an MMC. Some investigators have found that, as result of a heat treatment, the matrix regions adjacent to the reinforcement may exhibit a higher dislocation density when compared with matrix material further away from the interface due to mismatch of the coefficients of thermal expansion (CTE) between the matrix and the ceramic reinforcements. These CTE-dislocation effects influence the kinetics of precipitation [62-64] and in case of an AA6061-based MMC may even result in a layer of matrix material around the particles with a high hardness [29].

Since the width of particle/matrix interfaces and the interparticle distances are of the order of micrometers, it is practically not possible to determine gradients in mechanical properties around the particles using conventional techniques. However, nanoindentation which measures the resistance to plastic deformation in very small volumes, may offer some indication of the presence of gradients in mechanical behaviour on the micrometer range.

In part A, chapter 3, nanoindentation testing is used to measure and calculate the hardness and elastic modulus profiles of AA6061 reinforced with Al₂O₃ in three different heat treatment conditions. Results are compared with nanoindentation measurements on unreinforced AA6061 in the same three heat treatment conditions, to investigate possible changes in the mechanical behaviour of the matrix material due to the presence of the ceramic reinforcement. The hardness and elastic modulus of matrix and particles can indeed be determined with this technique, but the values obtained may only be used for relative comparison. Like Das *et al.* [29], Mg enrichment around the ceramic particles is observed in this investigation, but

measurement of the hardness and elastic modulus of this interfacial layer is not possible. The limited width of the Mg-rich zone of approximately 4 μm explains the absence of indentations in this layer in this investigation, but also raises serious questions about the correctness of the indentations done by Das *et al.*

When comparing nanoindentation results of AA6061 reference material with the behaviour of an AA6061 matrix in an MMC in three different heat treatment conditions, it turns out that there are hardly any differences in calculated elastic moduli and hardness values. So, when modelling the mechanical behaviour of MMCs using the finite element method it is permissible to assume the MMC matrix behaving similar as the same aluminium alloy without ceramic reinforcements.

The greater part of the experimental work done in this investigation, which is presented and discussed in part A, chapter 4, involves the fracture mechanical experiments. In this chapter, the fracture mechanical behaviour of the precipitation hardening aluminium alloy AA6061 and of both AA6061-based MMCs is being investigated using both tensile and fracture toughness experiments.

Tensile tests, in which the material properties such as the elastic modulus, the yield strength, the ultimate tensile strain and the hardening exponent are determined are only performed on unreinforced AA6061 material, since it turns out to be impossible to machine the MMCs into suitable tensile specimens. The fracture toughness experiments on the other hand, are performed on the unreinforced AA6061 alloy, serving as reference material for the matrix of the MMCs, on the commercial MMC and on the experimentally manufactured MMCs. The commercial MMC is tested in various heat treatment conditions, whereas the experimental MMCs are tested in T6 condition with various volume fractions of Al_2O_3 particles.

To determine the fracture toughness, the disk-shaped compact tension specimen geometry is selected since machining of this specimen geometry involves few steps. For the stress intensity analysis to be valid, an ideal planar crack with essentially zero crack tip radius needs to be created. The standard way to obtain such a crack is to fatigue load a specimen until a crack of the desired length has grown. In MMC material the growing crack turns out to be invisible due to unavoidable surface roughness. Therefore, the crack length is measured using the compliance method. Two different ASTM standards are used, namely ASTM E399 [83] and ASTM E1737 [84]. The ASTM E399 standard provides regulations to obtain plane strain fracture toughness values for metallic materials and ASTM E1737 covers the determination of fracture toughness as characterised by the J-integral for ductile materials that lack sufficient size and thickness or that are too ductile to be tested for fracture toughness in accordance with the requirements of ASTM E399.

It is concluded from the tensile tests, that different heat treatments which lead to predominantly β'' (condition B), predominantly β' (condition C) or a mixture of these precipitates (conditions T6 or T651), lead to large differences in yield strength in the unreinforced AA6061, *i.e.* the yield strength of the AA6061 alloy in condition C is about 30% lower than in the other two conditions.

Critical evaluation of all the requirements for valid fracture toughness values shows that many of the literature data for unreinforced AA6061, including our own, are invalid. The same can be concluded for the MMCs tested, *i.e.* only one specimen tested according to ASTM E399 is a valid fracture toughness value. Since most fracture toughness values just fail some

requirements some comparison can still be made. It is found that the fracture toughness of the commercial MMC is around $21 \text{ MPa}\sqrt{\text{m}}$ in heat treatment conditions B and C, which is only moderately lower than the fracture toughness values of the AA6061 alloy found in literature, which is on average $27 \text{ MPa}\sqrt{\text{m}}$. Since the measured fracture toughness values of the conditions B and C are similar, the fracture toughness of this MMC seems to be independent of the heat treatments as they are imposed in this investigation.

The fracture toughness of the experimental MMCs, which are reinforced with various volume fractions ceramic particles, is evaluated using different procedures, namely the ASTM E399 and the ASTM E1737 method. Using the ASTM E1737 method, an obvious trend for the variation of fracture toughness with volume fraction reinforcing Al_2O_3 particles can be predicted, whereas the ASTM E399 method can not.

The trend observed for the experimental MMCs is an approximately linearly decrease of the fracture toughness with increasing volume percentages of Al_2O_3 particles.

In part B, chapter 5, fracture in an AA6061-based MMC containing 20 vol.% Al_2O_3 particles is modelled using an axisymmetrical finite element model and a statistical approach for calculating the strength of reinforcing ceramic particles via the Weibull model [105]. Within this model, variables such as loading triaxiality, particle size and matrix alloy properties are varied to investigate the parameter dependence of particle fracture. When modelling the fracture behaviour of one particle, it is assumed that the survival probability of the ceramic particle is governed by a Weibull distribution. Fracture statistics of the MMC is examined by plotting the survival probability of an Al_2O_3 particle versus the macroscopic axial stress applied on the whole MMC.

Based on the calculations done, it can be concluded that the relation between the macroscopic applied stress on an MMC and the survival probability of a ceramic particle can be described by the Weibull modulus, as long as the stress distribution in the matrix surrounding that particle is proportional to the applied load. Furthermore, loading an MMC triaxially instead of uniaxially, results in a lower survival probability of the Al_2O_3 particle and the particle is likely to fail before plastic deformation in the matrix occurs.

When plotting the survival probability as a function of the macroscopic axial stress, this should result in a straight line with a gradient represented by the Weibull modulus. Considering the parameter dependence of particle fracture, it can be concluded that for the same loading ratio, an increase in the hardening exponent of the matrix, results in coinciding calculations for triaxial calculations, but uniaxial calculations coincide up to a point where curvature (a deviation) of the straight line starts. Furthermore, a variation of the characteristic stress (σ_0 in the Weibull model) results in a parallel shift of the curves for both triaxial and uniaxial calculations. For a fixed value of the hardening exponent, a 'mastercurve' can be made independent of characteristic stresses and matrix yield stresses and an increase of particle diameter (and thus volume of the ceramic particle) decreases the survival probability of an Al_2O_3 particle in an AA6061 aluminium matrix.

In ductile metals, voids mainly nucleate during plastic deformation, when second phase particles crack or debond from the surrounding matrix, and final fracture involves the growth of neighbouring voids to coalescence. This concept is applied to MMCs in part B, chapter 6, whereby the reinforcing particles act as nucleation sites for voids, either by decohesion of the

particle/matrix interface or by particle fracture. The model proposed by Gurson [31] is used in a form modified by Tvergaard and Needleman [111] to simulate the fracture mechanical behaviour of MMCs and to predict the fracture toughness as a function of heat treatment and various volume fractions reinforcing particles. The analysis in this chapter relies on the simplifying assumption that all voids are initially present in the material due to premature fracture of the ceramic particles.

The assumption that all particles in front of the crack tip are broken, is justified by the fact that the fracture process takes place in the direct vicinity of the crack tip, where the triaxiality is high. The model is tested on disk-shaped compact tension specimens. Modelling the fracture behaviour of experimental MMC, of which the production and fracture toughness is discussed in chapter 4, is not possible because the Gurson model can not handle the extremely high void volume fractions resulting from fracture of the ceramic particles as found in the MMC network of this material.

Numerical predictions indicate that no significant influence of the applied heat treatment conditions on the fracture toughness of the commercial MMC is to be expected. This effect is supported by experimental results. The Gurson model which in this numerical research is applied as a local model with a fixed sized element mesh turns out to be unfit for calculating the damage evolution in MMCs properly, *i.e.* the predicted fracture toughness values are all rather low values. With increasing element sizes, a shift to higher critical stress intensity values is observed, but still the values are too low. Calculations on MMCs containing 20 or 30 vol.% ceramic particles using the Gurson model result in a converged solution and show a trend similar to the trend found experimentally, *i.e.* a decrease in fracture toughness with increasing volume fraction reinforcing particles.

Overall, it can be concluded that with the use of the differential scanning calorimetry technique, the nanoindentation technique and the fracture toughness measurements it is possible to map out the (fracture) mechanical behaviour of AA6061-based MMCs reinforced with Al_2O_3 particles and to put the obtained results in perspective against a multitude of contradictory results reported in literature. As far as the finite element calculations are concerned, it is possible to investigate the influence of various variables such as the reinforcing particle size, the reinforcement volume fraction and the matrix ageing condition in isolation. Furthermore, an attempt is made to predict the fracture toughness of MMCs as a function of heat treatment condition and volume fraction reinforcing particles.

SAMENVATTING

Aluminium legeringen hebben voordelen zoals een lage dichtheid in combinatie met een redelijke stijfheid, sterkte en taaiheid en een uitstekende corrosie weerstand, maar deze legeringen hebben ook enige intrinsieke nadelen zoals een tamelijk lage stijfheid van 69 GPa, een matige slijtage weerstand en een slecht gedrag bij hoge temperaturen. Strevend naar betere materialen, is het wenselijk om de mechanische eigenschappen van huidige aluminium legeringen te verbeteren.

Een ontwikkeling van de afgelopen 20 jaar is die van metaal matrix composieten (MMC's). In vergelijking met huidige niet versterkte aluminium legeringen, richt onderzoek zich hier voornamelijk op de productie van deze materialen, dat wil zeggen gericht op een verbeterde stijfheid, slijtage weerstand en gedrag bij hoge temperaturen. Over het algemeen bestaan MMC's uit een aluminium matrix met daarin ingebed keramische deeltjes, waarbij de versterking onafgebroken kan zijn in de vorm van vezels, of onderbroken in de vorm van staafjes of deeltjes. Aluminium en aluminium legeringen zijn de meest toegepaste metalen als matrix materiaal voor MMC's, omdat de taaiheid, vervormbaarheid en lage dichtheid gecombineerd kunnen worden met de stijfheid en het belasting-dragend vermogen van de toegepaste versterking.

Het onderwerp van dit proefschrift is het onderzoek naar het breukmechanisch gedrag van MMC's welke gebaseerd zijn op de warmtebehandelbare AA6061 aluminium legering, welke zowel Mg als Si bevat, versterkt met Al_2O_3 deeltjes. Dit gedrag is zowel experimenteel onderzocht met behulp van verscheidene technieken, als numeriek met behulp van eindige elementen modellen, waarbij de experimenteel verkregen resultaten in de eindige elementen modellen gebruikt zijn om het mechanisch gedrag te simuleren. Aangezien er zowel experimenteel als numeriek onderzoek is verricht, is dit proefschrift verdeeld in twee delen, namelijk deel A, een experimenteel deel gewijd aan materiaal gedrag en deel B, een theoretisch deel over modelleren van breukmechanisch gedrag.

Twee MMC soorten zijn onderzocht. De eerste was een commercieel MMC bestaande uit AA6061 versterkt met 20 vol.% Al_2O_3 in verschillende warmtebehandeling condities. Dit betrof een industrieel geproduceerd materiaal via een geroerd gietproces. Hierbij werd het versterkende poeder aan gesmolten matrix materiaal toegevoegd en gemixt met behulp van een roerder. Na het gieten werd het materiaal tot een staaf geëxtrudeerd. De tweede onderzochte MMC soort betrof een experimenteel geproduceerd MMC, welke na productie een T6 warmtebehandeling onderging. Dit MMC is getest met vier verschillende volume fracties versterkende deeltjes, namelijk 7, 10, 14 of 22 vol.% Al_2O_3 deeltjes en is met behulp van poeder metallurgie geproduceerd. Productie van elk proefstuk bestaat uit het mixen van de poeders, het koud compacteren van de poeders, gevolgd door het heet compacteren van de poeders, ook wel sinteren genoemd. Het is gebleken, dat verschillen in deeltjesgrootte tussen AA6061 en Al_2O_3 poeder de productie van een microstructuur vergelijkbaar aan die van het

commerciële MMC bemoeilijkt, dat wil zeggen dat het experimentele MMC resulteert in een inverse microstructuur waarbij aluminium korrels omgeven zijn door een MMC netwerk. Omdat deze netwerk fase volledig bevochtigd is met aluminium, is toch een goede binding verondersteld.

Aangezien de matrix van de onderzochte MMC's van een precipitatie hardende soort is, is deze gevoelig voor een oplos-afschrik-verouderings warmtebehandeling. Uit de literatuur blijkt, dat een sterkte-toename in een AA6061 legering als gevolg van veroudering positief beïnvloed wordt door de toevoeging van verstevigende keramische deeltjes [38, 39]. Er wordt aangenomen dat de verstevigende deeltjes niet de algehele chemische samenstelling van de matrix beïnvloeden, dus het effect moet het gevolg zijn van een gestimuleerd precipitatie gedrag van de matrix. De aard van dit gestimuleerde precipitatie gedrag is niet eenvoudig te voorspellen, in het bijzonder niet voor op AA6xxx gebaseerde legeringen die zowel Mg als Si bevatten waar zelfs voor het onverstevigde basis materiaal de exacte volgorde van de verschillende precipitatie reacties onderwerp van discussie is [39-42].

Daarom is het commerciële MMC onderzocht met behulp van de differentiële scanning calorimetrie (DSC) techniek, om het precipitatie gedrag van de MMC matrix te vergelijken met dat van een niet verstevigde AA6061 legering. Gebaseerd op dit onderzoek, welke is beschreven in deel A, hoofdstuk 2, is de volgende precipitatie volgorde gevonden voor zowel de AA6061 referentie legering en het 20 vol.% Al_2O_3 /AA6061 MMC:

- (v) clusters gerelateerd aan vacatures,
- (vi) competitieve vorming van GP-I en GP-II (β'') zones,
- (vii) precipitatie van de β' phase, en
- (viii) vorming van de β - Mg_2Si phase

Verder is gebleken, dat de toevoeging van Al_2O_3 deeltjes de grootte van de pieken gevormd bij de stappen (i) en (iii) in AA6061 reduceert en de piektemperaturen naar lagere temperaturen verschuiven. Een ander gevolg van het toevoegen van Al_2O_3 deeltjes aan een AA6061 matrix is, dat deze deeltjes de vorming van de β'' fase bevordert. Deze fase draagt bij aan de versterking en zal de sterkte van het composiet verhogen.

Een aanzienlijke bijdrage aan de macroscopische mechanische eigenschappen is te danken aan het gedrag van het contactvlak tussen deeltje en matrix en wordt zeker niet alleen bepaald door de mechanische eigenschappen van de verschillende bestanddelen van een MMC. Sommige onderzoekers hebben gevonden dat, als gevolg van een warmtebehandeling, matrix gebieden aansluitend aan een verstevigend deeltje een hogere dislocatie-dichtheid hebben vergeleken met matrix materiaal verder weg van het contactvlak als gevolg van het niet bij elkaar passen van de thermische uitzettingscoëfficiënten van de matrix en de keramische verstevigingen. Deze effecten beïnvloeden de precipitatie kinetiek [62-64] en in het geval van een op aluminium gebaseerd MMC zou het zelfs kunnen leiden tot een laag van matrix materiaal om de deeltjes met een hoge hardheid [29].

Omdat de breedte van de contactvlakken tussen deeltje en matrix en de onderlinge deeltjesafstanden van de orde van micrometers zijn, is het praktisch niet mogelijk om gradiënten in mechanische eigenschappen rond de deeltjes te bepalen met conventionele technieken. Echter, nano-indentatie waarbij de weerstand tegen plastische deformatie in zeer

kleine volumes gemeten wordt, zou wellicht enige indicatie van de aanwezigheid van gradiënten in mechanisch gedrag op een micrometer schaal kunnen aantonen.

In deel A, hoofdstuk 3, is de nano-indentatie techniek toegepast om de hardheid en elasticiteits modulus profielen van AA6061 verstevigd met Al_2O_3 in drie verschillende warmtebehandelings condities te meten en te berekenen. De resultaten zijn vergeleken met nano-indentatie metingen aan niet verstevigd AA6061 in dezelfde drie warmtebehandelings condities, om mogelijke veranderingen in het mechanisch gedrag van het matrix materiaal als gevolg van de aanwezigheid van een keramische versteviging te onderzoeken. De hardheid en elasticiteits modulus van matrix en deeltjes kunnen inderdaad bepaald worden met deze techniek, maar de gevonden waarden kunnen alleen gebruikt worden voor een relatieve vergelijking. Net als bij Das *et al.* [29], is er in dit onderzoek Mg-verrijking rond de keramische deeltjes waargenomen, maar meting van de hardheid en de elasticiteits modulus van deze laag is niet mogelijk. De beperkte breedte van de Mg-verrijkte zone van ongeveer 4 μm verklaart de afwezigheid van indentaties in deze laag in dit onderzoek, maar roept tevens vragen op bij de juistheid van de metingen die door Das *et al.* gedaan zijn.

Wanneer men de nano-indentatie resultaten van het AA6061 referentie materiaal vergelijkt met die van het AA6061 matrix materiaal van een MMC in drie verschillende warmtebehandelings condities, blijkt dat er nagenoeg geen verschillen zijn in berekende elasticiteits moduli en hardheid waarden. Derhalve is het geoorloofd om aan te nemen dat een MMC matrix hetzelfde gedrag vertoont als dezelfde aluminium legering zonder keramische versteviging, wanneer met behulp van de eindige elementen methode het mechanisch gedrag van MMC's gemodelleerd wordt.

Het grootste deel van het experimentele werk dat gedaan is in dit onderzoek, hetgeen beschreven staat in deel A, hoofdstuk 4, betreft de breukmechanische experimenten. In dit hoofdstuk, is het breukmechanisch gedrag van de precipitatie hardende aluminium legering AA6061 en van beide op AA6061 gebaseerde MMC's onderzocht met zowel trekproeven als breuktaaiheids experimenten.

Trekproeven, waarmee materiaal eigenschappen zoals de elasticiteits modulus, de vloeispanning, de uiterste rek en de verstevigings exponent bepaald worden, zijn alleen gedaan aan het niet verstevigde AA6061 materiaal, omdat het niet mogelijk is om van de MMC's geschikte trekstaafjes te vervaardigen. De breuktaaiheids experimenten daarentegen, zijn gedaan aan de niet verstevigde AA6061 legering, welke als referentie materiaal voor de matrix van de MMC's dient, aan het commerciële MMC en aan de experimenteel vervaardigde MMC's. Het commerciële MMC is getest in verschillende warmtebehandelings condities, terwijl de experimentele MMC's getest zijn in T6 conditie met verschillende volume fracties Al_2O_3 deeltjes.

Om de breuktaaiheid te bepalen, is gekozen voor de disk-shaped compact tension geometrie, omdat vervaardiging van deze proefstuk geometrie de minste stappen inhoudt. Om ervoor te zorgen dat de spanningsintensiteits analyse geldig is, dient er een ideale vlakke scheur met een scheurtip radius van nagenoeg nul gemaakt te worden. Een standaard manier om zo'n scheur te verkrijgen is, om het proefstuk te vermoeien tot een scheur met de gewenste lengte gegroeid is. In MMC materiaal blijkt een groeiende scheur onzichtbaar te zijn als gevolg van oppervlakte ruwheid. Daarom is de scheurlengte gemeten met behulp van de compliantie methode. Twee verschillende ASTM standaards zijn gebruikt, namelijk ASTM E399 [83] en

ASTM E1737 [84]. De ASTM E399 standaard schrijft voorwaarden voor om plane strain breuktaaiheids waarden voor metallische materialen te bepalen en ASTM E1737 houdt de bepaling van de breuktaaiheid in, gekenmerkt door de J-integraal en is geschikt voor taaie materialen die niet voldoende groot en dik zijn of welke te taai zijn om getest te worden in overeenstemming met de eisen van ASTM E399.

Uit de trekproeven kan geconcludeerd worden, dat verschillende warmtebehandelingen, welke leidden to voornamelijk β'' (conditie B), voornamelijk β' (conditie C) of een mengsel van deze precipitaten (condities T6 of T651), resulteren in grote verschillen in vloeispanning in het niet versterkte AA6061, dat wil zeggen dat de vloeispanning van de AA6061 legering in conditie C ongeveer 30% lager is dan in de andere twee condities.

Een kritische evaluatie van alle eisen voor een geldige breuktaaiheid, toont aan dat veel data uit de literatuur voor niet versterkt AA6061, maar ook onze data, ongeldig zijn. Het zelfde kan geconcludeerd worden voor de onderzochte MMC's, dat wil zeggen dat slechts één proefstuk getest volgens ASTM E399, een geldige breuktaaiheids waarde genoemd kan worden. Aangezien de meeste breuktaaiheidswaarden net niet aan enige eisen voldoen, kan toch enige vergelijking van de resultaten gemaakt worden. Het blijkt dat de breuktaaiheid van het commerciële MMC ongeveer 21 MPa \sqrt{m} is in warmtebehandelings condities B en C, hetgeen slechts iets lager is dan de breuktaaiheidswaarden voor de AA6061 legering gevonden in de literatuur, welke gemiddeld 27 MPa \sqrt{m} is. Omdat de gemeten breuktaaiheidswaarden van de condities B en C gelijk zijn, lijkt het of de breuktaaiheid van dit MMC onafhankelijk is van de warmtebehandelingen zoals ze in dit onderzoek opgelegd zijn.

De breuktaaiheid van de experimentele MMC's, welke versterkt zijn met verschillende volume fracties keramische deeltjes, is onderzocht met verschillende procedures, namelijk de ASTM E399 en de ASTM E1737 methode. Met behulp van de ASTM E1737 methode kan een duidelijke trend voor de variatie in breuktaaiheid als functie van de volume fractie versterkende Al₂O₃ deeltjes voorspeld worden, waar dat met de ASTM E399 methode niet kan.

De waargenomen trend voor de experimentele MMC's is een bij benadering lineaire afname van de breuktaaiheid met toenemende volume percentages Al₂O₃ deeltjes.

In deel B, hoofdstuk 5, is breuk in een op AA6061 gebaseerd MMC met 20 vol.% Al₂O₃ deeltjes gemodelleerd met behulp van een axisymmetrisch eindig elementen model en een statistische benadering voor het berekenen van de sterkte van de versterkende keramische deeltjes via het Weibull model [105]. In dit model zijn variabelen zoals de triaxialiteit, deeltjes grootte en matrix legering eigenschappen gevarieerd om de parameter afhankelijkheid van deeltjes breuk te onderzoeken. Bij het modelleren van het breukgedrag van één deeltje is aangenomen, dat de overlevingskans van een keramisch deeltje bepaald wordt door een Weibull verdeling. Breuk statistiek van het MMC is onderzocht door de overlevingskans van een Al₂O₃ deeltje uit te zetten tegen de macroscopische axiale spanning opgelegd aan het gehele MMC.

Gebaseerd op de uitgevoerde berekeningen, kan geconcludeerd worden dat de relatie tussen de macroscopisch opgelegde spanning op een MMC en de overlevingskans van een keramisch deeltje beschreven kan worden met de Weibull modulus, zolang de spanningsverdeling in de

matrix om een deeltje heen proportioneel is aan de opgelegde belasting. Verder is gebleken dat triaxiaal belasten van een MMC in plaats van uniaxiaal, in een lagere overlevingskans van het Al_2O_3 deeltje resulteert en dat het deeltje vermoedelijk breekt voordat plastische vervorming in de matrix optreedt.

Wanneer de overlevingskans uitgezet wordt als functie van de macroscopisch axiale spanning, moet dit resulteren in een rechte lijn met een helling voorgesteld door de Weibull modulus. De parameter afhankelijkheid van deeltjes breuk in ogenschouw nemend, kan geconcludeerd worden dat voor dezelfde belastings-verhouding, een toename in de verstevigings exponent van de matrix leidt tot samenvallende berekeningen voor triaxiale berekeningen, maar uniaxiale berekeningen vallen samen tot een punt waar kromming (een afwijking) van de rechte lijn begint. Verder resulteert een variatie van de karakteristieke spanning (σ_0 in het Weibull model) in een evenwijdige verschuiving van de curves voor zowel triaxiale als uniaxiale berekeningen. Voor een vaste waarde van de verstevigings exponent kan een 'mastercurve' gemaakt worden, onafhankelijk van de karakteristieke spanningen en matrix vloeispanningen en een toename van deeltjes diameter (en dus volume van het keramisch deeltje) zorgt voor een afname van de overlevingskans van een Al_2O_3 deeltje in een AA6061 aluminium matrix.

In taaiere metalen, ontstaan holtes over het algemeen tijdens plastische vervorming wanneer tweede fase deeltjes breken of loslaten van de omringende matrix en uiteindelijke breuk omvat de groei van aangrenzende holtes tot de vorming van een scheur. Dit concept is toegepast op MMC's in deel B, hoofdstuk 6, waarbij de verstevigende deeltjes zich gedragen als initiatie plaatsen voor holtes, ofwel door loslaten van het contactvlak tussen deeltje en matrix, ofwel door deeltjes breuk. Het door Gurson [31] voorgestelde model is toegepast in een door Tvergaard en Needleman [111] aangepaste vorm, om het breukmechanisch gedrag van MMC's te simuleren en de breuktaaiheid als functie van warmtebehandeling en verschillende volume fracties verstevigende deeltjes te voorspellen. De analyse in dit hoofdstuk is gebaseerd op de vereenvoudigde aanname dat alle holtes van begin af aan in het materiaal aanwezig zijn als gevolg van voortijdige breuk van de keramische deeltjes.

De aanname dat alle deeltjes voor de scheurtip uit gebroken zijn, is rechtvaardigd vanwege het feit dat het breukproces plaatsvindt in de directe nabijheid van de scheurtip, waar de triaxialiteit hoog is. Het model is getest aan disk-shaped compact tension proefstukken. Modelleren van het breukgedrag van de experimentele MMC's, waarvan de productie en breuktaaiheid beschreven is in hoofdstuk 4, is niet mogelijk omdat het Gurson model de extreem hoge volume fractie holtes als gevolg van breuk van de keramische deeltjes in het MMC netwerk van dit materiaal, niet aankan.

Numerieke voorspellingen tonen aan, dat er geen significante invloed van de toegepaste warmtebehandelings condities op de breuktaaiheid van het commerciële MMC te verwachten is. Dit effect wordt ondersteund door experimentele resultaten. Het Gurson model, dat in dit numerieke onderzoek toegepast is als een lokaal model met een mesh met vaste element grootte, blijkt ongeschikt te zijn voor het goed berekenen van schade-ontwikkeling in MMC's, dat wil zeggen dat de voorspelde breuktaaiheidswaarden allemaal aan de lage kant zijn. Met toenemende element groottes wordt een verschuiving naar hogere kritische spanningsintensiteitswaarden waargenomen, maar de waarden zijn nog steeds vrij laag. Berekeningen aan MMC's met 20 of 30 vol.% keramische deeltjes met behulp van het Gurson

model leveren een geconvergeerde oplossing en tonen een vergelijkbare trend als voor de experimenten, dat wil zeggen een afname in breuktaaiheid met toenemende volume fractie versterkende deeltjes.

Over het geheel genomen, kan geconcludeerd worden dat met behulp van de differentiële scanning calorimetrie techniek, de nano-indentatie techniek en de breuktaaiheids metingen het mogelijk is het (breuk) mechanisch gedrag van op AA6061 gebaseerde MMC's versterkt met Al_2O_3 deeltjes in kaart te brengen en de verkregen resultaten te vergelijken met een veelvoud aan tegenstrijdige resultaten in de literatuur. Voor wat betreft de eindige elementen berekeningen, is het mogelijk om de invloed van verscheidene variabelen zoals de grootte van de versterkende deeltjes, de volume fractie van versterkende deeltjes en de matrix verouderingsconditie afzonderlijk te onderzoeken. Verder is er een poging gedaan om de breuktaaiheid van MMC's als een functie van warmtebehandelings conditie en volume fractie versterkende deeltjes te voorspellen.

ACKNOWLEDGEMENTS

The research described in this thesis was carried out at the Laboratory for Materials Science and Technology of the Faculty of Applied Sciences at Delft University of Technology. Since I started at this laboratory as a student, I have made a lot of friends and this thesis would not have been achieved without the help of many people. On these two pages I want to take the opportunity of thanking most of them.

First of all, I would like to thank my promotors Ad Bakker and Sybrand van der Zwaag for giving me the opportunity to do my own research, for helping me when I was off the track, but most of all for their confidence in my work. I would like to thank Sybrand especially for being there when Ad became ill and stimulating me to go on.

I am especially grateful to Michael Janssen, for the profound and instructive discussions we had and for the moments he just listened to me when I was feeling down. He knows he should not carp at everything, but for me his remarks made me consider my work more thoroughly.

I am particularly indebted to Anke van Gorp and Ardy Duwel for their experimental research into the fracture mechanical behaviour of both commercial and experimental metal matrix composites. Despite the problems we came across, they both kept their enthusiasm for the subject and their contribution is highly acknowledged. The results of their valuable work are described in chapter 4 of this thesis.

I would also like to express my gratitude to the Powder Metallurgy group for allowing me, Anke and Ardy to make use of their equipment for producing our specimens, whereby I would like to thank Henk-Jan Brinkman who introduced us with the basics of powder metallurgy and Tjeerd Tobi who assisted us wherever possible. Furthermore I would like to thank André Hoogstrate who spent many evening hours on machining all our specimens.

At the Faculty of Mechanical Engineering at Eindhoven University of Technology I want to thank Willem-Pier Vellinga who performed all the nanoindentation measurements which are described in chapter 3 of this thesis.

Technical support has been most important in this research, since the workability of the produced material was not its best characteristic. Therefore, I would like to thank Jan Hermesen, Piet Verbooi and Bram Huis for their problem-solving capacities and ability to get things finished 'yesterday'.

Analyses of the material would not have been possible without the expertise of Erik Peekstok and Dave Hanlon, to whom I am very grateful for using their microscopes and sharing their knowledge.

A Fracture Mechanical Study of Precipitation Hardenable Al-Based MMCs

I also wish to thank all my colleagues within the group "Mechanical Behaviour of Materials" for the everlasting discussions at the coffee table and the many good times we had together. I will miss, but certainly not forget anyone of you!! A special thanking is for Carel ten Horn for all the hours he spent with me at the workstations.

I owe a lot of thanks to Rob Deurenberg, for his willingness to try and understand the main lines of my work and designing the cover of this thesis.

I want to thank Peter Ament for his pep-talks and always knowing exactly when to call and just listen to me.

Finally, I wish to thank Erik for his unfailing support and accepting my temper at moments when things were not going as smoothly as intended. Without you it would have been impossible to finish.

June 2000

Katja Mussert

THE AUTHOR

Katja Mussert was born on 4 September 1971 in Rotterdam, The Netherlands. In 1990 she obtained her VWO-B diploma at the Willem de Zwijger Scholengemeenschap, Papendrecht and went to Delft University of Technology to start her study at the Laboratory for Materials Science of the Department of Chemical Technology and Materials Science. In 1994 she joined the Mechanical Behaviour of Materials group of the laboratory and went for two months to the National Aerospace Laboratory NLR in Marknesse, The Netherlands, to perform her practical work. The subject of the research done there was “Fracture Surface Marking of Alclad 2024-T3 Sheet”. In 1995 she completed her masters thesis entitled “Formation of Beach Marks on Alclad 2024-T3 Sheet” at the Laboratory for Materials Science, which was a continuation of the practical work done at the National Aerospace Laboratory NLR.

In 1996 she started her PhD-study on aluminium-based metal matrix composites in both the Mechanical Behaviour of Materials and Heat Treatment Science and Technology group. The work done in the past four years is described in this thesis. Since 1 March 2000, she is employed as researcher Mechanical Performance of Products at Automotive Applications of Corus Research, Development & Technology in IJmuiden, The Netherlands.

